
Doctoral Dissertations

Student Theses and Dissertations

Spring 2018

3D seismic attribute analysis and machine learning for reservoir characterization in Taranaki Basin, New Zealand

Aamer AlHakeem

Follow this and additional works at: https://scholarsmine.mst.edu/doctoral_dissertations



Part of the [Geology Commons](#), and the [Geophysics and Seismology Commons](#)

Department: Geosciences and Geological and Petroleum Engineering

Recommended Citation

AlHakeem, Aamer, "3D seismic attribute analysis and machine learning for reservoir characterization in Taranaki Basin, New Zealand" (2018). *Doctoral Dissertations*. 2659.

https://scholarsmine.mst.edu/doctoral_dissertations/2659

This thesis is brought to you by Scholars' Mine, a service of the Missouri S&T Library and Learning Resources. This work is protected by U. S. Copyright Law. Unauthorized use including reproduction for redistribution requires the permission of the copyright holder. For more information, please contact scholarsmine@mst.edu.

3D SEISMIC ATTRIBUTE ANALYSIS AND MACHINE LEARNING FOR
RESERVOIR CHARACTERIZATION IN TARANAKI BASIN, NEW ZEALAND

by

AAMER ALI ALHAKEEM

A DISSERTATION

Presented to the Faculty of the Graduate School of the
MISSOURI UNIVERSITY OF SCIENCE AND TECHNOLOGY

In Partial Fulfillment of the Requirements for the Degree

DOCTOR OF PHILOSOPHY

in

GEOLOGY AND GEOPHYSICS

2018

Approved by

Kelly Liu, Advisor

Stephen Gao, Co-Advisor

Neil Anderson

Waleed Al-Bazzaz

Joe Guggenburger

© 2018
Aamer Ali AlHakeem
All Rights Reserved

PUBLICATION DISSERTATION OPTION

This dissertation consists of the following two publications, formatted in the style used by the Missouri University of Science and Technology:

Paper I: Pages 30-45 have been published in the AAPG Search and Discovery Data Base.

Paper II: Pages 46-85 are prepared for submission to the SEG/AAPG Interpretation Journal.

Paper III: Pages 86-96 are submitted to the SEG Technical Program.

ABSTRACT

The Kapuni group within the Taranaki Basin in New Zealand is a potential petroleum reservoir. The objective of the study includes building a sequential approach to identify different geological features and facies sequences within the strata, through visualizing the targeted formations by interpreting and correlating the regional geological data, 3D seismic, and well data by following a sequential workflow. First, seismic interpretation is performed targeting the Kapuni group formations, mainly, the Mangahewa C-sand and Kaimiro D-sand. Synthetic seismograms and well ties are conducted for structural maps, horizon slices, isopach, and velocity maps. Well log and morphological analyses are performed for formation sequence and petrophysics identification. Attribute analyses including RMS, dip, azimuth, and eigenstructure coherence are implemented to identify discontinuities, unconformities, lithology, and bright spots. Algorithmic analyses are conducted using Python programming to generate and overlay the attributes which are displayed in 3D view. Integrating all of the attributes in a single 3D view significantly strengthens the summation of the outputs and enhances seismic interpretation. The attribute measurements are utilized to characterize the subsurface structure and depositional system such as fluvial dominated channels, point bars, and nearshore sandstone. The study follows a consecutive workflow that leads to several attribute maps for identifying potential prospects.

ACKNOWLEDGMENTS

First and foremost, my thanks to my advisor Dr. Kelly Liu. Thanks to all my PhD committee members, especially, to Dr. Waleed Al-Bazzaz for uprising my research ability.

I acknowledge my PhD degree sponsor the Saudi Ministry of Higher Education. Appreciation to the Saudi Cultural Mission (SACM) for arranging a great environment for my study in the US. Accordingly, thanks to my SACM technical advisor Dr. Nabil Khoury.

My sincere gratitude to the New Zealand Government for providing the data. Thanks to the Society of Exploration Geophysicists (SEG) and Attribute Assisted Seismic Processing & Interpretation (AASPI) for giving the python attribute codes. Appreciations to Schlumberger for supplying Missouri S&T with licenses for Petrel and Techlog. Recognitions to the IHS Markit for providing licenses for Kingdom and Petra over the years.

For it is a great chance to thank all my colleagues in the Department of Geological Sciences and Engineering for motivating me and sharing knowledge. Thankfulness for all my officemates in McNutt B16/B40 who made the lab such a friendly and professional place.

My express gratitude to my mom Mrs. Fatimah AlBasha for blessing me with the love keeping me encouraged. Finally, all my appreciations go to my lovely wife, Mrs. Hashmiah Alsaedi.

TABLE OF CONTENTS

	Page
PUBLICATION DISSERTATION OPTION	iii
ABSTRACT	iv
ACKNOWLEDGMENTS	v
LIST OF ILLUSTRATIONS	ix
LIST OF TABLES	xii
NOMENCLATURE	xiv
 SECTION	
1. INTRODUCTION	1
1.1. AREA OF STUDY	2
1.2. REGIONAL GEOLOGY	3
1.3. DATA SET	10
1.4. METHODOLOGY	15
 PAPER	
I. UP-SCALED PETROPHYSICAL ANALYSES USING MICRO-LEVEL FIELD-OF-VIEW PETROGRAPHIC IMAGES FOR THE KAPUNI GROUP, TARANAKI BASIN, NEW ZEALAND	30
ABSTRACT	30
1. INTRODUCTION	31
2. OBJECTIVES	31
3. DATA AND METHOD	32
4. RESULT AND DISCUSSION	34
5. CONCLUSIONS	36

REFERENCES	45
II. RESERVOIR CHARACTERIZATION USING 3D SEISMIC ATTRIBUTES AND ASSISTED PETROPHYSICAL LOG ANALYSES WITH ARTIFICIAL NEURAL NETWORK	46
ABSTRACT	46
1. INTRODUCTION	47
2. GEOLOGICAL SETTING AND DATA SET	48
2.1. KAPUNI GROUP OF MAUI FIELD	49
2.2. 3D-MAUI DATA SET	49
3. SEISMIC INTERPRETATION	50
3.1. WELL TO SEISMIC MATCHING	50
3.2. HORIZON AND FAULT INTERPRETATION	51
3.3. ATTRIBUTE ANALYSES	52
4. PETROPHYSICAL ANALYSIS	52
4.1. PETROPHYSICAL LOG CALCULATION	53
4.2. PETROPHYSICAL LOG PREDICTION	54
5. RESERVOIR CHARACTERIZATION	57
6. CONCLUSIONS	59
REFERENCES	84
III. VALIDATION OF POSTSTACK SEISMIC INVERSION USING ROCK PHYSICS ANALYSIS AND 3D SEISMIC AND WELL CORRELATION	86
ABSTRACT	86
1. INTRODUCTION	86
2. RECURSIVE INVERSION	88
3. SEISMIC INTERPRETATION	88

4. ROCK PHYSICS ANALYSIS	91
5. DISCUSSION	92
6. CONCLUSIONS.....	95
REFERENCES	96
SECTION	
2. CONCLUSIONS.....	97
APPENDIX.....	99
BIBLIOGRAPHY.....	100
VITA	103

LIST OF ILLUSTRATIONS

Figure	Page
SECTION	
1.1. Map showing location of the Taranaki Basin that lies 1150 miles east of Australia, across the Tasman Sea.	3
1.2. Tectonic setting of New Zealand.	5
1.3. The Taranaki Basin evolution.	6
1.4. Map showing the main structural elements, Cretaceous sub-basins, outcrops, and some drilled wells in the Taranaki Basin.	7
1.5. Cretaceous - Cenozoic stratigraphic framework for the Taranaki Basin.	9
1.6. The Taranaki Basin petroleum system.	10
1.7. Basemap of the main 3D seismic surveys and wells data covers the southern of the Taranaki Basin.	12
1.8. Vertical seismic section of Inline 693 showing a first indication of gas chimney along the fault located near trace 1300.	13
1.9. Thin section photomicrographs at 1285 m depth from Well Moki-2A for the Moki Formation with plane polarised light view of conventional core sample impregnated with blue epoxy resin, Scale 31x.	13
1.10. Work flow of the study.	16
1.11. Amplitude time slice at 1.558 s.	23
1.12. Vertical seismic section of Inline 693, after applying the Hilbert transform. This section is better showing the fault located near trace 1300.	24
1.13. Illustration showing the method to compute the parameters from the well formation top and the seismic time structure in order to calculate the average velocity.	25
1.14. Illustration showing the method to compute the parameters from the well formation tops and the seismic time structure in order to calculate the interval velocity.	26
1.15. Mathematical, geologic, and seismic nomenclature used in defining reflector dip.	27

1.16. Dip corrected coherence.	29
-------------------------------------	----

PAPER I

1. Three thin section sample images and their information from Well Maui-7.....	38
2. Thin section sample# 3 from Maui-7 showing the classes identification of the pore area ranges.	39
3. Classification of pore wettability.	39
4. The first two columns shown the neural network training input and output for Maui-7 that include the porosity (ϕ) log from well analysis (Phi log) and the thin section results with core lab porosity data.....	40

PAPER II

1. Geological settings in the study area.	60
2. Workflow of the study.	61
3. Basemap of the 3D-Maui seismic survey and well data used in this study.	61
4. Synthetic seismogram generation for Well Maui-7.....	62
5. Seismic attribute sections for target horizon identification and tracking.	63
6. Attributes used for fault interpretation.....	64
7. Synthetic seismogram overlay.	65
8. Attributes generated for the Mangahewa C-sand horizon.	66
9. Multi-attributes crossplot providing better prospect, structure, and stratigraphy identification.....	67
10. Thin-section (TS) sample.....	68
11. Crossplot of DENS versus NEUT with GR color-coded for facies interpretation to recognize the Mangahewa C-sand of the Kapuni group in Maui-7.....	68
12. Petrophysical log interpretation of the Kapuni group.	69
13. The feed-forward neural network structure of one hidden layer, in addition to the input and output layers.....	71
14. Crossplots of permeability and porosity.	71
15. Quality Control (QC) crossplots for both PHI and Perm calculated logs for the Mangahewa Formation.	72

16. Quality Assurance (QA) crossplots for both PHInn and Knn predicted logs from ANN for the Mangahewa Formation.	73
17. Sequence diagram flow of the petrophysical modeling.	74
18. Petrophysical logs resulted from the NNM compared with the calculated logs and compared to the upscaled logs for both the predicted and the calculated logs.	75
19. Porosity models of the Mangahewa C-sand reservoir within the Maui B-area.	76
20. Permeability models of the Mangahewa C-sand reservoir within the Maui B-area.	77
PAPER III	
1. Rock physics template (RPT) developed by Ødegaard and Avseth (2003).	87
2. Synthetic seismogram generation for Well MB-Z(11).	89
3. C-sand horizon interpretation.	90
4. Seismic attributes of C-sand.	90
5. Crossplot between the C-sand amplitude horizon slice in Figure 4a and the C-sand AI slice in Figure 4b.	91
6. Inversion attribute cross-section along the arbitrary line shown in Figure 3a.	92
7. AI results from rock physics analysis vs. Poisson's ratio (ν) color-coded with PHI.	93
8. AI computed vs. sonic logs color-coded with PHI showing a good regression relation for Well MB-Z(11).	93
9. Rock physics template showing AI vs. V_p/V_s	94
10. Rock physics template for facies analysis.	94
11. AI extracted vs. V_p/V_s crossplot for Well MB-Z(11).	95

LIST OF TABLES

Table	Page
SECTION	
1.1. Sequence groups representing main stratigraphy and their formations forming the petroleum elements of the Taranaki Basin	8
1.2. Well data used in this study	14
PAPER I	
1. Definitions of the morphological analysis parameters.....	41
2. Identification of ten classes for the pore area size ranges applied to each thin section sample from (Figure 1).	42
3. Pre-Logic morphological pore mean values calculations of the thin section samples from Figure 1 using the parameter definitions in Table 1 and the classes of area ranges from Table 2.....	43
4. Post-Logic morphological pore mean value calculations of the thin section samples from Figure 1 using the parameter definitions in Table 1 and the classes of area ranges in Table 2.	44
PAPER II	
1. Well data used in this study and formation tops of the Mangahewa C-shale and C-sand.....	78
2. Logs utilized in this study.	79
3. Part of the post-logic morphological pore mean value calculations of the porosity (Phi), permeability (K) for the thin-section.....	80
4. Parameters used for petrophysical log analysis for the Mangahewa C-Sand Formation.....	80
5. The ANN models and logs and wells used to predict the petrophysical logs (PHInn and Knn).	80
6. QC crossplots generated for both PHI and Perm.	81
7. Statistics structural framework of the Maui Field.....	81
8. Statistics for the velocity model in the Maui Field.	82

9. Statistics for the structural grid model of the Kapuni group in the Maui B-area.....	82
10. Statistics for a structural grid of the Mangahewa reservoir in the Maui B-area.	83
11. Statistics for all obtained petrophysical logs and models.	83

NOMENCLATURE

Symbol	Description
3D	Three Dimensional
AI	Acoustic Impedance
bb1	Barrel
CALI	Caliper
CC	Correlation Coefficient
CS	Check Shot
DT	Delta-t Sonic
GR	Gamma Ray
GRI	Gas Research Institute
KB	Kelly Bushing Elevation Reference
LL3	Laterolog 3 Resistivity
LVM	Local Varying Mean
km ²	Kilometer Square
MICRO	Micro Log
TD	Target Depth
TS	Thin-Section
TWT	Two Way Time
PEF	Photo Electric Effect
RILD	Deep Induction Resistivity
RILM	Medium Induction Resistivity
RC	Reflection Coefficient
RHOB	Bulk Density
DENS	Density Log

SECTION

1. INTRODUCTION

The Taranaki Basin, a Cretaceous foreland basin, is the first explored basin in New Zealand. It covers an area of about 330,000 km² mostly in the offshore along the west coast of New Zealand's North Island. Typical plays occurred within the Taranaki Basin are half graben, inversions, volcanic edifices, extensional fault blocks, and thrust folds. The basin is filled up with about 9 km of sediments. Coals of the Pakawau and Kapuni groups are considered the most potential petroleum source rocks in the basin. The basin's typical potential reservoirs are in terrestrial, paralic and nearshore sandstones, turbidites, fractured limestone, volcanoclastics, and shelf sands reservoirs, which were developed in Cretaceous–Paleogene.

The 2015 petroleum exploration data package was prepared by the Ministry of Business, Innovation, and Employment (MBIE) in New Zealand. The package includes 2D/3D seismic surveys, composite well data, core imaging, thin section photomicrographs, production history, report of interests, and GIS maps.

The seismic data is interpreted to gain a general understanding of the structural features characterizing the geological background of the study area. Both the seismic vertical sections and the seismic horizontal slices are studied to obtain an overall view of the structural impression on the targeted horizons. Additionally, both the well logs and the formation tops provide a general indication of the structural characterization. The well data are utilized to correlate the 3D seismic volume to identify the horizons of the study.

Petrophysical analyses are implemented using both geological data in form of the thin sections of well cores to conduct the reservoir properties and to calculate petrophysical parameters including the water saturation, shale volume, and porosity. The thin sections are scanned and analyzed using the visual analysis tool that counts different pores and grains beside measuring their shapes and sizes for porosity and permeability.

Attribute processing analysis is the main goal of the study. Geometric attributes such as volumetric dip and azimuth, coherence, and curvature are crossplotted to strengthen the summation of their outputs supporting the seismic interpretation. A comparison between the Pseudo attribute and the petrophysical analysis is performed using the photomicrographs and the logs for better optimization. Attribute measurements are integrated to characterize the subsurface structure and depositional system. Finally, multi-attribute analyses are conducted to optimize the results predicted from attributes.

This integrated study is expected to support the petroleum exploration with the low cost by using the capabilities of the geophysical processing and interpretation of the seismic data. The attribute maps for identifying the potential prospects and characterizing the target reservoir by using the available seismic and well data provide constraints for future exploration and drilling.

1.1. AREA OF STUDY

New Zealand consists of two major landmasses with a total area of 250,000 km² located in the southwestern of the Pacific Ocean (Figure 1.1). However, most of New Zealand continent area (6 million km²) is submerged under the sea in the northwest, south, and east of New Zealand. It is considered a high potential prospective country for oil and gas discoveries. Many gas and oil fields are discovered. The Taranaki Basin is the

first explored basin which is a sedimentary basin in the western New Zealand with an area of about 330,000 km² mostly in the offshore (Figure 1.1). Currently, the Taranaki Basin is the only producing province in New Zealand (King et al., 2010).

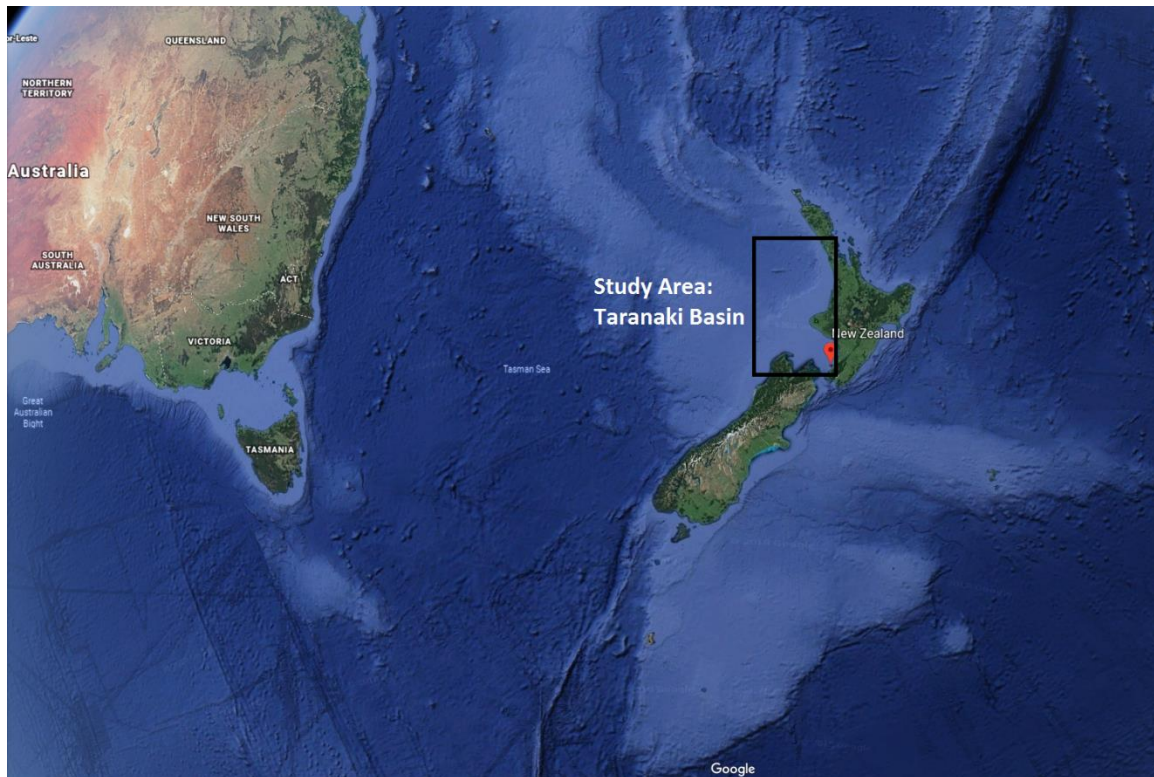


Figure 1.1. Map showing location of the Taranaki Basin that lies 1150 miles east of Australia, across the Tasman Sea. The red rectangle is the approximate location of the Taranaki Basin, west of New Zealand (Google Earth, 2018).

1.2. REGIONAL GEOLOGY

New Zealand is distributed in an active tectonic boundary between the Australian and Pacific plates (Figure 1.2). Since 20 million years ago, major deformations and uplifts developed in this region resulting the uprising of the New Zealand land above the sea level (NZPAM, 2014) (Figure 1.2). New Zealand consists of two main islands. The North Island located in the Australian Plate, while the South Island is part of the Pacific

Plate. In the eastern North Island, the Pacific Plate is subducting beneath the Australian Plate with a speed of 40 to 50 mm/yr decreasing toward south (Figure 1.2). In the South Island, the boundary between the oceanic lithosphere of the Australian and the Pacific plates is a strike slip fault known as the Alpine Fault. South of the South Island, the Pacific Plate slowly raises the Australian Plate (Figure 1.3). As a result of these plate tectonics, many basins are formed around New Zealand. This study focuses on the Taranaki Basin which is the only producing basin in New Zealand.

The Taranaki Basin is a Cretaceous foreland basin found along the west coast of New Zealand's North Island and the northern part of South Island (Figures 1.2 and 1.3) [Higgs et al., 2010]. On the north-east to east, the basin is bounded by the buried Taranaki Thrust Fault (Figures 1.4) and on the south-east by Waimeae-Flaxmore faults. The present day shelf break bounds the Taranaki Basin from south to south west. In the west, the deepwater Taranaki is extended to the north-west boundary of the basin.

The Taranaki Basin is a marine basin with a continental crust basement. Initially, it is considered as part of the Caledonian Basin. However, the Taranaki Basin was separated from the Caledonian Basin about 118 Ma with the propagation of the New Zealand-Antarctic Ridge [King et al., 2010]. This intra-continental failed rift separated proto-New Zealand from the eastern Gondwana. Between 80 – 55.5 Ma, drift of New Zealand continental fragment from the remnant Gondwana (Australia-Antractical) block occurred to start open the Tasman Sea [King et al., 2010]. Moreover, the thrust fold and arc developed 20 Ma in the North-east of the Taranaki Basin [Higgs et al., 2010].

The basin is characterized by many tectonic elements developed since Cretaceous, which includes passive margin, platform subsidence, volcanic arc, fold-thrust belt, and

back-arc rift. These tectonic events formed many sub-basins (Higgs et al., 2010). The main sub-basins that characterized with thick deposits are Pakawau, Manaia, and Maui sub-basins in the south, and the Moa and Te Ranga sub-basins in the north (Figure 1.4).

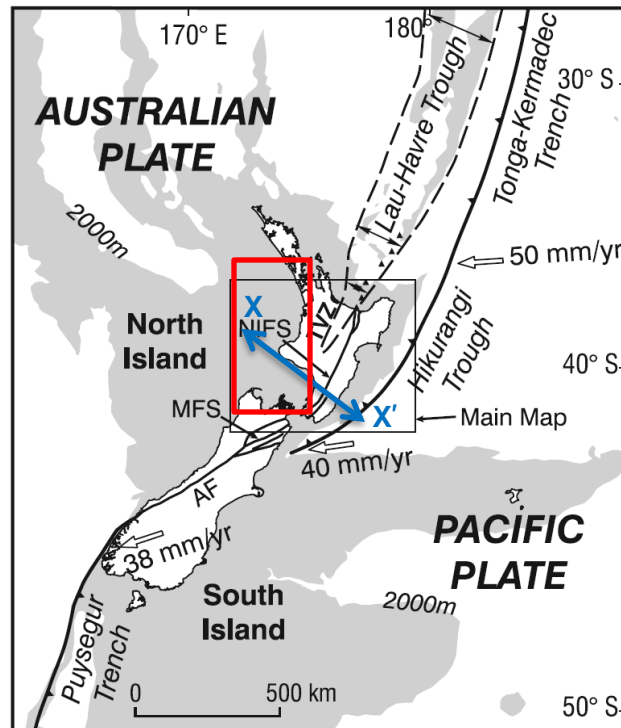


Figure 1.2. Tectonic setting of New Zealand. The estimated boundary of the Taranaki Basin is shown east of the northern Island. The shaded area is the sedimentary accumulation around New Zealand with many basins. The Taranaki Basin is bounded by the red lines. The blue line represents the X – X' cross-section in Figure 1.3 (Modified from Nicol et al., 2007).

The Taranaki Basin contains typical plays, such as half graben, inversions, volcanic edifices, extensional fault blocks, and thrust folds. Sediments fill up to about 9 km in the basin (King et al., 2010). The basin consists of four main stratigraphy, i.e., the Late Cretaceous Pakawau group, the Paleocene-Eocene Kapuni and Moa groups, the Oligocene-Miocene Ngatoro and Wai-iti groups, and the Plio-Pleistocene Rotokare group (Table 1.1 and Figure 1.5).

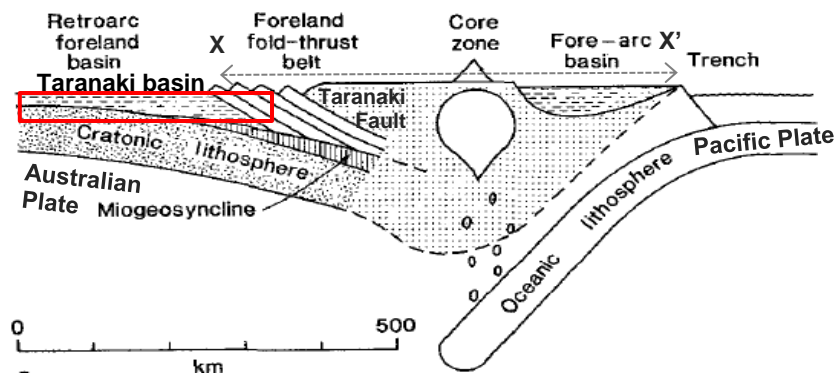


Figure 1.3. The Taranaki Basin evolution. The red lines bound the basin. The location of line X – X' can be found in Figure 1.2 (Modified from Stern and Davey, 1990).

A wide range of lithofacies is presented in the basin and characterized by fluvial-deltaic depositional system. As a result, typical reservoirs developed such as terrestrial, paralic, nearshore sandstones, turbidites, fractured limestones, volcanoclastics, and shelf sand reservoirs (King et al., 2010).

Coals of the Pakawau and Kapuni groups considered the most potential petroleum source rocks in the Taranaki Basin. Late Cretaceous Pakawau Group source rocks started converting (Type III) Kerogen to hydrocarbons between about 65 to 20 Ma. The Eocene Kapuni group source rocks generated hydrocarbons from the marginal marine (Type II) Kerogens since the last 0.4 M.yr. In addition, there is a good organic carbon generative source potential from the coal-bearing Rakopi, Farewell, Kaimiro, and Mangahewa formations (Figure 1.6).

The Taranaki Basin geologic style and fault system (Figure 1.4) played a primary role in migrating the hydrocarbon from the source coaly rocks, and marine shales in the Cretaceous–Paleogene to the upper potential reservoir. Moreover, the source rocks of the Taranaki Basin evolved a large volume of CO₂ prior to oil generation that could support the migration process (King et al., 2010).

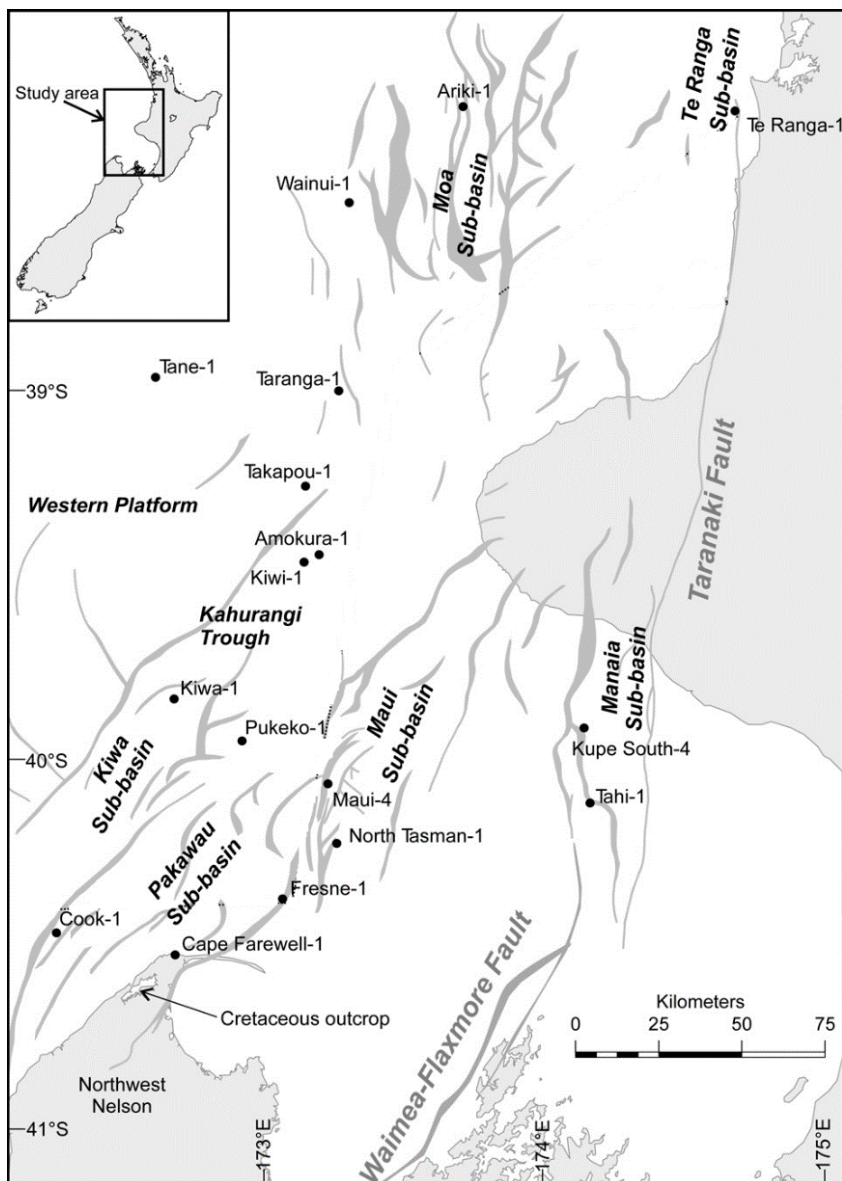


Figure 1.4. Map showing the main structural elements, Cretaceous sub-basins, outcrops, and some drilled wells in the Taranaki Basin (Higgs et al., 2010).

Table 1.1. Sequence groups representing main stratigraphy and their formations forming the petroleum elements of the Taranaki Basin (Modified from Higgs et al., 2010; King et al., 2010).

Age	Phase	Petroleum Element	Group	Formation	Reservoir Facieses
Plio-Pleistocene	Regressive	Reservoir/Seal	Rotokare	Mangaa	Slope sandstones
				Giant foresets	Fine-grained basin
				Tangahoe	Fine-grained shelf deposits
				Matemateaonga	Floor, slope, and shelf deposits
Miocene		Reservoir/Seal	Wai-Iti	Urenui	Slope channel conglomerates
				Mt Messenger	Volcaniclastic sediments
				Mohakatino	Submarine fan sands
				Moki	Submarine fan sands
				Manganui	Shelf to basin floor mudstones
Oligocene		Transgressive	Reservoir/Seal	Ngatoro	Taimana
	Tikorangi				Limestone and slope carbonates
	Otaraoa				Calcareous sandstones and limestone
Eocene	Reservoir/Seal		Moa	Tangaroa	Submarine fan sandstone
				Turi	Shelf and slope, mudstones
	Reservoir/Seal/Source		Kapuni	Mckee	Shallow-marginal marine sandstones
				Mangahewa	Coastal sands, coal mudstone
				Kaimiro	Fluvial sands, coal mudstone
Paleocene			Farewell	Fluvial braid plain coastal sands, coal mudstone	
L. Cretaceous		Source	Pakawau	Rakopi	Organic marine coal mudstone

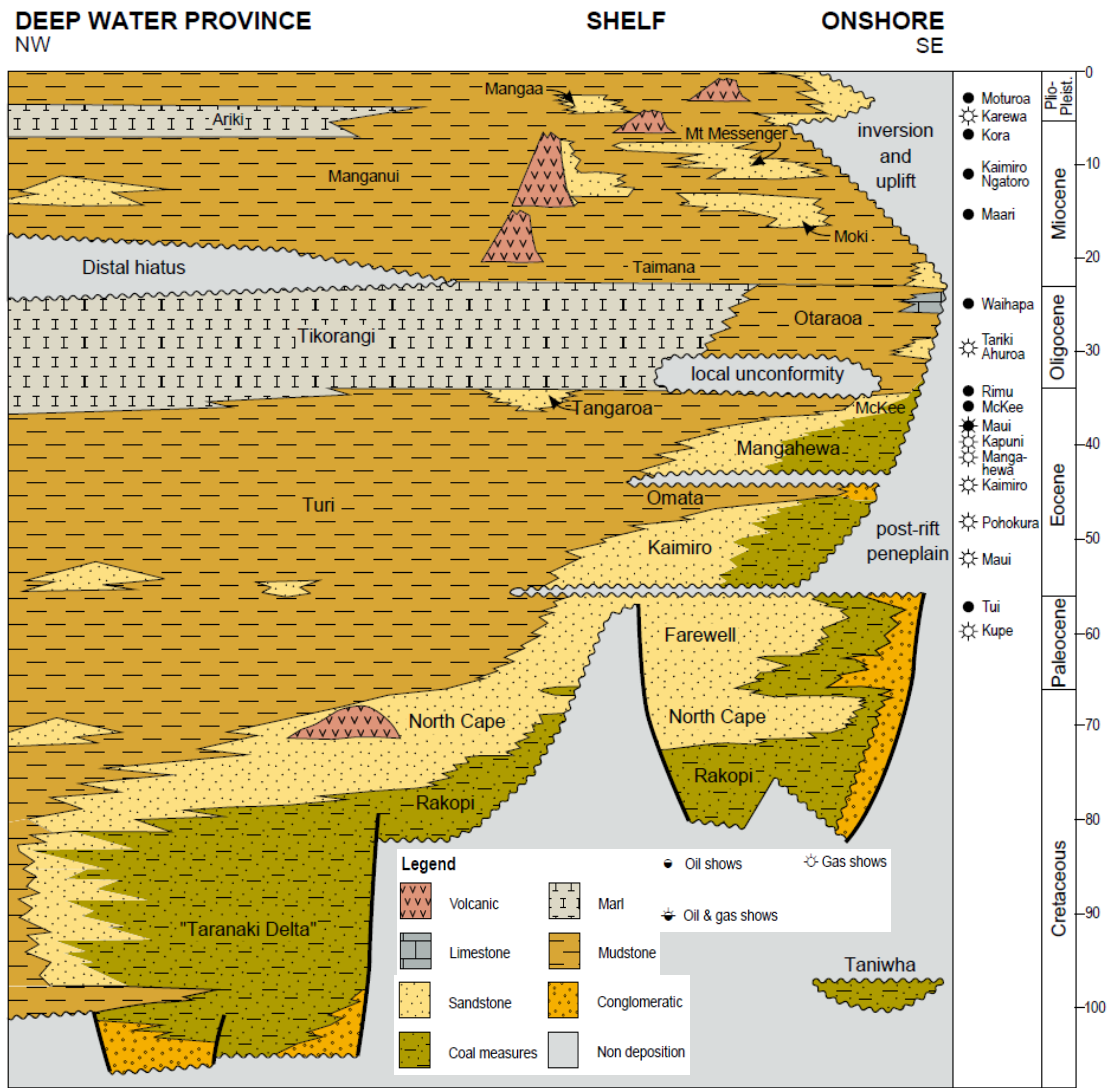


Figure 1.5. Cretaceous - Cenozoic stratigraphic framework for the Taranaki Basin (NZPAM, 2014).

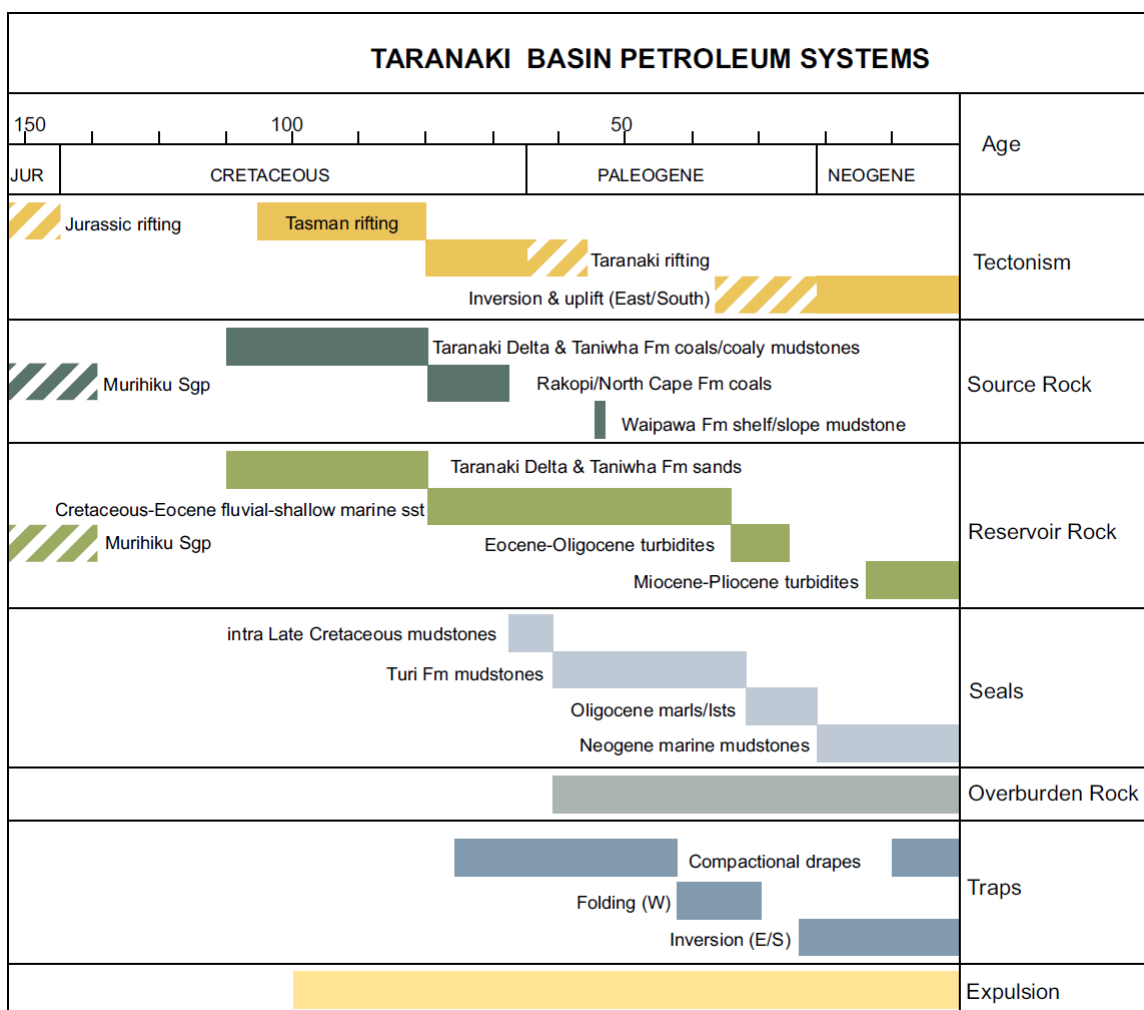


Figure 1.6. The Taranaki Basin petroleum system (NZPAM, 2014).

1.3. DATA SET

The Petroleum Exploration Data Pack was provided by the New Zealand Petroleum and Minerals (NZPAM). The pack includes information about the Taranaki, Tasman Frontier, Reinga-Northland, East Coast, Pegasus, Raukaumara, West Coast, Western Southland, Whanganui, Great South, and Canterbury basins. The content of the data pack is listed as following:

- **Seismic Data:** there are about 582 2D/3D seismic survey projects. For the Taranaki Basin, there are 255 2D seismic survey projects and 41 3D seismic data. The seismic surveys are attached with their seismic navigation files and cultural data across New Zealand. The seismic data studied in this project includes three 3D seismic data sets, i.e., Maui Base, Maari, and Kerry, in addition to many 2D lines which cover the area between Manaia and Maui sub-basins (Figure 1.10).
- **Well Data:** there are Las data from 535 wells that compose many types of logs such as Gamma ray (GR), SP, resistivity, sonic, density, and neutron. Depth-TWT calibration files are attached. In this study, around 40 wells are studied (Table 1.2). Moreover, the wells are attached with geological data in the form of thin section photomicrograph core photos and samples for specific reservoirs (Figure 1.9). Also, there are petrophysical data in form of geochemistry and fluid flow base data of the reservoirs, well testing, and production history for the wells.
- **Maps and Reports:** there is a comprehensive GIS dataset of the seismic and well data available, such as seamless Geology GNS QMAP of a 1:250,000 geological map series of onshore New Zealand. This includes GIS mapping of studied petroleum source rock potential, seal rock distribution and quality, and petroleum occurrences, in addition to New Zealand Basement Composition and Heat Flow GIS. Report of interests regarding seismic processing, geological history, and petroleum prospectively are included.

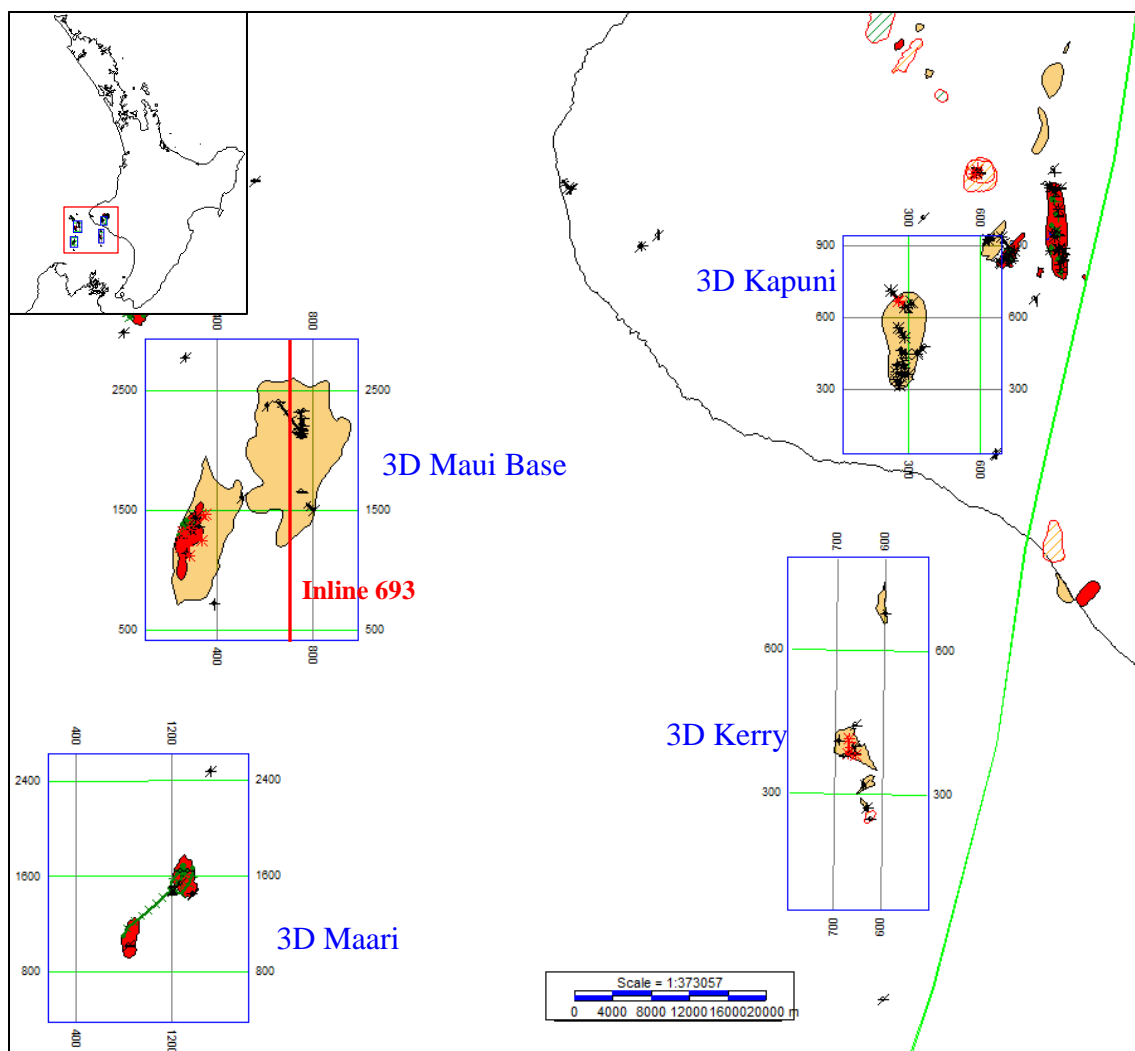


Figure 1.7. Basemap of the main 3D seismic surveys and wells data covers the southern of the Taranaki Basin. The box in the upper left shows the location of the study area in red box relative to the North Island. The red line in 3D Maui Base represents Inline 693 shown in Figure 1.8.

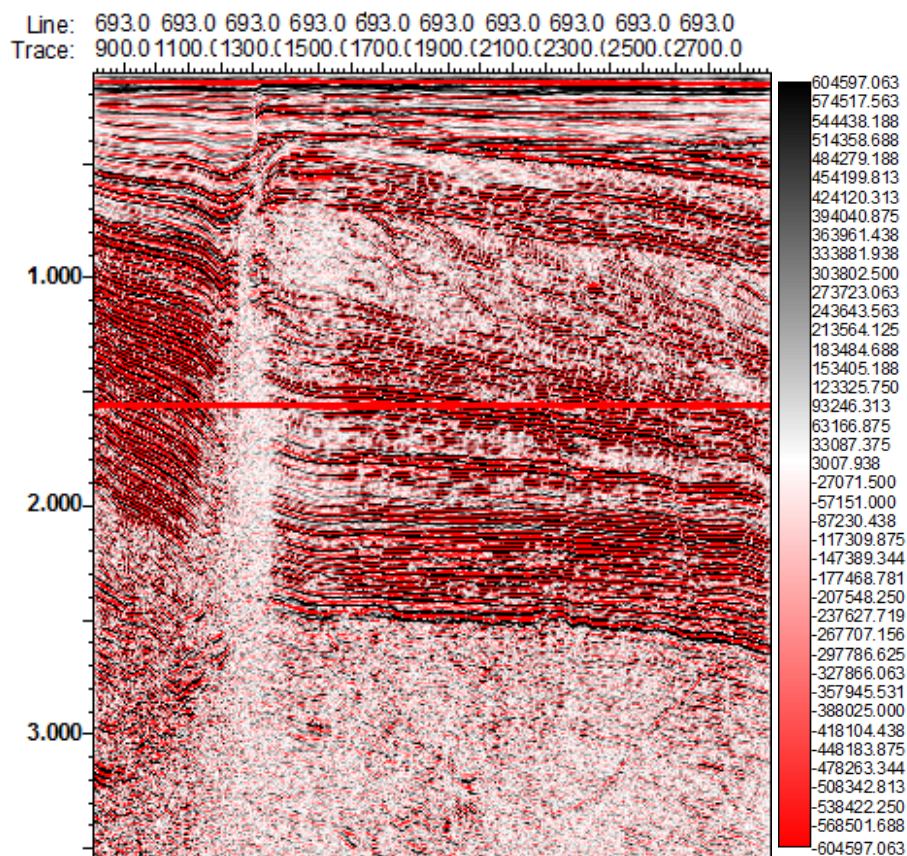


Figure 1.8. Vertical seismic section of Inline 693 showing a first indication of gas chimney along the fault located near trace 1300.

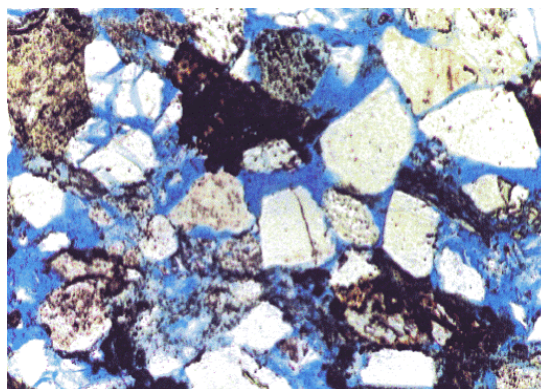


Figure 1.9. Thin section photomicrographs at 1285 m depth from Well Moki-2A for the Moki Formation with plane polarised light view of conventional core sample impregnated with blue epoxy resin, Scale 31x. This moderate magnification view of a clean, fairly labile-rich and fine-grained sandstone indicates the well interconnected pore system typical of this sample (pores stained blue).

Table 1.2. Well data used in this study

	Well Name	KB (m)	TD (m)	X(m)	Y(m)	Formation at TD	Status
1	Kea-1	22.5	3135	1629021.19	5586256.34	Kapuni Group	Abandoned
2	Kupe South-1	32.5	3503	1695302.41	5587765.45	Farewell	Suspended
3	Kupe South-2	33.78	3250	1694679.21	5589393.76	Pakawau Group	Suspended
4	Kupe South-3	32.3	3447	1696349.87	5588793.19	Pakawau Group	Suspended
5	Kupe South-4	33.1	3800	1697379.36	5584897.75	Tahi Group	Abandoned
6	Kupe South-5	31.3	3200	1698008.83	5581189.35	Puponga Group	Suspended
7	Kupe South-6	44	3385	1695807.27	5588188.69	Puponga Group	Gas/Condensate
8	Kupe South-7	44	3503	1695809.66	5588188.63	Farewell	Gas/Condensate
9	Kupe South-8	44	3834	1695806.11	5588191.17	Farewell	Gas/Condensate
10	Kupe-1	9.4	3682	1696469.65	5590960.2	Kapuni Group	Abandoned
11	MA-02A	45.13	5603	1638616.51	5621546.16	Kapuni Group	Suspended
12	MA-10A	45.13	4114	1638615.02	5621551.45	Kapuni Group	Suspended
13	Maari-1	27.4	2200	1625842.11	5575775.01	Kapuni Group	Suspended
14	Maari-2	25	1495	1625844.62	5574534.69	Moki	Abandoned
15	Maui South-1	27	2942	1639157.45	5614106.61	Otaraoa	Abandoned
16	Maui-1	9.45	3510	1626596.18	5608925.2	Pakawau Group	Suspended
17	Maui-2	34	3567	1638598.35	5615317.6	Rotoroa Igneous	Suspended
18	Maui-3	34	3401	1638807.91	5623794.59	Pakawau Group	Suspended
19	Maui-4	34	3919	1620562.08	5567960.22	Basement	Abandoned
20	Maui-5	26.8	3227	1632348.3	5614729.85	Kapuni Group	Abandoned
21	Maui-6	27	3228	1635014.86	5624367.68	Kapuni Group	Abandoned
22	Maui-7	27	3139	1627524.56	5612683.1	Kapuni Group	Plugged
23	MB-N(5)-A	39.41	3729	1627100.15	5611575.54	Kapuni Group	Active
24	MB-P(8)	39.42	3709	1627100.45	5611571.94	Kapuni Group	Oil Well
25	MB-Q(10)	39.42	3802	1627098.75	5611569.85	Kapuni Group	Gas Well
26	MB-R(1)	39.42	3620	1627103.47	5611579.55	Kapuni Group	Oil Well
27	MB-S(12)	39.42	4402	1627097.16	5611567.85	Kapuni Group	Gas Well
28	MB-T(9)	39.42	3639	1627096.75	5611571.55	Kapuni Group	Gas Well
29	MB-V(3)	39.42	3781	1627101.79	5611577.54	Kapuni Group	Suspended
30	MB-W(2)	39.42	4186	1627105.45	5611577.85	Kapuni Group	Gas Well
31	MB-X(4)	39.42	3930	1627103.75	5611575.85	Kapuni Group	Oil Well
32	MB-Z(11)	39.42	3100	1627095.15	5611569.54	Kapuni Group	Gas Well
33	Moki-1	26	2620	1626642.15	5575783.81	Kapuni Group	Abandoned
34	Moki-2A	22	1822	1627177.03	5573424.25	Mahoenui	Abandoned
35	Momoho-1	39.2	3145	1697661.88	5582417.16	Puponga Group	Abandoned
36	MR5P12	46.94	4773	1625073.28	5573773.85	Manganui	Oil Well
37	Rahi-1	29	3501	1629439.29	5603654.36	Basement	Dry Hole
38	Tahi-1	26	1776	1699269.95	5562322.44	Pakawau Group	Abandoned
39	Tieke-1	23.58	3579	1626407.77	5629373.08	Basement	Abandoned
40	Toru-1	32	4151	1699510.04	5602622.7	Farewell	Suspended

1.4. METHODOLOGY

Seismic interpretation is the extraction of subsurface geologic information from seismic data. The seismic data is interpreted to gain a general understanding of the structural features characterizing the geological background of the study area. Both the seismic vertical sections and the seismic horizontal slices are studied to obtain an overall view of the structural impression on the target horizons. Additionally, both the well logs and the formation tops are utilized for the structural characterization and for correlating the 3D seismic volume with the well data to precisely identify the horizons of the study. Figure 1.10 shows the workflow and final results of the study.

A synthetic seismogram is a simulated seismic response computed from well data. It is a suitable tool for correlating geological data from well logs with seismic data. The seismic data are displayed in time. Synthetic seismogram provides both time and depth for accurate reflection event verification. The components needed to generate a synthetic seismogram include Time-Depth (T-D) chart, velocity log, density log (DENS), and wavelet. Following are the description of each of the components:

Time-Depth (T-D) Chart is used to connect depth of well logs to time in the seismic section. It can be generated for a well through the checkshots, which utilized either explosive or vibroseis sources. For better results, the T-D chart can be integrated with the sonic log (DT), which records the travel times of an emitted wave from the source to receivers. Moreover, the T-D chart can be built using the checkshots, integrated with their logs. On the other hand, applying the T-D chart for a specific well to other wells will lead mislocated horizons. In order to better locate horizons, new T-D charts are generated for each well by correlating the formation top data with the horizon.

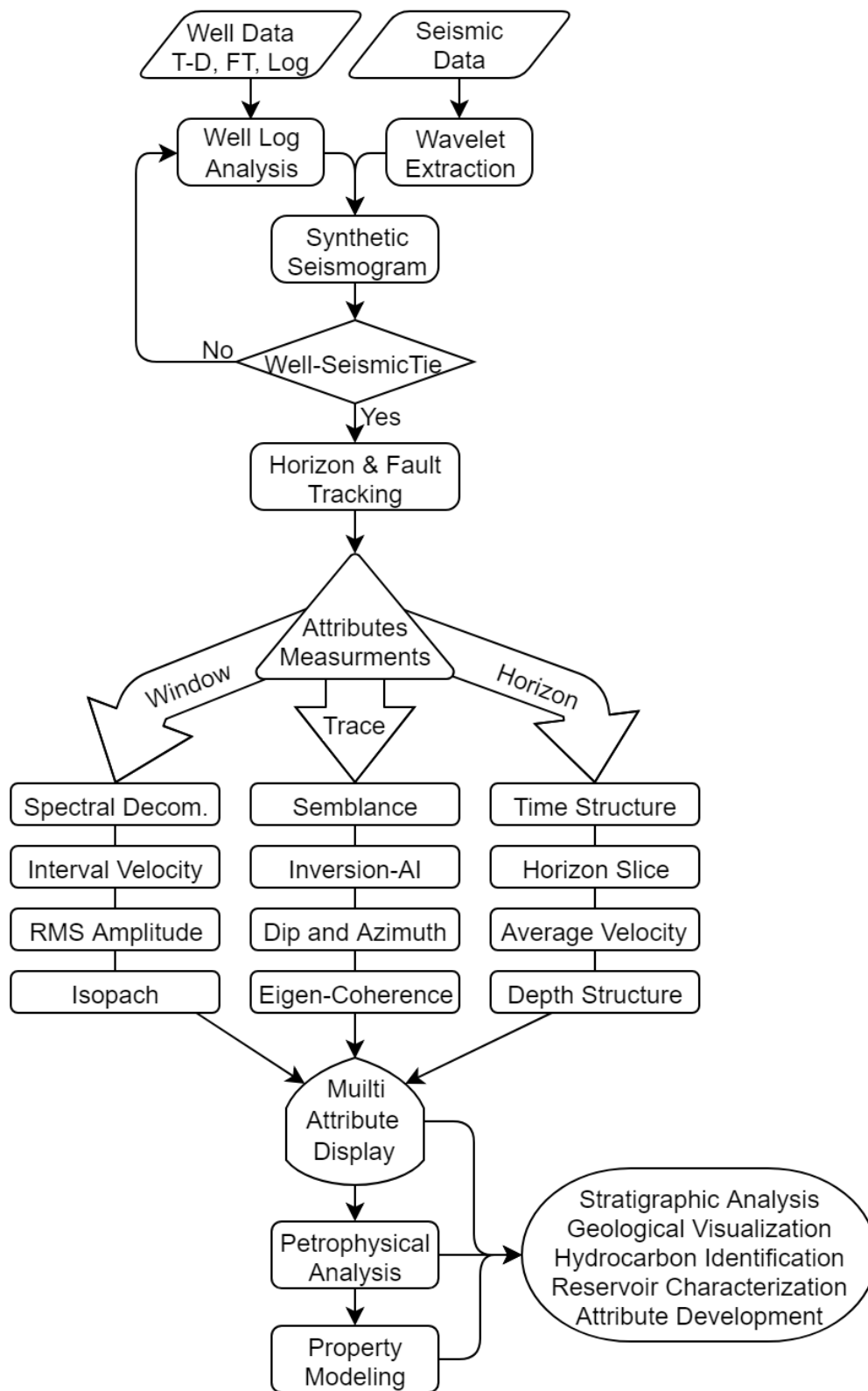


Figure 1.10. Work flow of the study.

Acoustic Impedance (AI) is the product of the velocity and the density log at a specific layer. The velocity log is a record of the wave speed along the well formations. It can be measured directly from DT. DENS is combined with the DT to compute the acoustic impedance as a function of depth. The velocity relates mathematically to both the density (by Gardner's correlation) and the resistivity (by Faust's correlation). Thus, it can be measured from either density logs or resistivity logs.

The wavelet depends on the seismic acquisition source and can be extracted from the seismic traces surrounding the well.

The Reflection Coefficient (RC) is a measure of the AI contrast at a formation bed boundary. It is expressed mathematically as:

$$RC = \frac{AI_2 - AI_1}{AI_2 + AI_1} , \quad (1)$$

The reflection coefficient is computed from equation (1) for each time sample. Hence, a sequence of coefficients is generated as a reflection coefficient series. The reflection coefficient series is convolved with the wavelet extracted to generate the synthetic seismogram. Finally, the synthetic seismogram is matched with nearby survey traces so that well log features can be tied to the seismic data.

Synthetic matching of the generated synthetic seismogram is utilized to match the generated synthetic seismogram with the real seismic data. Seismic trace is extracted for each well from the nearest seismic traces around the well. This extracted trace represented the real seismic data to be used in the synthetic matching. The synthetic trace can be shifted, stretched, or squeezed to obtain the best matching results. The cross-correlation coefficient (r) between the seismic trace and the synthetic seismogram during

the synthetic editing is calculated to clarify the quality of the synthetic matching. The cross-correlation coefficient ranges between -1.0 (perfectly out of phase) and $+1.0$ (perfectly matched in shape).

Horizon and fault interpretation requires picking a reflection event across all the seismic survey lines. Interpreting specific event yields records of both time and amplitude values. Therefore, the interpreted horizon is a composite of different traces varying in time and amplitude values for a specific layer. Faults are represented by discontinuities in the seismic data. By tracing these discontinuities, fault surface map can be generated. Structural maps can be constructed after the horizons are tracked. The Two Way travel Times (TWT) are stored after horizons are picked to generate time structure maps. The gradient projection gridding algorithm process is used to smooth the time structure map. That process computes X and Y derivatives at every data sample location. In addition, it allows projecting an interpolated value at a grid node using an inverse distance to a power weighting.

Well log analysis is performed to interpret the lithology of the seismic data. Well logs analysis includes crossplots of logs that yields a perfect tool to measure and recognize many geological, geophysical, and petrophysical parameters. For example, Gamma Ray (GR) and Spontaneous Potential (SP) are utilized to identify the lithology (Asquith and Kryqowski, 2004).

Petrophysical analysis is conducted by integrating the seismic interpretations and well log analyses to obtain the reservoir properties. Reservoir characterization is important for many aspects. The information obtained is used to identify prospects. It is also valuable for production and development for the hydrocarbon reservoir fields.

Various data such as well data, logs, cuttings, core data, core plugs, production tests, and petrophysical data can be processed, analyzed, and interpreted to improve the well production, and help identifying prospects. The thin section will be scanned and analyzed using the visual analysis software tool that counts different pores and grains beside measuring their shapes and sizes to measure porosity and permeability (Al-Bazzaz et al., 2007).

The reservoir properties are extracted from the seismic data in the target zones. They are used for attribute measurements of the geophysical and geological data, which are used in many different interpretation aspects such as structural interpretation and reservoir evaluation. While the petrophysical analyses help characterizing the reservoirs, it can also be used to perform attribute maps such as porosity map and Pseudo well generation. Following are the main analysis methodology of the studied petrophysical parameters:

Porosity (Φ) expresses the fraction of the rock pore volume (PV) over the bulk volume (BV). The most important type of porosity is the effective porosity (Φ_e) which measures the connectivity of voids of the rock, porosity can be calculated by studying the morphology of the grains and pores in the thin section photographs (Al-Bazzaz et al., 2007). It is represented by the following fraction:

$$\Phi = \frac{\sum PoreArea}{\sum PoreArea + \sum GrainArea} \quad , \quad (2)$$

On the other hand, well logs can be analyzed to measure the porosity. The density logs are useful for porosity calculation. First, velocity logs were estimated using the Faust relationship (Faust, 1953):

$$Velocity = C (D R_t)^{1/6} , \quad (3)$$

where $C=1948$. R_t is the resistivity, and D is the corresponding depth. The Bulk density logs (DENS) are generated using the velocity logs (Gardner, 1974):

$$DENS = C_1 Velocity^{0.25} , \quad (4)$$

where $C_1 = 0.2295$, a constant depending on the rock type. Density porosity (PHID) can be calculated (Asquith and Kryqowski, 2004):

$$PHID = \frac{(RHOMA-DENS)}{(RHOMA-RHOF)} , \quad (5)$$

where fluid density (RHOF) can be assumed as 1.0, and the matrix density (RHOMA) is 2.65 for sand. If density and neutron logs are available, the effective porosity log (PHIE) can be calculated (Asquith and Kryqowski, 2004). The relation is expressed as following:

$$PHIE = \left[\frac{(PHID-PHIN)}{2.0} \right] (1 - V_{sh}) , \quad (6)$$

where PHID is the density porosity (in decimals), PHIN is the neutron porosity (in decimals), and V_{sh} is the shale volume (in decimals). In addition, porosity can be calculated from the sonic log (DT) (Asquith and Kryqowski, 2004). The sonic porosity (PHIS) is calculated in equation (7) below:

$$PHIS = C \left[\frac{(DT-DTM)}{(DTF-DTM)} \right] , \quad (7)$$

where DT is the sonic travel time ($\mu\text{s}/\text{ft}$), DTM is the sonic travel time of the matrix which is $55.5 \mu\text{s}/\text{ft}$ for sandstone, DTF is the sonic travel time of the fluid $189 \mu\text{s}/\text{ft}$, and C is a constant, which is 0.7 for gas and 0.9 for oil.

Water Saturation (S_w) is a ratio of the pore volume filled with water over the bulk volume. It can be obtained from the resistivity logs (Asquith and Kryqowski, 2004). S_w is expressed mathematically by the Archie equation:

$$S_w = \sqrt[n]{\frac{AR_w}{\phi^m R_t}} \quad , \quad (8)$$

where R_w is the resistivity of the formation water assumed to be 0.02 ohm-meter, R_t is the value from the resistivity log in ohm. A is the tortuosity factor which is 1 , m is the cementation exponent which is 2 , n is a constant varying from $1.8 - 2.5$, commonly, it is 2 .

Permeability (K) measures the movement ability of fluids within the formation. The permeability log can be derived from the water saturation and the porosity using the Wyllie-Rose (1950) and Timur (1968) method (Asquith and Kryqowski, 2004):

$$K = C \frac{\phi^{4.4}}{S_{w-irr}^2} \quad , \quad (9)$$

where K is the permeability in millidarcies (mD), C is the oil constant of 8581 , ϕ is the porosity, and S_{w-irr} is the water saturation of a zone at irreducible water saturation.

A seismic attribute is any measure of seismic data that helps us better visualize or quantify features of interpretation interest. Attributes extracted from seismic data are utilized to determine reservoir properties. Attributes are considered to include such quantities as interval velocity, inversion for acoustic impedance, pore-pressure prediction,

bright-spot detection, direct detection of hydrocarbons by different seismic measurements. Those Types of attributes can be classified as following:

1. Horizon (Slice) based attribute includes the amplitude time slice, time structure, horizon slice, average velocity to compute depth structure maps. The curvature attribute is useful for identifying folds and flexures, compaction, and karst (Figure 1.11).
2. Formation (Window) attributes include the Root-Mean-Square (RMS) amplitude, interval velocity, spectral decomposition, and porosity. The RMS amplitude is a post-stack amplitude attribute. Mathematically, it is calculated by using the square root of the sum of squared amplitudes divided by the number of samples within the specified window. It is an effective attribute that helps determining hydrocarbon prospects. In fact, it enhances hydrocarbon bright spots and can be used as a Direct Hydrocarbon Indicator (DHI).
3. Trace attributes include the acoustic impedance, Hilbert transform, coherence, dip, and azimuth. Volumetric dip and azimuth attributes are valuable to define a local reflector surface and is structurally driven coherence effective method for representing geological discontinuities such as faults, channel edges, karst, and dewatering features in 3-D seismic data volumes (Figure 1.12).

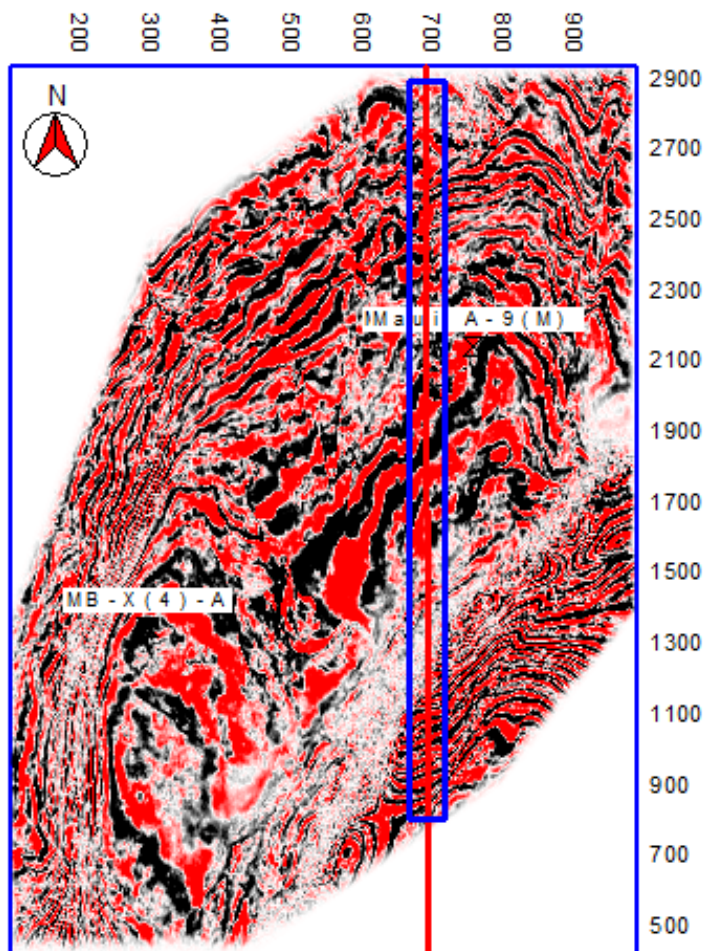


Figure 1.11. Amplitude time slice at 1.558 s. The red-blue line is Inline 693 that is illustrated as a horizontal red line in both Figure 1.8 and Figure 1.12.

Following are the algorithms that are used in this study to obtain the seismic attributes:

- **Average velocity map** is important to compute depth maps. After constructing the time structure maps, depth maps can be obtained with velocity information. The relationship between the average velocity (V_{avg}), the two way travel time to reflector (target horizon), and the depth of the horizon (D) is shown in equation (10) below.

$$V_{avg} = \frac{2D}{TWT} \quad (10)$$

The velocity used to convert the seismic data from time domain to depth domain is computed for each well. The TWT is obtained from the time structure of the targeted horizon. The formation top data are used for the depth value (D) (Figure 1.13). The average velocity values calculated from the provided wells for specific horizon are gridded. As a result, the average velocity map computed is used for the depth map generation.

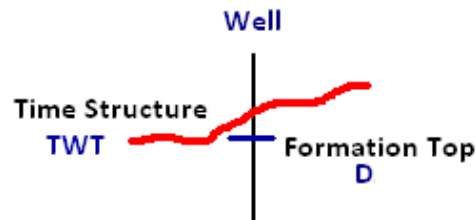


Figure 1.13. Illustration showing the method to compute the parameters from the well formation top and the seismic time structure in order to calculate the average velocity. (Alhakeem, 2013).

- **Interval velocity map** is the seismic velocity over a specific interval of rock or strata. It can be expressed mathematically by the following equation:

$$V_{int} = \frac{2(D_1 - D_2)}{(T_1 - T_2)}, \quad (11)$$

where V_{int} is the interval velocity, D_1 is the depth to the upper reflector, D_2 is the depth to the lower reflector, T_1 is the two way travel time to the upper reflector, and T_2 is the two way travel time to the lower reflector (Figure 1.14).

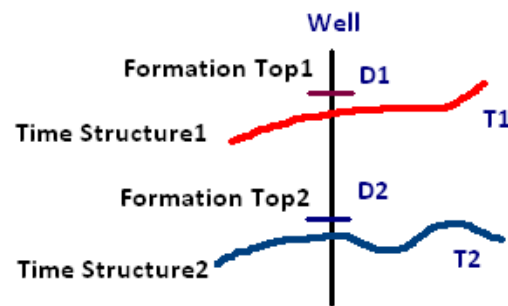


Figure 1.14. Illustration showing the method to compute the parameters from the well formation tops and the seismic time structure in order to calculate the interval velocity. (Alhakeem, 2013).

- **Geometric Attributes** are volumetric dip and azimuth, coherence, and curvature are geometric attributes that are useful to show the stratigraphy and discontinuity of the seismic data. Moreover, they can be generated to support each other's measurements. In fact, volumetric dip and Azimuth (Figure 1.15) are used to derive the coherence that is an effective tool to represent faults and stratigraphy. (e.g., Marfurt et al., 1998; Marfurt et al., 1999; Luo et al., 1996, 2001).

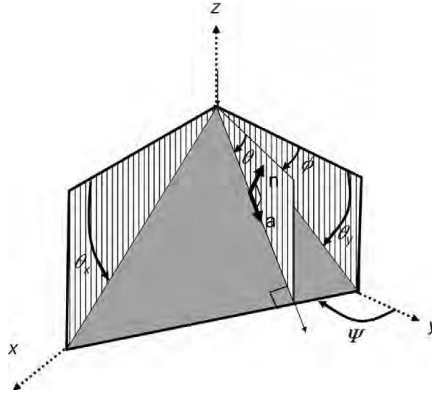


Figure 1.15. Mathematical, geologic, and seismic nomenclature used in defining reflector dip. By convention, n = unit vector normal to the reflector; a = unit vector dip along the reflector; θ = dip magnitude; ϕ = dip azimuth; ψ = strike; θ_x = the apparent dip in the xz plane; and θ_y = the apparent dip in the yz plane.

Dip and azimuth can be defined in equations (12) and (13) as following:

$$\omega = 2\pi f = 2\pi \frac{\partial \phi}{\partial t} = 2\pi \frac{\frac{\partial d^H}{\partial t} d - \frac{\partial d}{\partial t} d^H}{d^2 + (d^H)^2}, \quad \phi = \text{atan2}(d^H, d),$$

$$k_x = \frac{\partial \phi}{\partial x} = \frac{\frac{\partial d^H}{\partial x} d - \frac{\partial d}{\partial x} d^H}{d^2 + (d^H)^2}, \quad s = (p^2 + q^2)^{1/2},$$

$$k_x = \frac{\partial \phi}{\partial x} = \frac{\frac{\partial d^H}{\partial x} d - \frac{\partial d}{\partial x} d^H}{d^2 + (d^H)^2}, \quad p = \frac{k_x}{\omega}; q = \frac{k_y}{\omega},$$

Dip:
$$\theta = \tan^{-1} \left(\frac{\sqrt{k_x^2 - k_y^2}}{k_z} \right), \quad (12)$$

Azimuth:
$$\phi = \text{atan2}(k_x, k_y), \quad (13)$$

Where ω is the instantaneous frequency. Kx and ky are the instantaneous wavenumbers. d^H is the Hilbert transform with respect to depth (z). θ_x and θ_y are the angular dips.

On the other hand, coherence attribute first generalized by Marfurt et al. (1998) from Finn's (1986) by applying the semblance scanning method to 3D data. This generates a robust means of estimating reflector dip from multi-trace analysis windows (Figure 1.16). In fact, coherence can be generated using three methods, i.e. crosscorrelation algorithm, semblance, and eigenstructure algorithms. It can be defined in the equation (14) as following:

$$C_S(\theta_x, \theta_y) = \frac{\sum_{k=Ks}^{Ke} \left\{ \left[\frac{1}{J} \sum_{j=1}^J u_j(k\Delta t - p\Delta x_j - q\Delta y_j) \right]^2 + \left[\frac{1}{J} \sum_{j=1}^J u_j^H(k\Delta t - p\Delta x_j - q\Delta y_j) \right]^2 \right\}}{\sum_{k=Ks}^{Ke} \left\{ \frac{1}{J} \sum_{j=1}^J [u_j(k\Delta t - p\Delta x_j - q\Delta y_j)]^2 + \frac{1}{J} \sum_{j=1}^J [u_j^H(k\Delta t - p\Delta x_j - q\Delta y_j)]^2 \right\}}, \quad (14)$$

Where p and q are given in the process of equations (12) and (13), x_j and y_j denote the local coordinates of the j th trace measured from an origin at the analysis point, J denotes the total number of traces in the analysis window, and Ks and Ke denote the first and last temporal sample, respectively, in the analysis window.

Finally, multi-attribute analyses help clustering the attributes to optimize the results.

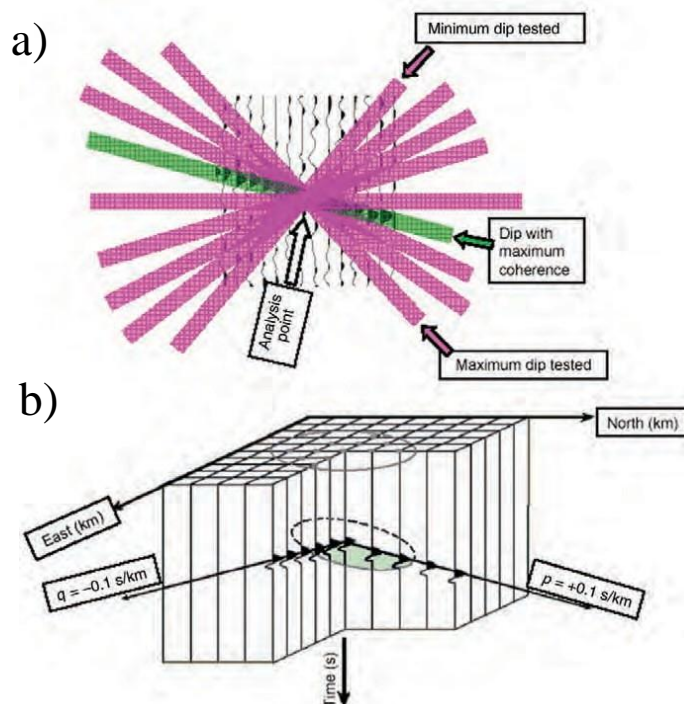


Figure 1.16. Dip corrected coherence. (a) A schematic diagram showing a 2D search based estimate of coherence. First, the algorithm estimates coherence using semblance, variance, principal component, or some other statistical measure (such as that given by equation 13) along a discrete number of candidate dips (shown in magenta and green). In this example, the maximum coherence is calculated along the dip (shown in dark green).

Next, the algorithm passes an interpolation curve through the coherence measures estimated by the peak value and two or more neighboring dips (shown here in light green). The peak value of this curve gives an estimate of coherence, whereas the dip value of this peak gives an estimate of instantaneous dip. (b) A schematic diagram showing a 3D search-based estimate of coherence, in which p indicates the inline and q the crossline components of vector time dip. The technique is analogous to that shown in (a). (After Marfurt et al., 1998).

PAPER**I. UP-SCALED PETROPHYSICAL ANALYSES USING MICRO-LEVEL
FIELD-OF-VIEW PETROGRAPHIC IMAGES FOR THE KAPUNI GROUP,
TARANAKI BASIN, NEW ZEALAND**

Aamer Alhakeem¹, Kelly Liu¹, and Waleed H. Al-Bazzaz²

Search and Discovery Article #10953 (2017)

¹Affiliation Geology and Geophysics, Missouri S&T, Rolla, MO, United States

²Kuwait Institute for Scientific Research, Ahmadi, Kuwait

Email: alhakeem.a@gmail.com

ABSTRACT

This paper presents the results of pore level micro-analyses and characterization of the Kapuni Group sandstone reservoir in the Taranaki Basin, New Zealand. In Well Maui-7, three rock fragments of the Mangahewa Formation, situated at depths of 2736 m, 2796 m, and 2897 m, are selected for analyses. In addition, two rock fragments of the Kaimiro Formation, situated at depths of 3011 m and 3028 m, are analyzed. After sample preparation, various petrographic images are captured with a thin section microscope at different depths of magnification. The images are then processed to study the pore networks in the space domain between a lower bound of 50 μm and an upper bound of 4 mm. Then, petrophysical parameters such as porosity, permeability, and MHR are measured at their native selected spaces (Al-Bazzaz and Al-Mehanna, 2007). The well logs, including density, neutron, resistivity, GR, and SP, are analyzed to calculate the

porosity and permeability logs. Neural network processing is conducted by combining the morphological pore sample and well log analyses for the training of the computer. Using the consistent data measured and delineated from different field-of-view (FOV), up-scaling porosity, matrix permeability, MHR, and grain-size at micro-levels are investigated effectively. The petrophysical parameters obtained from up-scaling FOV scale sizes are utilized to develop a simple statistical model. The sample size scale to be measured includes 600X-FOV, which is adequate for recognizing features at 50 μm -scale size, then gradually escalates to 450X-FOV for recognizing features at 100 μm -scale size, 300X-FOV for features at 200 μm -scale size, 100X-FOV for features at 500 μm -scale size, and finally, 40X-FOV for features at 2 mm-scale size.

1. INTRODUCTION

The Taranaki Basin, a Cretaceous foreland basin, covers an area of about 330,000 km^2 mostly in the off-shore along the west coast of the North Island, New Zealand (King et al., 2010). Due to its great potential and wide promising, various data including geological, geophysical, and petrophysical data are collected and processed to predict reservoir characteristics using relative fast, inexpensive, and reliable methods. The “Big data” analyses produce QC petrophysical log analysis, logs modification, and upscaling. Three approaches, i.e., morphological approach, well log analyses, and computational neural networking modeling, are utilized to investigate data from micro- to meter-level.

2. OBJECTIVES

Three rock fragments from the Mangahewa Formation are analyzed in this study. The objectives include:

- To qualify and quantify the pores and the nature of the pore network in the formation
- To describe the wettability of the formation
- To study the porosity and the relative permeability action of internal influences of pore and grain morphology
- To measure porosity, relative permeability, and Mean Hydraulic Radius (MHR) (pore-throat)
- To invest in the “Big data” available from the basin to extract valuable hidden information and patterns for fast, inexpensive, and reliable reservoir characterization
- To provide QC tool for the petrophysical log analysis using lower scale level thin sections which provide significant amount of petrophysical measurements

3. DATA AND METHOD

The data were provided by the Ministry of Business, Innovation, and Employment (MBIE) in New Zealand. The dataset includes 2D/3D seismic surveys, composite well data, geological data (core lab data, thin sections, etc.), geophysical data, drilling data, production data, and reports, which can be processed as “Big data” to extract hidden valuable information and patterns. In Well Maui-7, three rock fragments of the Mangahewa Formation, situated at depths of 2736 m, 2796 m, and 2897 m, are selected for analyses (Figure 1). In addition, two rock fragments of the Kaimiro Formation, situated at depths of 3011 m and 3028 m, are analyzed. After sample preparation, various petrographic images are captured with a thin section microscope at different depths of magnification.

Petrophysical analyses by morphological approach are implemented using the thin section images of Maui-7 to conduct a study of the pore networks in the space domain between a lower bound of 50 μm and an upper bound of 4 mm (Table 1). The thin sections are scanned and analyzed using the visual analysis tool, which counts different pores and grains based on pre-identified classes of pore sizes ranges (Table 1) beside measuring their shapes, sizes, and distribution (Tables 2, and 3). Petrophysical parameters such as porosity, permeability, and MHR are measured at their native selected spaces according to the method proposed by Al-Bazzaz and Al-Mehanna (2007) (Table 4). Wettability, as described in Table 1, is predicted for each sample and is classified as shown in Figure 3.

Petrophysical well log analyses are conducted by using density, neutron, resistivity, GR, and SP logs to calculate the porosity and permeability logs (Asquith and Krygowski, 2004). The morphological analysis of the thin sections provides spatial measurements along the wellbore. However, with such big data available for the formation, petrophysical parameters can be computed along the formation by correlating with measured petrophysical core data and log. The Well Maui-7 data are utilized to associate a precise up-scaling of the micrometer domain thin section data to meter domain logs. Computational approaches of analyses are conducted by combining the morphological pore sample, core data, and well log analyses for the Neural Network Training (NNT) (Figure 4). Then, Neural Network Model (NNM) is performed for further predictions. The porosity log of Well Maui-5 was predicted with more realistic results as shown in Figure 4 in the NNM input and output. Using the consistent data

measured and delineated from different field-of-view (FOV), up-scaling porosity, matrix permeability, MHR, and grain-size at micro-levels are investigated effectively.

4. RESULT AND DISCUSSION

The morphological analyses of the thin section (TS) practically match the results of core lab and well log analysis. The challenges in calculating the porosity from the morphological approach is the black stain in the thin section images that affect the porosity measurements. However, with better geological and petrophysical background involved with such big data, accurate decisions made to describe such features.

Sample TS1 at 2736 m has 3 unique pore distributions, extremely tight, moderately tight and large pores. At the beginning, 3,443 pores are captured, selected, and counted from 2X thin section image. All pores are grouped in 10 classes for pre-logic measurements, and these 10 classes are generated from the 3,443 claimed big data. Subsequently each class was subject to post logic calculations (Table 3), which yielded 10 interesting pore morphology and petrophysical attributions summarized in Table 4. Out of all distribution 3 zones are subject for discussion. Zone A (extremely tight) is defined by classes 1, 2 and 3. It has the most available pores abundance 29%, 2.4%, and 1.1% and an equivalent pore diameter of 2.0, 4.8, and 6.2 μm respectively. The porosity is low in class 1 which is about 6%, but high in classes 2 and 3 which are 24.1%, 34.7% respectively. The permeability is calculated to be 55 md, 166 md, and 232.5 md respectively. The pore-throat (MHR) is approximated to be 3.1 μm , 5.1 μm , and 5.7 μm respectively. The wettability is approximated to be 179°, 169°, and 150° indicating that zone A is strongly-oil-wet. Zone A is then described as low in oil production and it will need EOR recovery enhancement. Zone B has 4 classes (4, 5, 6, and 7). They are bigger

in area than zone A but less in abundance than zone A, roughly around 1% in total. The equivalent diameters are 7.4 μm , 8.3 μm , 9.1 μm , and 9.9 μm . The porosity for zone B is doubled roughly about 50%, which is better than zone A, and the average permeability is about 350 md. The wettability is described as a transition from strongly-oil-wet (171° and 174°) in classes 3 and 5 respectively to medium-oil-wet (119° and 125°) in classes 6 and 7 respectively. Zone B will show an increase in water production later in the formation development cycle. This zone is a candidate for water flooding secondary recovery. Zone C is classes 8, 9, and 10 and shows the greatest pore area, but the least abundance, about 0.2% in total. However, their pore equivalent diameters are the greatest, 11.0 μm , 11.4 μm and 12.1 μm . Zone C pore style and size will be responsible for the easy flow regime within the formation. In respect with zone A and zone B, zone C shows the greatest porosity regime, >50% and the greatest permeability regime, over than 400 md. The average pore throat for zone C is 10.3 μm . The wettability is described between moderately-oil-wet to moderately-water-wet, indicating that zone C is the main primary oil recovery region in the formation. Zones A, B, and C are unique and have different characterization signatures; however, the overall average behavior of the TS1 sample including all three zones yields a pore diameter equivalent of 1.3 μm , average porosity of 21.6%, average permeability of 47.5 md, a pore throat connecting diameter of 7.8 μm , and contact angle wettability of 113° creating an overall medium-oil-wet reservoir conditions. Water flooding is highly recommended for 2736 m depth.

For samples TS2 2796 m and TS3 2897 m (Table 3), and the same analyses as sample TS1 were conducted. TS2 has about 1494 count of pores. TS3 has about 17,339 count of pores. Both samples have 3 zones of pore networks zone A, zone B, and zone C.

Sample TS2 has zones A and B strongly-oil-wet, but zone C has strong-water-wet to medium-oil-wet indicating better oil recovery than sample TS1 (Table 4). TS2 has an average porosity of 16.1%, an average permeability of 783 md, and an average pore-throat (MHR) of 4.1 μm . The overall wettability contact angle is 109° medium-oil-wet. Sample TS3 has also 3 distinctive production zones. Zone A is described as strongly-oil-wet, zone B as medium-oil-wet, and zone C as strongly-water-wet regimes. The average porosity is 16.9 % and the average permeability is 332 md. The average pore-throat (MHR) is 4.4 μm , which is better than sample TS2. The sample TS3 will show fast oil recovery due the combination effect of highest number of pores, water wet wettability, high permeability and MHR.

The integration of the porosity well log analysis of Maui-7 as input porosity curve with the thin section analysis and the core lab data using the neural network training yielded more realistic and confident porosity log (Figure 4) for the NNT output curve. The NNM was built based on the training of the logs with the TS and core lab data. The NNM predicted an enhanced porosity curve of Well Maui-5 by minimizing the fluctuating in the beginning of the log as shown in Figure 4 for the NNM predicted curve.

5. CONCLUSIONS

- 1- Three zones were successfully measured, A (the smallest), B (the middle), and C (the largest). Zone A is described to be strongly-oil-wet, zone B is described to be medium-oil-wet, and zone C is either be medium-oil-wet or strongly-water-wet depending on the size area of the pore. The larger the pore, the more likely follow water wet regimes.

- 2- The more abundance of pores, the more likely increase in permeability. The higher area of pores just as zone C in the formation, the higher potential of oil recovery.
- 3- Porosity and permeability average values can be different than core data, for the imaging processing can capture all classes of pore networks (zones A, B, and C); while core analyses cannot accurately penetrate to zone A type of networks.
- 4- Zone A oil recovery is a candidate for EOR, zone B for water flooding secondary recovery and zone C for primary recovery, all regimes are available in different proportions in the same formation.
- 5- TS1 has the lowest oil recovery potential. TS2 has better oil recovery system than TS1. TS3 has the greatest oil recovery potential.
- 6- Porosity of (16.5 – 21.6%), permeability of (47.5 – 782.5 mD), and MHR of (4.1 – 7.8 μm) with medium to strong oil wet wettability indicate that the Mangahewa Formation is a good reservoir, which is consistent with the previous studies.
- 7- The neural network model offered a valuable tool for pseudo well log predictions for this area.


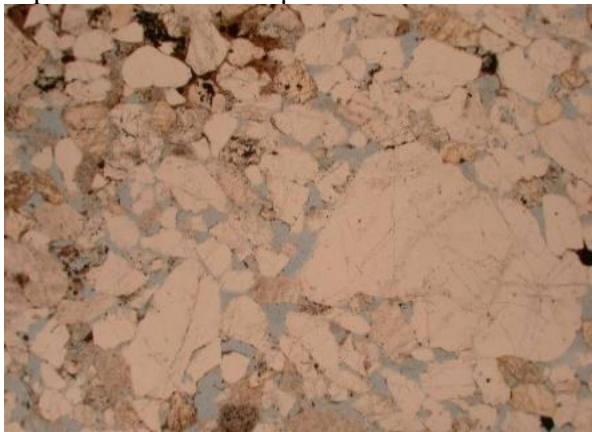

Sample Info	Thin Section Image
<p>Sample# 1</p> <p>Formation: Mangahewa C-Sand</p> <p>Depth: 2736 m</p>	<p>2xpl View Width 4000 μm</p> 
<p>Sample# 2</p> <p>Formation: Mangahewa C-Sand</p> <p>Depth: 2796 m</p>	<p>2xpl View Width 4000 μm</p> 
<p>Sample# 3</p> <p>Formation: Mangahewa C-Sand</p> <p>Depth: 2897 m</p>	<p>2xpl View Width 4000 μm</p> 

Figure 1. Three thin section sample images and their information from Well Maui-7.

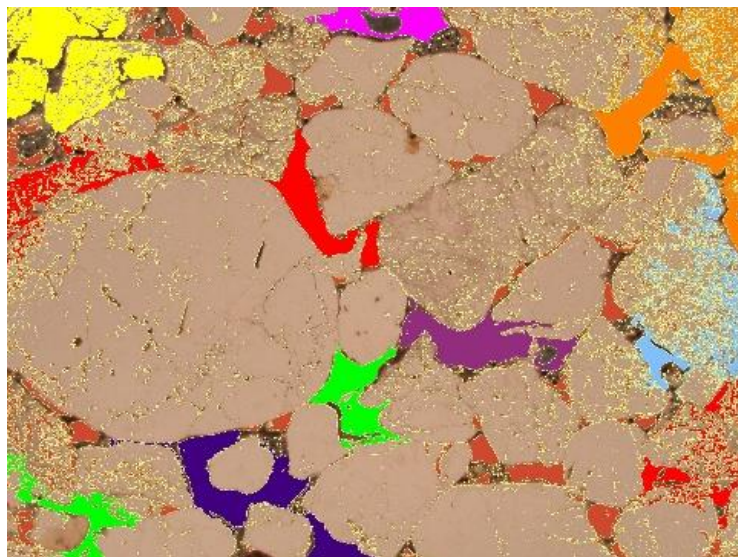


Figure 2. Thin section sample# 3 from Maui-7 showing the classes identification of the pore area ranges.

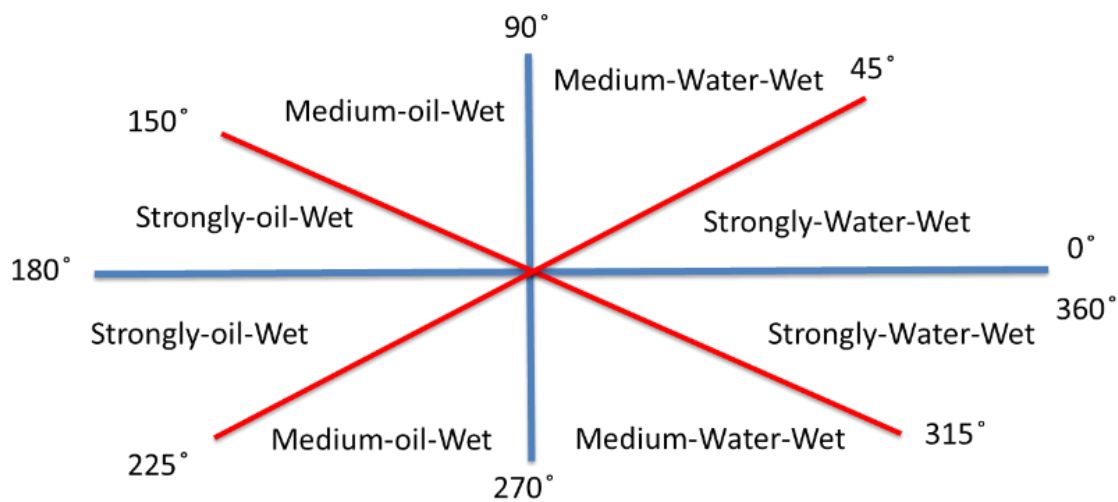


Figure 3. Classification of pore wettability (Al-Bazzaz, 2017).

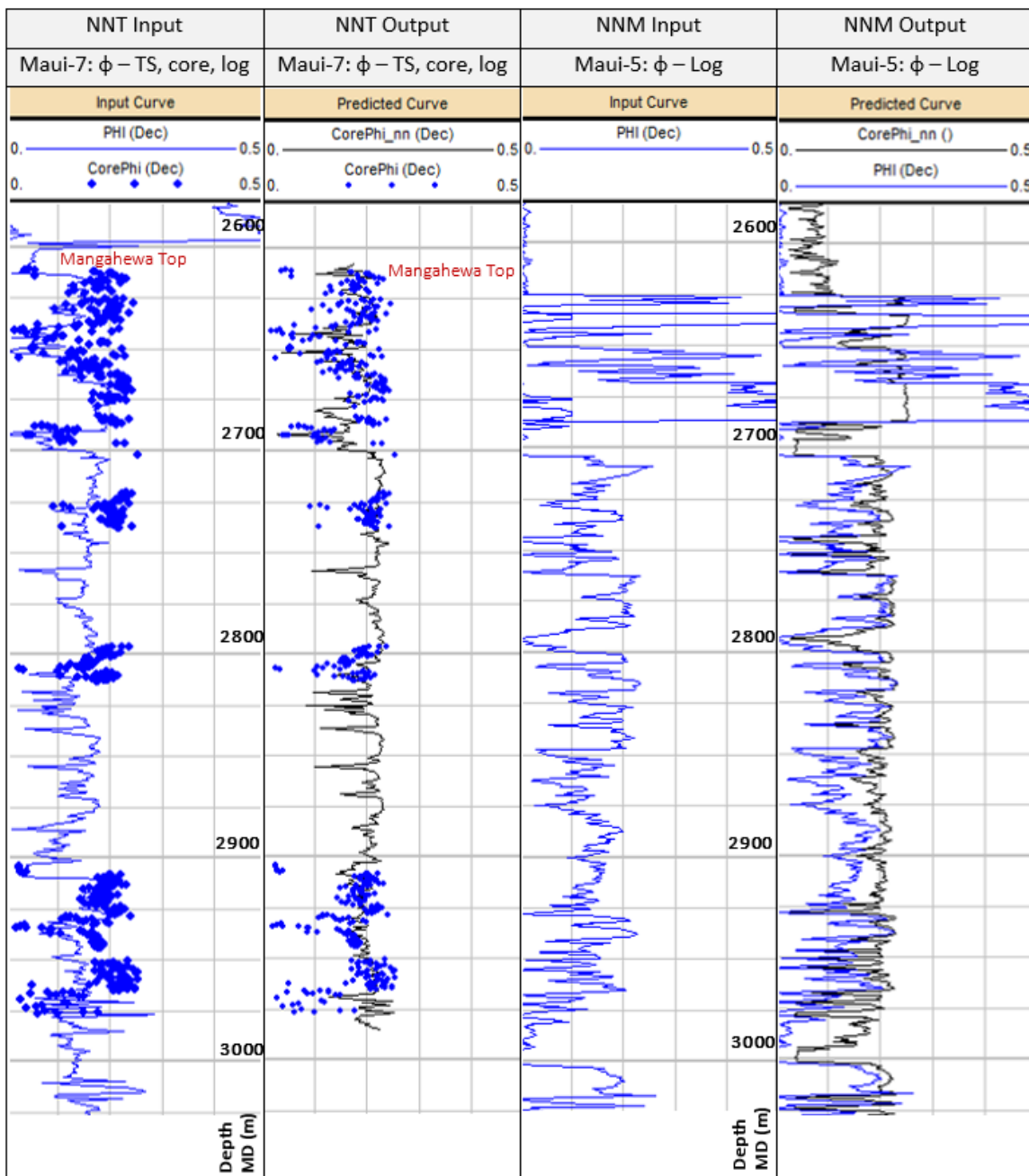


Figure 4. The first two columns shown the neural network training input and output for Maui-7 that include the porosity (ϕ) log from well analysis (Phi log) and the thin section results with core lab porosity data. The two last columns shown neural network modeling input (blue) and output (black).

Table 1. Definitions of the morphological analysis parameters (Al-Bazzaz and Al-Mehanna, 2007).

Parameter	Method	Units	Approach	Description	Comments
Pore Area	Σ Pore Area	$\mu\text{-m}^2$	Visual Counting	Measured	Accurate
Grain Area	Σ Grain Area	$\mu\text{-m}^2$	Visual Counting	Measured	Accurate
Pore Perimeter	Pore Circumference	$\mu\text{-m}$	Visual Counting	Measured	Accurate
Porosity	$\phi = \frac{\sum PoreArea}{\sum PoreArea + \sum GrainArea}$	Fraction	Summation/Statistical	Calculated	Low Error
Hydraulic Radius	$HydraulicRadius = \frac{PoreArea}{PorePerimeter}$	$\mu\text{-m}$	By Definition	Calculated	Avoid Circular or Triangular Shape Simplicity
Mean Hydraulic Radius (MHR)	$MHR = \frac{\sum_1^n HydraulicRadius}{n}$	$\mu\text{-m}$	Averaging/Statistical	Calculated	Pore Throat for a Sample
The Long L-axis of a Grain Particle	L-axis	$\mu\text{-m}$	Visual Counting	Measured	Accurate
The Short L-axis of a Grain Particle	S-axis	$\mu\text{-m}$	Visual Counting	Measured	Accurate
The Intermediate I-axis of a Grain Particle	$I = \frac{L + S}{2}$	$\mu\text{-m}$	Mid-point Averaging	Calculated	Simple Approach
Grain Diameter	$GrainDiameter = \frac{I}{1.32}$	$\mu\text{-m}$	Kumar & Cui Sieve Method	Calculated	Originally Applied for mm-scale Grain Particles
Permeability	$k = 5.6281 \cdot \frac{d^2 \cdot \phi^3}{(1 - \phi)^2}$	milli-Darcy	Carmen & Kozeny	Calculated	Diameter & Porosity are Accurately Measured
Class Pore Area	Total Pore Areas Fitted in a Range of Pore Areas where MHR is Located	$\mu\text{-m}^2$	Visual Counting	Measured	Accurate
Wettability	Θ = Pore Shapes and Morphology	Deg	Pore/grain Orientations (New Proposal)	Measured	2-D

Table 2. Identification of ten classes for the pore area size ranges applied to each thin section sample from (Figure 1).

Class (1-10)	Area Range [μm^2]
1	1-500
2	500-1000
3	1000-1500
4	1500-2000
5	2000-2500
6	2500-3000
7	3500-4000
8	4000-4500
9	4500-5000
10	5000-10000
Total	1-10000

Table 3. Pre-Logic morphological pore mean values calculations of the thin section samples from Figure 1 using the parameter definitions in Table 1 and the classes of area ranges from Table 2.

Morphological Pore Analysis (Pre-Logic) Mean Values											
Class	Frequency [%]	Area [μm^2]	Perimeter [μm]	Elongation	Roundness	Circularity	Width [μm]	Length [μm]	W/L	Equivalent	Angle [$^\circ$]
1	29.10	28.5	9.1	1.9	2.5	1.3	1.8	3.4	2.0	2.0	179.0
2	2.35	140.8	28.4	3.7	2.6	0.7	4.6	8.6	2.0	4.8	169.4
3	1.05	235.0	41.5	4.8	2.3	0.5	6.3	11.2	1.9	6.2	150.1
4	0.55	333.5	48.5	4.6	2.2	0.5	7.7	12.9	1.7	7.4	171.0
5	0.26	424.4	53.7	4.3	3.0	0.7	7.5	16.2	2.2	8.3	174.2
6	0.09	512.7	63.9	5.0	2.8	0.5	9.4	17.7	1.9	9.1	119.0
7	0.09	594.7	75.6	6.3	2.5	0.4	10.1	18.1	1.9	9.9	125.0
8	0.03	741.7	71.4	4.3	2.7	0.6	10.0	20.7	2.1	11.0	17.0
9	0.12	801.6	86.9	6.4	2.0	0.3	11.6	19.1	1.6	11.4	117.8
10	0.06	903.3	66.8	3.1	2.0	0.6	11.7	19.8	1.7	12.1	179.0
TS1	100.0	21.4	5.4	1.5	3.1	2.1	2	1.1	0.5	1.3	113.0
1	14.06	78.1	45.5	2.3	2.4	1.0	8.5	15.4	0.6	9.4	179.0
2	2.07	338.5	120.7	3.6	2.5	0.7	19.5	35.0	0.6	20.7	144.0
3	1.27	566.1	166.5	4.1	2.2	0.6	28.4	45.6	0.6	26.8	169.0
4	0.80	818.6	201.9	4.2	2.6	0.6	31.8	59.8	0.5	32.3	156.7
5	0.47	1031.7	261.0	5.4	2.5	0.5	39.0	65.2	0.6	36.2	174.5
6	0.33	1243.2	295.2	5.9	2.1	0.4	45.6	76.5	0.6	39.8	158.2
7	0.27	1409.8	240.8	3.3	2.6	0.8	39.2	73.6	0.5	42.4	143.6
8	0.27	1676.3	411.7	8.8	2.3	0.3	51.5	84.1	0.6	46.2	52.0
9	0.07	1947.4	408.2	6.8	3.9	0.6	47.8	108.3	0.4	49.8	73.3
10	0.07	2148.8	364.4	4.9	2.8	0.6	55.4	109.1	0.5	52.3	105.5
TS2	100.0	78.6	24.9	1.5	2.4	1.6	4.6	8.0	0.6	4.9	109.0
1	9.395	26.0	29.9	2.72	3.8	1.4	4.3	8.3	0.5	4.21	179.3
2	0.006	3033.6	508.5	5.10	6.8	1.3	42.7	170.7	0.3	62.20	178.1
3	0.012	3992.0	1133.3	1.86	28.8	15.5	105.6	142.6	0.7	71.28	142.1
4	0.017	5641.8	1691.1	2.59	43.7	16.9	98.6	186.7	0.5	84.74	132.9
5	0.006	6525.8	995.6	4.09	12.1	3.0	76.6	190.6	0.4	91.22	6.9
6	0.006	8191.1	1684.5	3.44	27.5	8.0	110.0	316.2	0.3	102.20	29.1
7	0.006	10460.8	4907.8	1.95	183.0	94.0	136.8	249.2	0.5	115.50	81.7
8	N/A	N/A	N/A	N/A	N/A	N/A	N/A	N/A	N/A	N/A	N/A
9	0.006	12931.8	1654.8	0.58	16.8	28.8	139.1	173.4	0.8	128.41	5.9
10	0.006	15194.0	3150.6	0.99	51.9	52.4	199.6	285.2	0.7	139.19	78.0
TS3	100.0	7.6	5.2	2.3	1.3	0.6	1.0	1.7	0.6	1.10	72.3

Table 4. Post-Logic morphological pore mean value calculations of the thin section samples from Figure 1 using the parameter definitions in Table 1 and the classes of area ranges in Table 2. The Post-Logic calculations include the Wettability, Porosity (ϕ), Permeability (K), and pore-throat (MHR).

Post-Logic				
Class	Wettability	ϕ [%]	K [mD]	MHR [μm]
1	strongly-oil-wet	6.05	54.91	3.14
2	strongly-oil-wet	24.14	166.14	4.96
3	medium-oil-wet	34.68	232.51	5.66
4	strongly-oil-wet	42.97	284.84	6.88
5	strongly-oil-wet	48.95	322.58	7.90
6	medium-oil-wet	53.67	352.38	8.03
7	medium-oil-wet	57.33	375.55	7.87
8	strongly-water-wet	62.63	409.01	10.39
9	medium-oil-wet	64.43	420.37	9.23
10	strongly-oil-wet	67.12	437.36	13.53
TS1	medium-oil-wet	21.60	47.53	7.80
1	strongly-oil-wet	16.40	778.82	1.72
2	Medium-oil-wet	45.95	2011.04	2.81
3	strongly-oil-wet	58.71	2544.83	3.40
4	strongly-oil-wet	67.27	2903.43	4.05
5	strongly-oil-wet	72.15	3107.50	3.95
6	strongly-oil-wet	75.74	3257.73	4.21
7	medium-oil-wet	77.98	3351.35	5.86
8	strongly-water-wet	80.80	3469.78	4.07
9	medium-water-wet	83.02	3562.65	4.77
10	medium-oil-wet	84.37	3618.87	5.90
TS2	medium-oil-wet	16.48	782.52	4.10
1	strongly-oil-wet	0.01	0.00	0.87
2	strongly-oil-wet	0.78	1.11	5.97
3	medium-oil-wet	1.03	2.55	3.52
4	medium-oil-wet	1.45	7.27	3.34
5	strongly-water-wet	1.68	11.30	6.55
6	strongly-water-wet	2.10	22.54	4.86
7	medium-water-wet	2.69	47.51	2.13
8	N/A	0.00	0.00	0.00
9	strongly-water-wet	3.32	90.93	7.81
10	medium-water-wet	3.90	149.28	4.82
TS3	medium-water-wet	16.95	332.49	4.43

REFERENCES

- Al-Bazzaz, W. H., and Y. W. Al-Mehanna (2007), Porosity, Permeability, and MHR calculations using SEM and thin-section images for complex Mauddud-Burgan carbonate reservoir characterization, *Society of Petroleum Engineers*, SPE 110730.
- Al-Bazzaz, W. H. (2017), Classification of pore wettability, in preparation.
- Asquith, G., and D. Krygowski (2004), Basic well log analysis, second edition, *American Association of Petroleum Geologist and Society of Exploration Geophysics*, Methods in Exploration.
- Djebbar, T., and D. Erle (2004), Petrophysics, second edition, *Elsevier Inc.*
- King, P. R., G. P. Thrasher, K. J. Bland, P. Carthew, D. D'Cruz, A. G. Griffin, C. M. Jones, and D. P. Strogen (2010), Cretaceous-Cenozoic geology and petroleum systems of the Taranaki Basin, New Zealand. Digitally remastered version. GNS Science, Lower Hutt, *Institute of Geological & Nuclear Sciences monograph 13*.
- Marfurt, K. J., R. L. Kirlin, S. L. Farmer, and M. S. Bahorich (1998), 3-D seismic attributes using a semblance-based coherency algorithm, *Geophysics*, 63, 1150-1165.
- New Zealand Petroleum and Minerals (NZPAM) (2014), *New Zealand Petroleum Basins*, Ministry of Business, Innovation and Employment, Wellington, New Zealand, ISSN 2324-3988.

PAPER**II. RESERVOIR CHARACTERIZATION USING 3D SEISMIC ATTRIBUTES AND ASSISTED PETROPHYSICAL LOG ANALYSES WITH ARTIFICIAL NEURAL NETWORK**

Aamer Alhakeem^{1*}, Kelly Liu¹, Waleed Al-Bazzaz², Haidar Almubarak¹, and Stephen Gao¹

¹ Missouri University of Science and Technology, Rolla, Missouri, United States,

² Kuwait Institute for Scientific Research, Ahmadi, Kuwait

* Corresponding Author: aaaxb2@mst.edu

ABSTRACT

The Kapuni group, within the Taranaki Basin in New Zealand, is a potential petroleum reservoir with various geophysical data. To provide new constraints on reservoir characterization, we developed a procedure to integrate the petrophysical and geological data. The study includes building a sequential approach to identify and visualize geological features and facies within the stratigraphy, started by interpreting and correlating the regional geological data, 3D seismic, and well data. Seismic interpretation is conducted targeting the Kapuni group; mainly, the Mangahewa and Kaimiro formations. Structural maps, horizon slices, isopach, and velocity maps, supported by continuity and discontinuity attributes, i.e., spectral decomposition, inversion, and coherence are generated. Well log analyses are performed for facies and petrophysics identification. The attribute measurements are utilized to characterize the subsurface structure and depositional system such as fluvial dominated channels, lagoon, and shoreface sandstone. Root Mean Square (RMS), dip, azimuth, and eigenstructure

coherence attributes are integrated to generate a multi-attribute in 3D view. Overlaying different attributes in a single 3D view can significantly strengthen the summation of the outputs and support the seismic interpretation. The resulting multi-attributes volume of the Kapuni Formation is cropped to run Artificial Neural Network (ANN) models using feed-forward with back-propagation to train the models by utilizing all available logs and the core data as input/output. More than 40 crossplots are produced for the quality management of the ANN. The calculated porosity logs based on assumptions range to about 35%, while the lower resolute measured porosity based on lab records ranged to about 26%. The predicted logs based on the ANN resulted in accurate values that range to about 27% with high resolution. Finally, the C-sand reservoir is characterized by evaluating and modeling the porosity and the permeability using both predicted and calculated logs. In comparison, the predicted logs offer more realistic values than other logs since they are close to the core data values.

1. INTRODUCTION

Reservoir characterization using geophysical interpretation has been attracting attention to reduce exploration costs and enhance productivity (Chopra and Marfurt, 2007; Brown, 2011). The availability of numerous geological and geophysical data opened the door for the exploration researchers to apply the artificial neural networking or other different methods of machine learning (Hampson et al., 2001; Dorrington, 2004). Attribute analyses of the seismic data can boost the quantity and quality of the data (Herrera et al., 2006). With the increasing algorithmic attributes applied to the 3D post-stack seismic and petrophysical data, it is essential to use machine learning to optimize the exploration goal for better prospect evaluation (Hampson et al., 2000).

This study integrates the seismic attribute analyses with petrophysical interpretation using micrometer scale data (thin-sections). A consecutive workflow is designed for seismic interpretation and attribute mapping to identify fracture, horizon continuity, stratigraphy, facies, direct hydrocarbon indicators, and potential prospects. Petrophysical analyses in a morphological approach using digital thin-section images yield abundant petrophysical data for the reservoir characterization and modeling.

Among these integrated sequences of flow, quality management in both its primary aspects – Quality Control (QC) and Quality Assurance (QA) – is needed before the Artificial Neural Network (ANN) process. Crossplotting the available well logs and the predicted logs is useful for ensuring reliable results from the ANN. The main objective of this study is to develop an efficient sequential flow for reservoir characterization which can generate a property model that matches the real characteristics of the targeted prospect. In this study, we use the Maui Field in the Taranaki Basin in New Zealand that embraces the Kapuni group, which comprise the most productive formations in the country, including the Mangahewa Formation.

2. GEOLOGICAL SETTING AND DATA SET

The Taranaki Basin, a Cretaceous foreland basin, covers an area of about 330,000 km² mostly in the offshore along the west coast of the North Island, New Zealand (King et al., 2010). Sediments fill up to about 9 km in the basin (Figure 1a). The basin consists of four main sequences, i.e., the Late Cretaceous Pakawau group, the Paleocene-Eocene Kapuni and Moa groups, the Oligocene-Miocene Ngatoro and Wai-it groups, and the Plio-Pleistocene Rotokare group (Figure 1c).

2.1. KAPUNI GROUP OF MAUI FIELD

The Maui Field is bounded in the west by the reverse Whitiki Fault and in the east by the normal Cape Egmont Fault (Figure 1). The Maui sub-basin is considered as the main source of the hydrocarbon that migrated into the Maui Field. A wide range of lithofacies is presented in the Taranaki Basin. We focus on the Eocene Kapuni which comprises three main formations, i.e., the Mangahewa (C-sand), Kaimiro (D-sand), and Farewell (F-sand) (King et al., 2008). The deposition environments of the Kapuni Group consist of coastal plain, marginal marine, and shallow marine to offshore that formed the thick sandstone layers. The coastal plain environment encounters the fluvial channel, overbank, and Marsh/floodplain facies. The marginal marine environment contains facies including estuarine, distributary, tidal channel beach, back beach, back-barrier bar, tidal sand-bar, flood tidal-delta sandflat, mudflat, embayment, and lagoon. The shallow marine depositional setting encounters shoreface, shoreline, and mouth-bar facies. The offshore deposited shelf mudstone, storm-generated sandstone, and offshore barrier facies (Table 1) (King et al., 2008). Coals in the Pakawau and Kapuni groups are considered as the most potential petroleum source rocks in the Taranaki Basin.

2.2. 3D-MAUI DATA SET

Figure 2 shows the workflow which illustrates all available data used in the study. The 3D-Maui post-stack seismic survey consists of 889 inlines and 1258 crosslines with bin spacing of 25 m, Two Way Travel Time (TWT) records have a length of 5.5 s, sampling rate of 2 ms, traces number of 869588, minimum amplitude of $-1.38E+07$, maximum amplitude of $1.38E+07$, and mean amplitude of 302907 (NZPM, 2015). The New Zealand Transverse Mercator 2000 (NZTM2000) projection coordinate system is

used to map the seismic survey and the well data (Figure 3). Composite well data comprises well headers, logs, thin-section (TS), and core data (Tables 1 and 2) (NZPM, 2015). The well data include core data with measured porosity, permeability, and grain density for five wells.

3. SEISMIC INTERPRETATION

The seismic data is interpreted to gain a general understanding of the structural features for characterizing the target geological subsurface layers. In this study, the Kapuni group formations are targeted, mainly the Mangahewa C-sand and Kaimiro D-sand.

3.1. WELL TO SEISMIC MATCHING

As illustrated in the workflow (Figure 2), the interpretation of the seismic data begins with matching the well data (depth domain) with the seismic data (time domain) by generating the synthetic seismogram (Figure 4). The components required to generate a synthetic seismogram include time-depth (T-D) chart, sonic (DT) logs, density log (DENS), and wavelet (Figure 4). A zero-phase wavelet of 2 ms sample interval and 0.1 s length is extracted from the seismic data from the surrounding area of 250 m diameter from each well. To match the synthetic seismogram with the seismic data, different seismic attributes were generated to support the identification of the Kapuni tops. Post-stack inversion (Figure 5a) is useful for lithological understanding, especially for a widely studied layering with a good geological background such as the Kapuni group. Moreover, 80 Hz spectral decomposition (SD) attribute is used for its strong continuity feature viewing of the seismic horizons (Figure 5b). Semblance-based coherence attribute

is obtained to show the effect of the faults and fracture for both the horizontal and vertical sections of the seismic data (Figure 6) (Marfurt et al., 1998). The generated synthetic seismogram is placed on the seismic attributes to be matched with the well logs and ensuring reliable interpretation (Figure 7).

3.2. HORIZON AND FAULT INTERPRETATION

Horizon and fault tracking are conducted to obtain an overall view of the structural impression on the target horizons. Tracking the target Mangahewa C-sand (top of Kapuni) leads to the generation of the structure maps. Horizon and fault interpretation requires picking a reflection event – of continuity for the horizon and of discontinuity for the fault – across the seismic survey. Interpreting the specific events yields time and amplitude values of horizon maps. Therefore, the interpreted horizon is a composite of different traces varying in time and amplitude values for a specific layer. Faults are represented by discontinuities in horizontal seismic events. By tracing these discontinuities, major faults are interpreted with the support of the coherence attribute (Figure 6c). Time structure maps are constructed from the tracked horizon surfaces by applying the gradient projection gridding algorithm. This process computes X and Y derivatives at every data sample location. In addition, it allows projecting an interpolated value at a grid node using an inverse distance to a power weighting (Figure 8a). Similarly, the horizon amplitude slice maps are generated for the C-sand (Figure 8b). Furthermore, for more realistic results, depth surface maps are obtained by correlating time structure with the velocity surface that is computed by the integration of DT, T-D, FT, and time structure surface. The average velocity surface and depth structure surface are shown after gridding in Figure 8, sequentially.

3.3. ATTRIBUTE ANALYSES

Surface and volume seismic attributes are generated for structural, stratigraphical, potential prospect evaluations, and data preparation for the reservoir modeling. For structural evaluation, we generated the structure (Figure 8a and 8d) and coherence (Figure 6) attributes. For stratigraphical evaluation, amplitude slice, average velocity, root mean square (RMS), and isochron attributes are generated (Figure 8b, 8c, 8e, and 8f). Additionally, multi-attributes are generated for integrated evaluation and reliable interpretation. These attributes comprise of the dip and azimuth maps, eigenstructure-based coherence volume attributes that improve the coherency with the structural dip (Figure 9a and 9b) (Gersztenkorn and Marfurt, 1999; Marfurt et al., 1999). Multi attributes are integrated into a 3D structure view of eigenstructure-based coherence and amplitude volume attribute (Figure 9c). This multi-attribute view identifies a volume of consistent structure and stratigraphy within the reservoir. The interval velocity volume attribute is also generated to prepare for the petrophysical modeling.

4. PETROPHYSICAL ANALYSIS

The composite well data, such as sonic log and resistivity log, are measured by various logging instruments (Table 2) among which petrophysical parameters comprising the porosity (Φ) and permeability (K) are of high and decisive value for their direct influence on the quality of petroleum reservoirs. The most reliable method to obtain Φ and K measurements is the core laboratory analysis. There are also theoretical means for petrophysical calculation using measured well logs to obtain a useful estimation (Asquith and Krygowski, 2004). Studying the thin-section images of the well core samples using a morphological approach can provide a realistic estimation (Al-Bazzaz and Al-Mehanna,

2007) (Figure 10 and Table 3). The goal of petrophysical analysis in this study is to develop a methodology to combine the log calculated with the measured core data, by processing the available data as “big data” to extract valuable hidden information and patterns. As a result, reservoir property modeling can ensure better characterization.

4.1. PETROPHYSICAL LOG CALCULATION

Petrophysical well log analyses are conducted by using DENS, NEUT, resistivity, GR, and SP logs to calculate the porosity and permeability (Perm) logs (Asquith and Krygowski, 2004). The study uses basic calculations of the petrophysical parameters to show how this calculation can be enhanced for better results using ANN. Clay volume log (Vcl) is computed from GR or SP, and corrected by crossplotting DENS with NEUT, which is useful for lithology and facies evaluation (Figure 11). Moreover, the porosity log (PHI) can be computed from DT, DENS, or NEUT/DENS logs. Table 4 shows some estimated parameters used for these calculations. Density matrix log (RhoMat) is calculated from Vcl for better PHI calculation. Water saturation log (SW) and flushed zone water saturation (SXO) are calculated using the Archie equation with both resistivity R_w and R_t . Bulk volume water log (BVW) is calculated from both PHI and SW for showing the amount of water in the rock in a schematic display. The porosity can be calculated in different pore classes to have effective porosity log (PHIE) or total porosity (PHIT). The permeability log (Perm) is derived from the relationship between the water saturation and the porosity using the Wyllie-Rose (1950) and Timur (1968) method (Asquith and Krygowski, 2004). Finally, the petrophysical calculation results are plotted in Figure 12 for three different wells.

Additionally, Phi and Perm are measured at their native selected spaces according to the method proposed by Al-Bazzaz and Al-Mehanna (2007) (Figure 10 and Table 4), using the morphological analysis of the thin-sections to provide spatial measurements along the wellbore. The pore networks of the available thin-section images are studied in the space domain between a lower bound of 50 μm and an upper bound of 4 mm.

4.2. PETROPHYSICAL LOG PREDICTION

Artificial Neural Network (ANN) is an effective tool for well log prediction (Hampson et al., 2001; Dorrington, 2004; Herrera et al., 2006). In this study, petrophysical logs are predicted by training the ANN model using the available core data of both the porosity (CoreP) and permeability (CoreK) to predict the porosity (PHInn) and permeability (Knn) logs (Figure 13). ANN works as a universal function approximator that can estimate the non-linear relationship between the input and the output.

The process consists of two stages – the feed-forward stage, and the back-propagation stage. The input is presented as a vector or matrix X . In the feed-forward stage the vector/matrix X is multiplied by a set of weights in the matrix W_1 . The output of this matrix multiplication is passed into a non-linear function (hyperbolic tangent). The result is multiplied by another set of weights W_2 and then passed into another non-linear function. The output is compared to the true value y that corresponds to the input and the Mean Squared Error (MSE). The calculated MSE is used to tune the set of weights W_1 , W_2 by back propagating the error and multiplying it by the derivative of the non-linear function with respect to the input X . The process is repeated multiple times until a satisfactory MSE is reached or a predefined number of runs is passed.

In the example shown in Figure 13, the following log properties were used as input to the ANN: GR, DENS, NEUT, PHI, and DTC. They are arranged as a vector/matrix X . The output that we are trying to predict is porosity log (PHInn). The input to the ANN (the log data values) X is multiplied by the hidden layer weights W_1 and the result is fed to the function $f_1 : \Leftrightarrow \tanh$ to produce the activation (hidden layer output) A

$$A = f_1(W^T X),$$

where T is the matrix transpose. The output of the hidden layer A is multiplied by the output layer weights W_2 and the result is fed to the function $f_2 : \Leftrightarrow \tanh$ to produce the ANN output PHInn

$$PHInn = f_2(A^T W_2)$$

To calculate the error (E) of ANN prediction we need to compare it to the real CoreP data

$$E = \frac{1}{2} \|PHInn - CoreP\|_2^2$$

The weight needs to be updated to minimize the error using the following equation

$$W = W - \alpha w \frac{\partial E}{\partial W},$$

where W is the weight to be updated, αw is the learning rate, and $\partial E / \partial W$ is the partial derivative of the error with respect to the weight being updated. The error is

propagated from the output layer back to the hidden layer. To get the error due to the output layer weight W_2 , the following are conducted.

$$\begin{aligned}\frac{\partial E}{\partial W_2} &= (PHInn - CoreP) \frac{\partial PHInn}{\partial W_2} \\ &= [(PHInn - CoreP) \circ f_2'(W_2 A)] \frac{PHInn}{\partial W_2} \\ &= [(PHInn - CoreP) \circ f_2'(W_2 A)] A^T\end{aligned}$$

where \circ is the element wise multiplication.

$$\text{let } \delta_2 = [(PHInn - CoreP) \circ f_2'(W_2 A)] A^T$$

$$\frac{\partial E}{\partial W_2} = \delta_2 A^T$$

similarly for W_1 we have

$$\begin{aligned}\frac{\partial E}{\partial W_1} &= [W_2^T \delta_2 \circ f_1'(W_1 X)] X^T \\ &= \delta_1 X^T\end{aligned}$$

An ANN model is trained using the stochastic gradient decent (sgd) algorithm by minimizing the mean square error (mse) between the true values $train_y$ and the output produced by the network using $train_x$ as input. After the training the weight matrices (W_1, W_2) from the model along with the activation function are used to predict on the test data.

The process, by itself, yields no output unless there is a relation between the input that allows the ANN to invest and start learning in the neural network training (NNT) stage to organize for the neural network modeling (NNM) stage (Figure 2). Thus, data

preparation is run by resampling and cropping a particular reservoir with close specifications to inquire reliable inputs for realistic outputs. Quality management during the ANN process ensures the appropriate relation between the input and the porosity/permeability logs. Quality Control (QC) is conducted to examine the quality of the core data measured (Figure 14a) and to ensure that the nominated logs for ANN are related to Phi and Perm with good correlation coefficient (R) of more than 0.7. Table 5 lists about forty QC crossplots that have been examined to nominate logs with Phi and Perm. Figure 15 illustrates samples of the QC crossplots with good R except for Figures 15f, 15g, and 15j, which have been ignored for their specific well and specific log. Then, each group of logs that passed the QC is used as the input of the ANN model for the wells. ANN models are listed in Table 6. The ANN model resulted in the porosity predicted log (PHInn) and the permeability predicted log (Knn). The predicted logs are tested for Quality Assurance (QA) by the crossplots listed in Table 5. Figure 14b shows the improvement in quantity of the predicted petrophysical data with preserving the quality of the measured data. Figure 16 demonstrates samples of the QA crossplots, showing good matching quality in the predicted logs to be ready for the reservoir property modeling.

5. RESERVOIR CHARACTERIZATION

Constructing the petrophysical model is aimed at providing a reservoir characterization for the defined Mangahewa C-sand reservoir. A sequence of flow is constructed by incorporating all of the previous seismic interpretations and well log analyses to create comprehensive models (Herrera et al., 2006; Chopra and Marfurt, 2007; Brown, 2011). Figure 17 shows a result-based workflow diagram. The structural

framework in the time domain is assembled using 16 interpreted horizons including the Mangahewa C-sand and Kaimiro D-sand, and six major fault surfaces of the Maui Field (Table 7). By combining this with the velocity model (Figure 17b), the whole framework is converted to depth domain and matches with all the horizon and fault interpretations, forming a background model of the respective layers and structure (Figure 17c and Table 8). In Figure 17d, the structural grid model is built by defining the model to cells of I, J, and K grid directions (Table 9). The calculated and the predicted logs are upscaled by averaging the values for each grid cell penetrated by well logs (Figure 17e). Cell arithmetic mean is applied to upscaling the porosity logs, while for permeability logs, the harmonic mean is applied (Table 11). In Figure 18, petrophysical logs resulting from the Neural Network Model (NNM) are illustrated and compared with the calculated logs and the upscaled logs for both the predicted and the calculated logs. Finally, a stochastic algorithm of sequential Gaussian simulation is applied to build the petrophysical property model after running geostatistical data analysis (Figure 17f). In Figure 19a, porosity models of the Mangahewa C-sand reservoir are demonstrated for the predicted PHInn logs of values ranging between 0% and about 25%. Figure 19b shows the same model of PHInn, but with filtering porosity values of less than 20% to compare with the calculated PHI model in Figures 19c and 19d that have a value range between 0 and 35%. The statistics obtained for the porosity models are listed in Table 11. Moreover, predicted and calculated permeability models of the Mangahewa C-sand reservoir are illustrated in Figure 20. 200 mD values and lower of the permeability are filtered and modeled using both Knn and Perm logs (Figure 20b and 20d). The permeability model statistics (Table 11) shows better standard deviation (std) values for the predicted than the calculated.

6. CONCLUSIONS

The study implemented prospect analysis and reservoir characterization of the Maui B-area. The SD, inversion, and coherence attributes were analyzed and used successfully for seismic-well-tie. RMS, dip and azimuth, and eigenstructure-based coherence attributes were useful tools for optimizing the results predicted and for stratigraphy and prospect analyses. The workflow included calculating and predicting the petrophysical logs after identifying the study boundary. Multi-attribute analyses helped to cluster attributes for eventual evaluation including structure, fracture, stratigraphy and bright spot for geometrical boundary identification of the model. The study provides constraints for future exploration and drilling, and for developing attributes to identify the potential prospects and using available seismic and well data.

The neural network model that generates the pseudo porosity volume can be distributed along a structured grid model for optimizing the reservoir characterization. The porosity logs of the Mangahewa C-sand are predicted for 25 wells, with the measurements close to the core porosity that ranged between about 0 and 25%, while the calculated porosity logs ranged between 0 and 37%. The std values for the predicted permeability are about 1250 mD, while they are 5271 mD for the calculated permeability model, indicating good improvement. In summary, the study provides criteria for quality management of ANN.

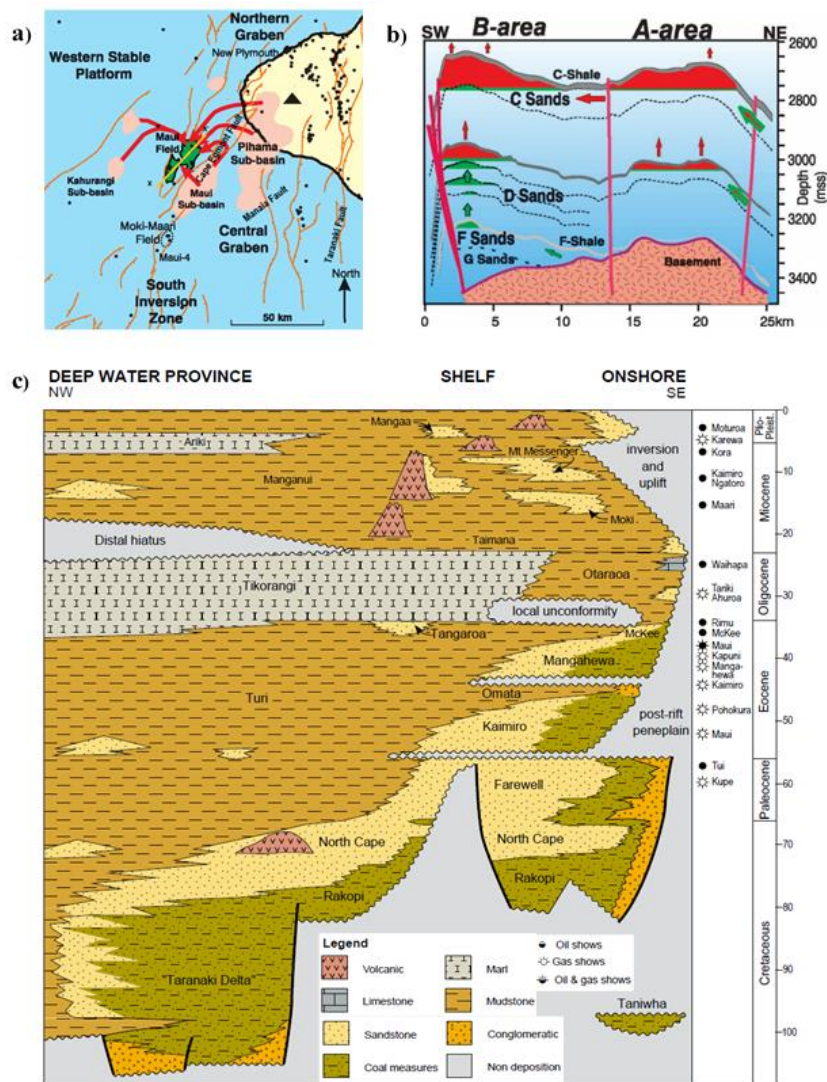


Figure 1. Geological settings in the study area. (a) Map showing the main fault systems and sub-basins with an indication of petroleum source rock of the Maui Field in the Taranaki Basin (Funnell, 2004). (b) Vertical section of the yellow line (X-X') crossing the Maui Field in Figure 1a showing the stratigraphy and reservoirs of the Kapuni Group for both the Maui A-area and Maui B-area. The Whitiki Faults (west of Maui) and the Cape Egmont Fault system (south-east, mid-east, and east of Maui) are illustrated (Funnell, 2004). (c) Cretaceous - Cenozoic stratigraphic framework for the Taranaki Basin (NZPAM, 2014).

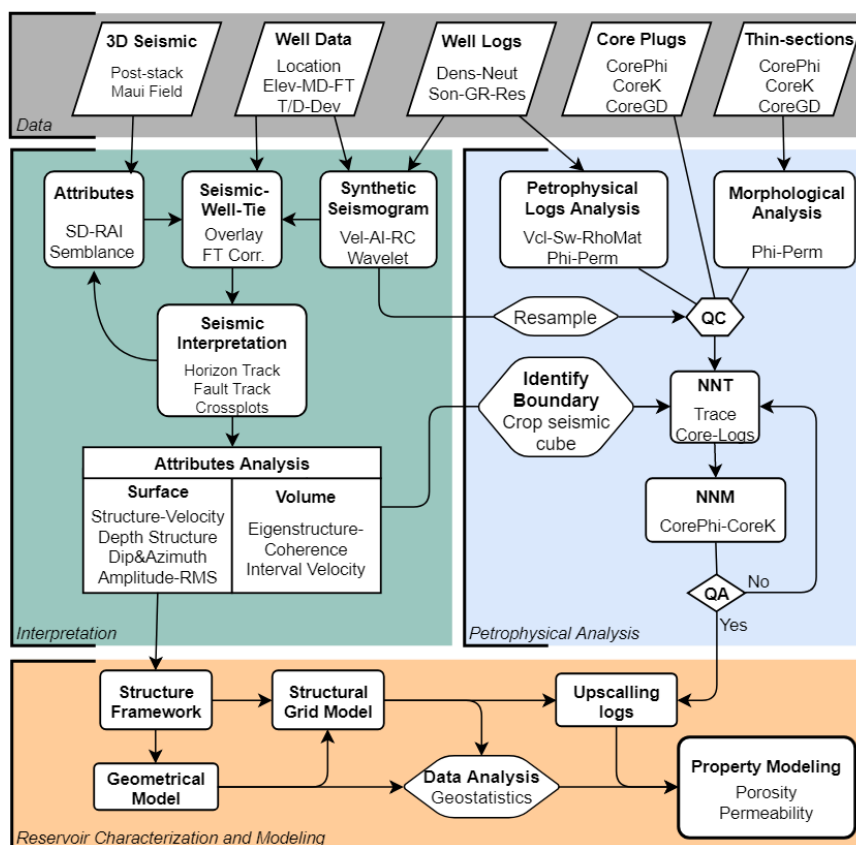


Figure 2. Workflow of the study. It comprises four main processes, i.e., data preparation, seismic interpretation and attribute analysis, petrophysical analysis and ANN, and reservoir characterization and modeling.

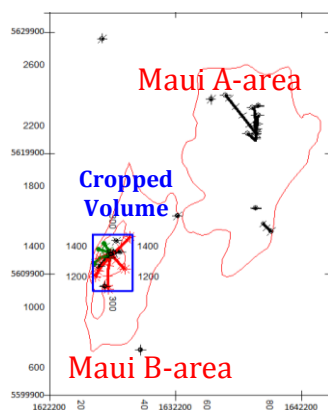


Figure 3. Basemap of the 3D-Maui seismic survey and well data used in this study. The Maui A-area and Maui B-area fields are bounded by the red line. The cropped volume area in blue is used for the petrophysical model of the Maui B-area targeted reserve (NZPM, 2015).

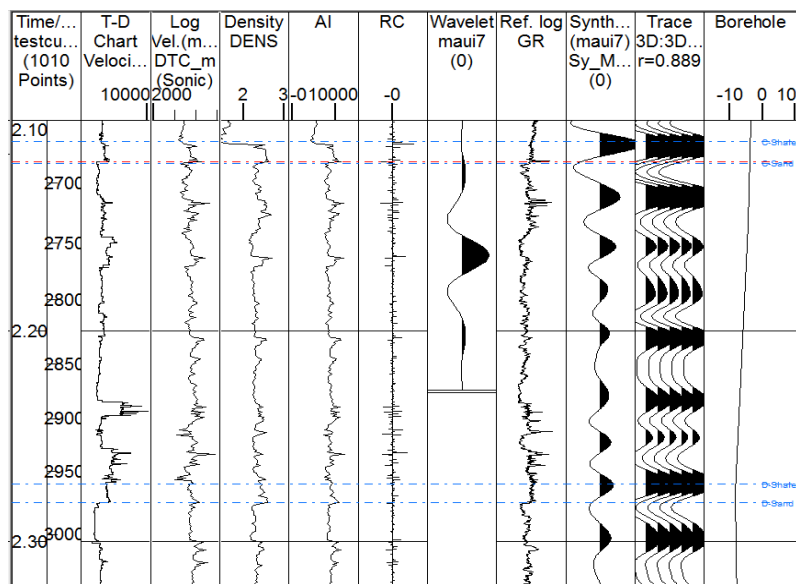


Figure 4. Synthetic seismogram generation for Well Maui-7. The components used and the synthetic seismogram generated are illustrated. The cross-correlation coefficient between the seismic trace and the synthetic seismogram (r) value is 0.889 indicating a good match between the synthetic seismogram and the seismic trace.

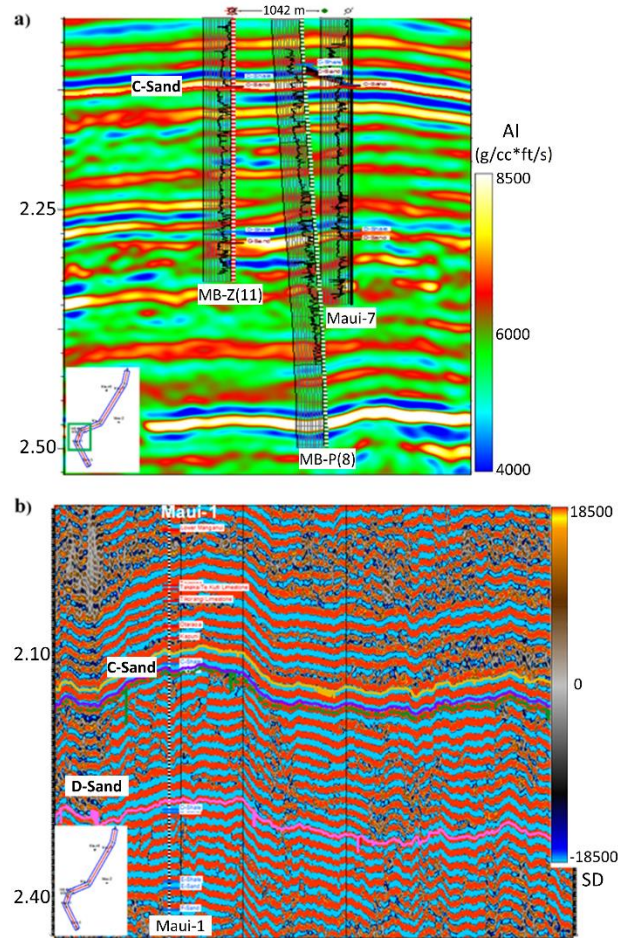


Figure 5. Seismic attribute sections for target horizon identification and tracking. a) Acoustic impedance (g/cc*ft/s) recursive inversion with AI logs overlies the wells for MB-Z(11), MB-P(8), and Maui-7 respectively. b) 80 Hz spectral decomposition attribute line illustrated in the basemap at the left corner. Horizon interpretation is indicated for C-sand in purple line and D-sand in pink line. The Maui-1 is shown with its formation tops for identifying the horizon.

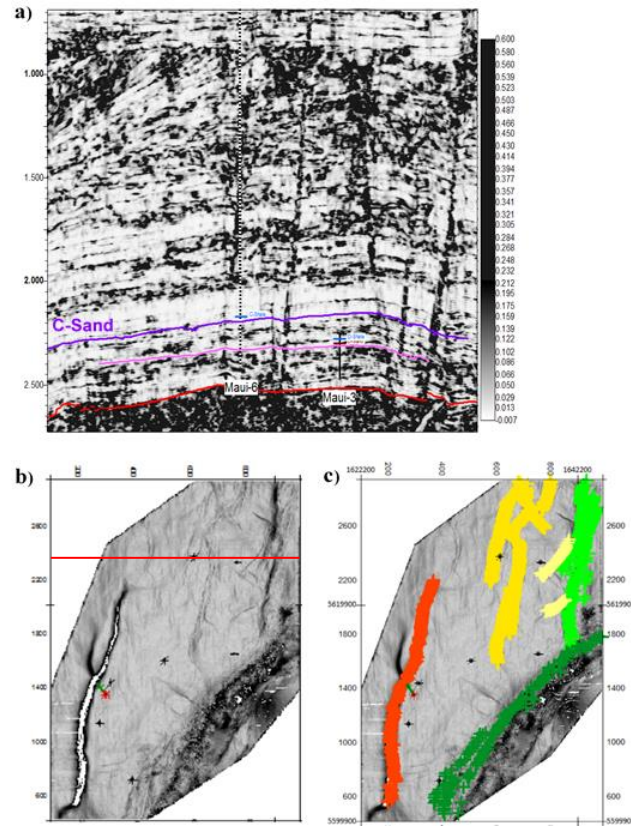


Figure 6. Attributes used for fault interpretation. a) Coherence vertical seismic section of crossline 2354 (red line in 6b) providing a great reveal of the faults crossing the targeted horizons of the Kapuni group. b) Horizontal section coherence of the Mangahewa C-sand horizon illustrated purple line in 6a. c) Coherence section of the C-sand showing the interpretation of The Whitiki Faults (red) and the Cap Egmont Fault System (yellow and green).

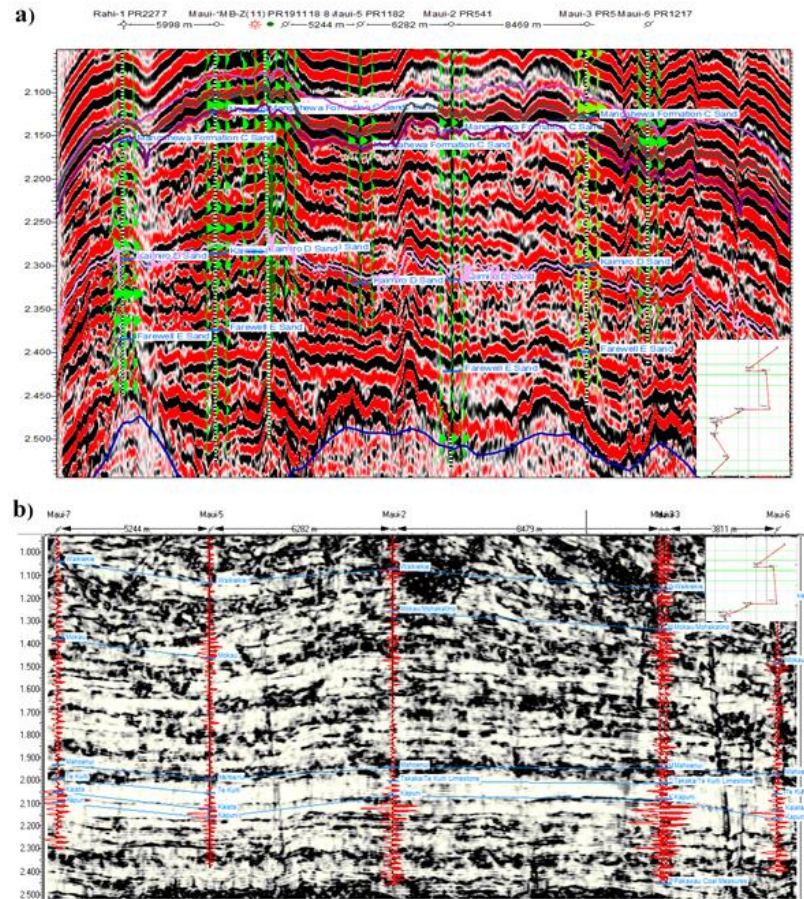


Figure 7. Synthetic seismogram overlay. a) Seismic section of the arbitrary line shown in the right corner. The synthetic seismograms generated for all eight wells are overlaid and matched with the seismic data. Horizon picking follows the seismogram tops for both C-sand and D-sand. b) Coherence section of the arbitrary line crossing six wells with synthetic seismic matching and formation top correlation to study the effect of the major fractures on the horizon continuity.

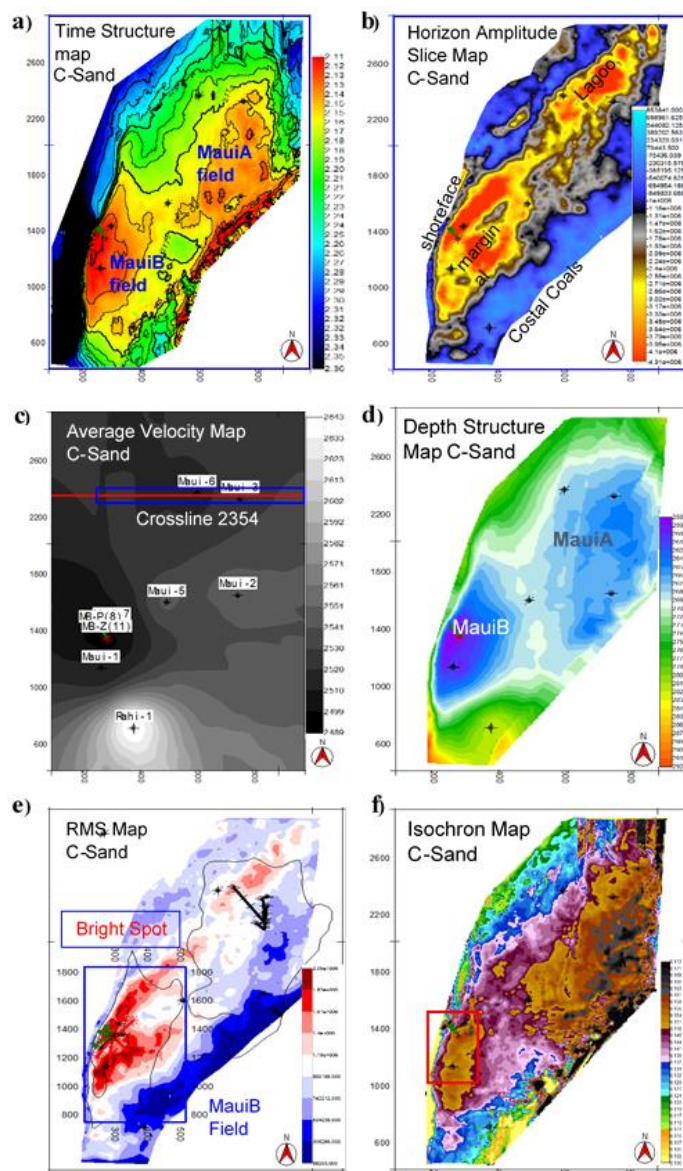


Figure 8. Attributes generated for the Mangahewa C-sand horizon. a) Time structure map shows two anticlines representing the Maui A-area and Maui B-area. b) Horizon amplitude slice map shown lagoon and tidal-flat marginal marine in red and coastal coals in Blue. c) Average velocity map shows a low value near the Maui B-area. The area near well Rahi-1 is characterized by high average velocity value. In the Maui A-area, the highest velocity value is around the Maui-6. d) Depth structure map shows the Maui A-area and Maui B-area anticlines. A dramatic dipping to the east-south of the Maui A-area and to the west-south of the Maui B-area caused by the fault system that surrounds the study area. The map shows a general dipping toward the north and north-east. e) RMS amplitude map shows a bright spot around the Maui B-area. f) Isochron map shows high-values within the Maui B-area that combined with the RMS results to ensure good prospective and to bound the reservoir consistency area for characterization evaluation for better attribute and petrophysical analysis.

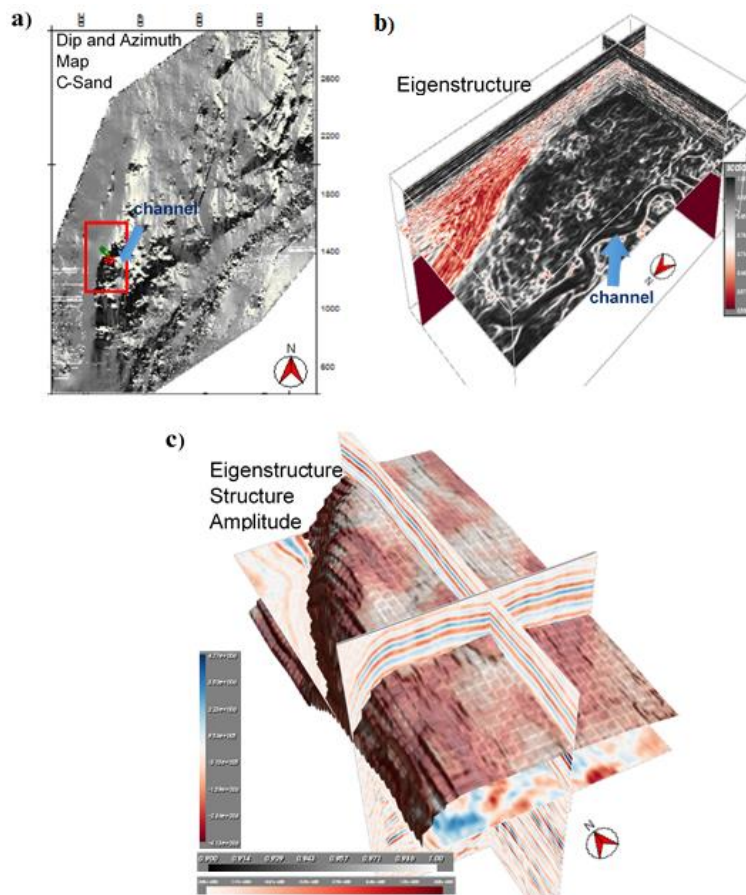


Figure 9. Multi-attribute crossplots providing better prospect, structure, and stratigraphy identification. a) Dip and azimuth map of the C-sand horizon used to improve the process of the coherency. b) 3D eigenstructure coherence cropped volume for the area outlined in red in Figure 9a. A channel is mapped successfully. c) The Mangahewa C-sand horizon visualized within a brick seismic volume integration of amplitude horizon (White-Red colorbar) and eigenstructure coherence transparency (black-white colorbar) in 3D seismic structure view.

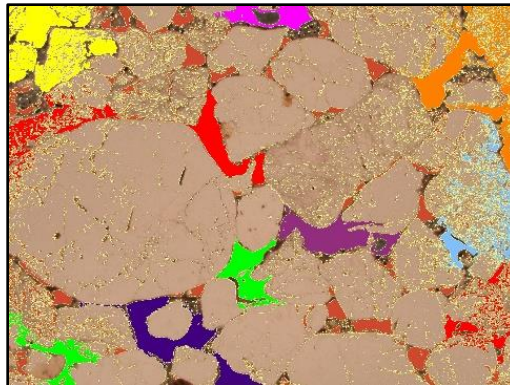


Figure 10. Thin-section (TS) sample. Mangaheha C-sand Maui-7 Depth: 2897 m showing the class identification of the pore area ranges applied to each thin-section of the study. Identification of ten area range classes starts with class one that ranges between 0–500 μm^2 with 500 μm^2 increment range increase for each class range up to class ten 5000–10000 μm^2 . Colors indicate the pores area range classification. TS width of view is 4000 μm . (Alhakeem et al., 2017).

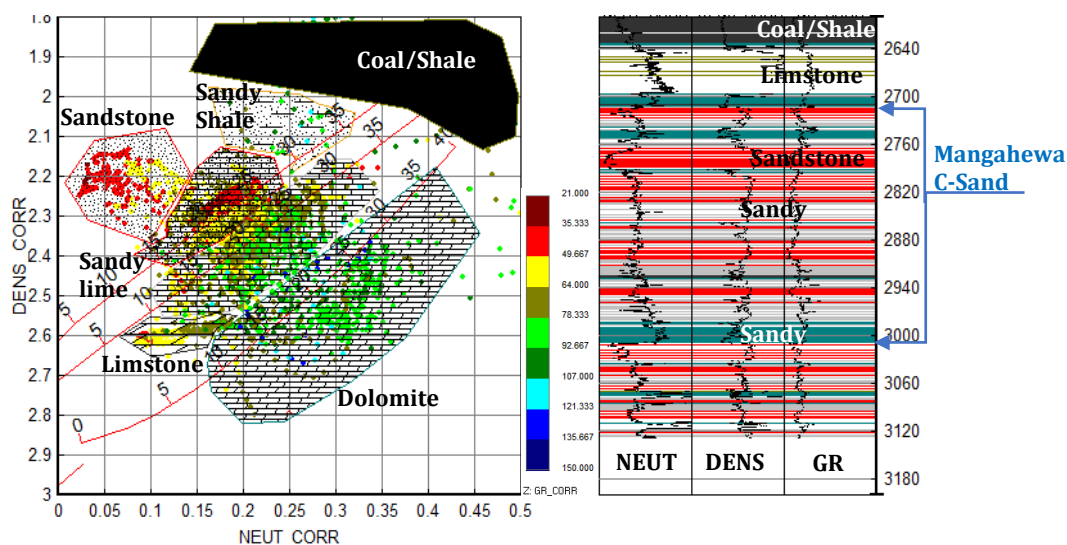


Figure 11. Crossplot of DENS versus NEUT with GR color-coded for facies interpretation to recognize the Mangaheha C-sand of for the Kapuni Group in Maui-7.

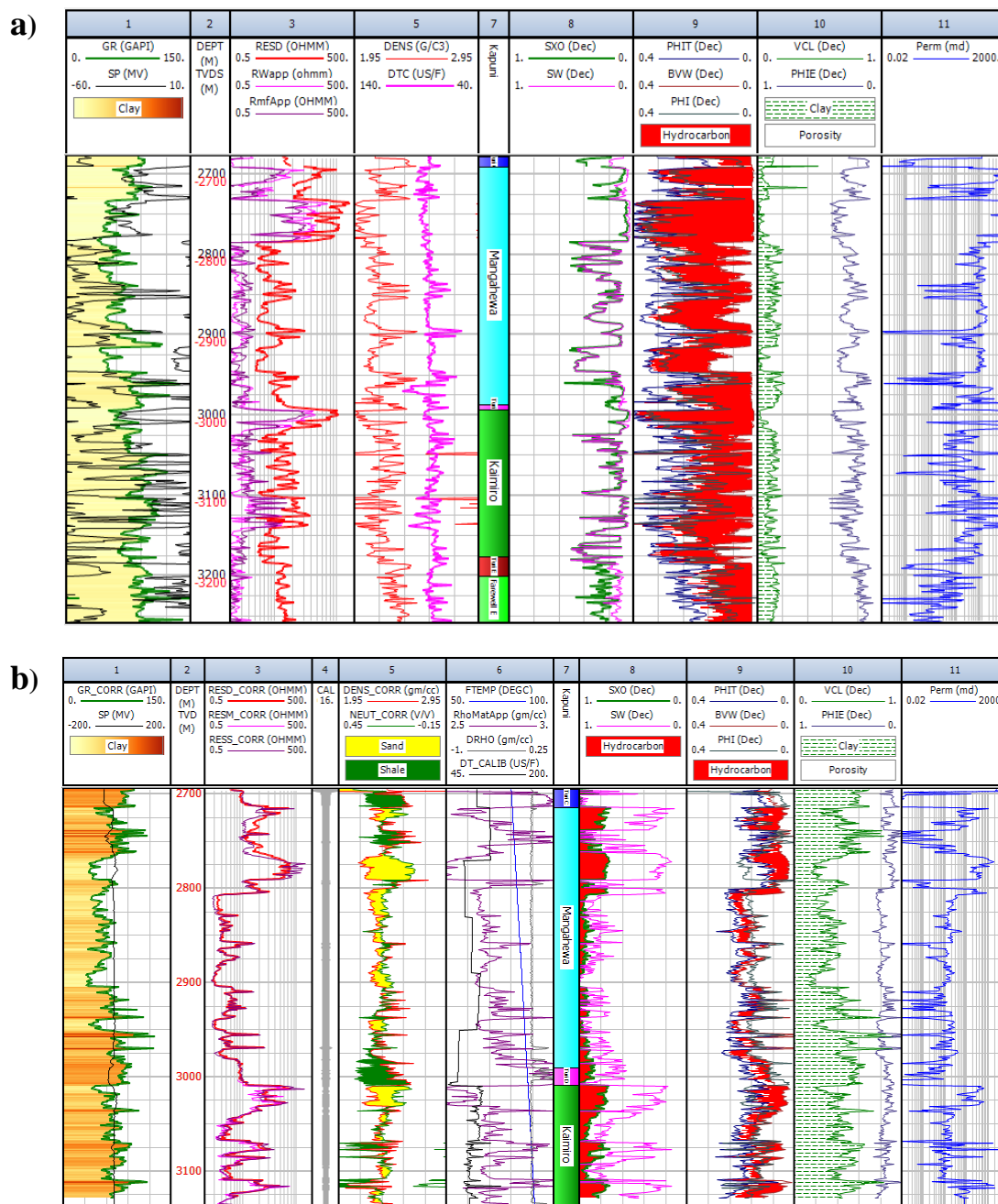


Figure 12. Petrophysical log interpretation of the Kapuni group. a) Maui-1 log analyses performed using GR, SP, RESD, RESM, RESS, DENS, NEUT, DRHO, RhoMatApp, DTC, and, FTEMP. The resulting logs are SXO, SW, PHIT, BVW, PHI, VCL, PHIE, and Perm. Track-8 shows the interpretation of hydrocarbon existence in red. b) Maui-7 log analyses performed using GR, SP, RESD, RWapp, RmfApp, DENS, and DTC. The resulting logs are SXO, SW, PHIT, BVW, PHI, VCL, PHIE, and Perm. Track-9 shows the interpretation of hydrocarbon existence in red. c) MB-P(8) log analyses performed using GR, SP, RESD, RESS, DENS, NEUT, DRHO, RhoMatApp, DTC, and, FTEMP. The resulting logs are SXO, SW, PHIT, BVW, PHI, VCL, PHIE, and Perm. Track-9 shows the interpretation of hydrocarbon existence in red.

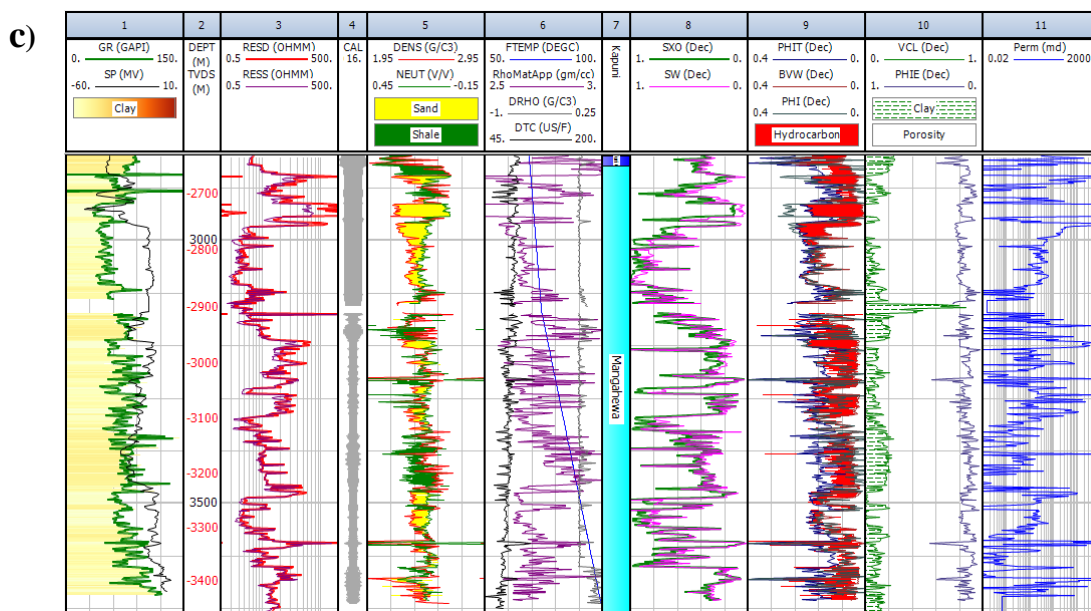


Figure 12. Petrophysical log interpretation of the Kapuni group. a) Maui-1 log analyses performed using GR, SP, RESD, RESM, RESS, DENS, NEUT, DRHO, RhoMatApp, DTC, and, FTEMP. The resulting logs are SXO, SW, PHIT, BVW, PHI, VCL, PHIE, and Perm. Track-8 shows the interpretation of hydrocarbon existence in red. b) Maui-7 log analyses performed using GR, SP, RESD, RWapp, RmfApp, DENS, and DTC. The resulting logs are SXO, SW, PHIT, BVW, PHI, VCL, PHIE, and Perm. Track-9 shows the interpretation of hydrocarbon existence in red. c) MB-P(8) log analyses performed using GR, SP, RESD, RESS, DENS, NEUT, DRHO, RhoMatApp, DTC, and, FTEMP. The resulting logs are SXO, SW, PHIT, BVW, PHI, VCL, PHIE, and Perm. Track-9 shows the interpretation of hydrocarbon existence in red (cont.).

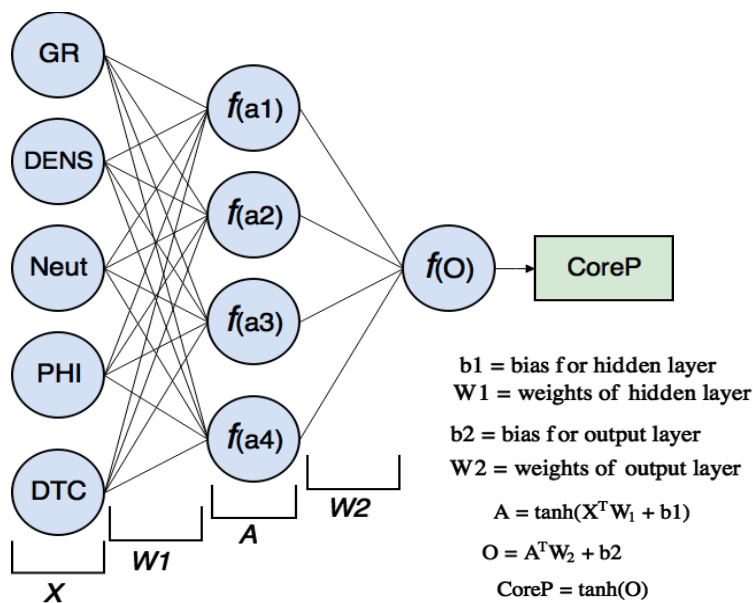


Figure 13. The feed-forward neural network structure of one hidden layer, with the input and output layers. First, the input layer of six neurons are the property logs used. Second, the hidden layer contains four nodes using the hyperbolic tangent activation function. The log analysis is performed using GR, SP, RESD, RESS, DENS, NEUT, and DRHO logs.

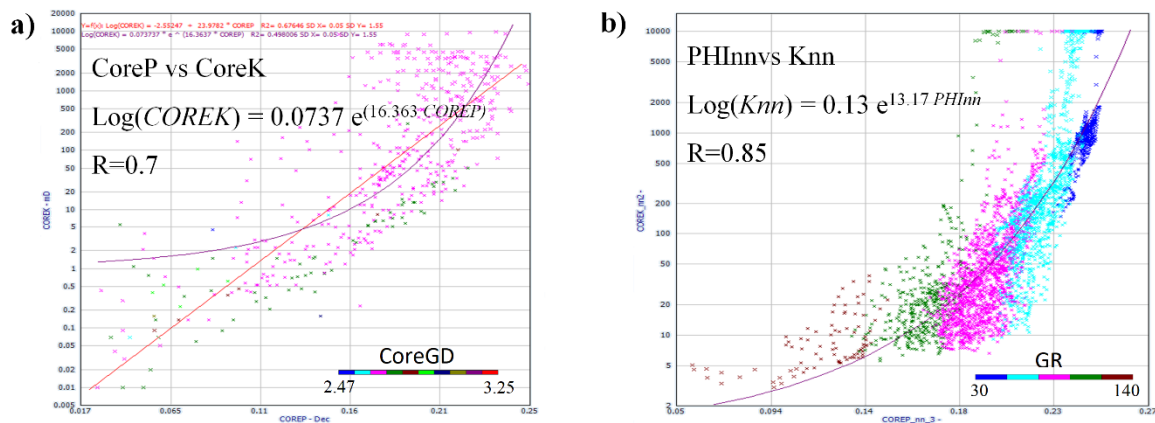


Figure 14. Crossplots of permeability and porosity. a) COREK and COREP that are used in the ANN model for Maui-7. b) Knn and PHInn that are predicted from the ANN showing a good correlation coefficient (R) of the exponential regression of 0.85 for Maui-1.

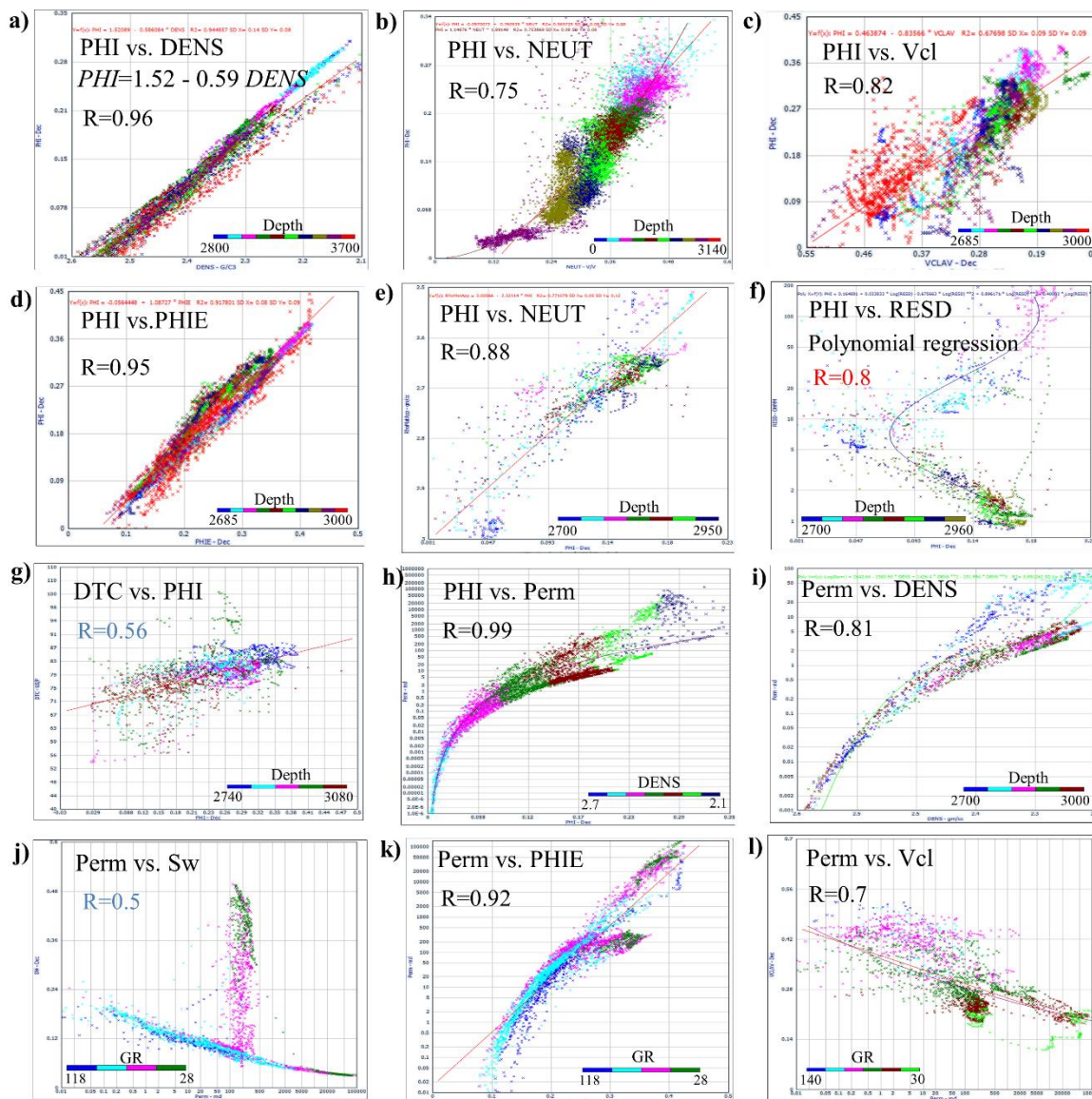


Figure 15. Quality control (QC) crossplots for both PHI and Perm calculated logs for the Mangahewa Formation. a) PHI vs. DENS with depth color-coded for MB-P(8). b) PHI vs. NEUT with depth color-coded for Maui-7. c) PHI vs. VCL with depth color-coded for Maui-1. d) PHI vs. PHIE with depth color-coded for Maui-1. e) PHI vs. RHOM with depth color-coded for Maui-7. f) PHI vs. RESD with depth color-coded for Maui-7. g) PHI vs. DTC with depth color-coded for Maui-1. h) Perm vs. PHI with DENS color-coded for MB-P(8). i) Perm vs. DENS with depth color-coded for Maui-7. j) Perm vs. SW with GR color-coded for Maui-1. k) Perm vs. PHIE with GR with color-coded for Maui-1. l) Perm vs. VCL with GR color-coded for Maui-1.

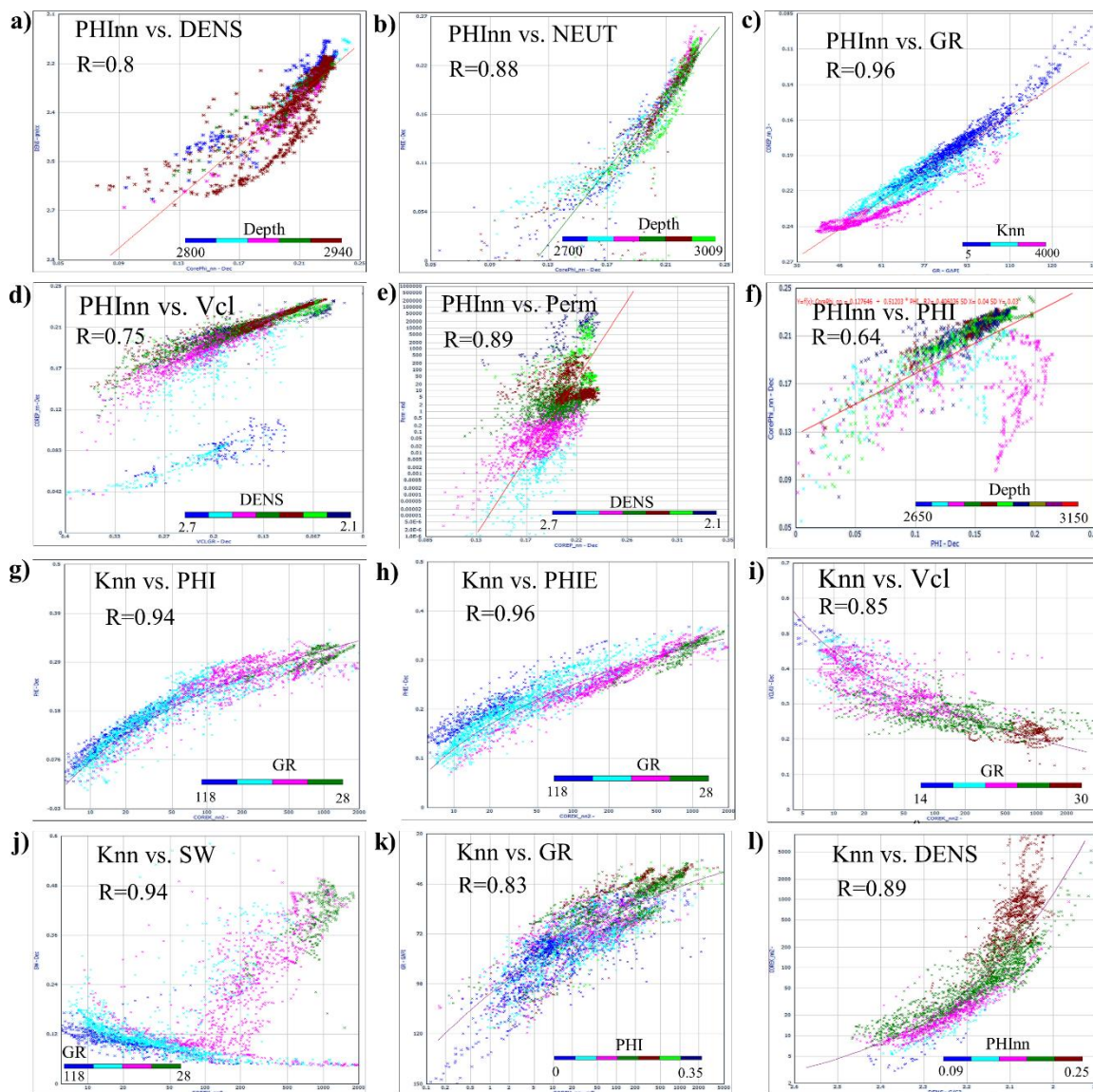


Figure 16. Quality Assurance (QA) crossplots for both PHInn and Knn predicted logs from ANN for the Mangahewa Formation. a) PHInn vs. DENS with GR color-coded for Maui-7. b) PHInn vs. NEUT with DENS color-coded for Maui-7. c) PHInn vs. GR with Knn color-coded for Maui-1. d) PHInn vs. VCL with DENS color-coded for MB-P(8). e) PHInn vs. Perm with DENS color-coded for MB-P(8). f) PHInn vs. PHI with depth color-coded for Maui-7. g) Knn vs. PHI with GR with color-coded for Maui-1. h) Knn vs. PHIE with GR color-coded for Maui-1. i) Knn vs. VCL with GR with color-coded for Maui-7. j) Knn vs. SW with GR color-coded for Maui-1. k) Knn vs. GR with PHI with color-coded for MB-P(8). l) Knn vs. DENS with PHInn color-coded for Maui-1.

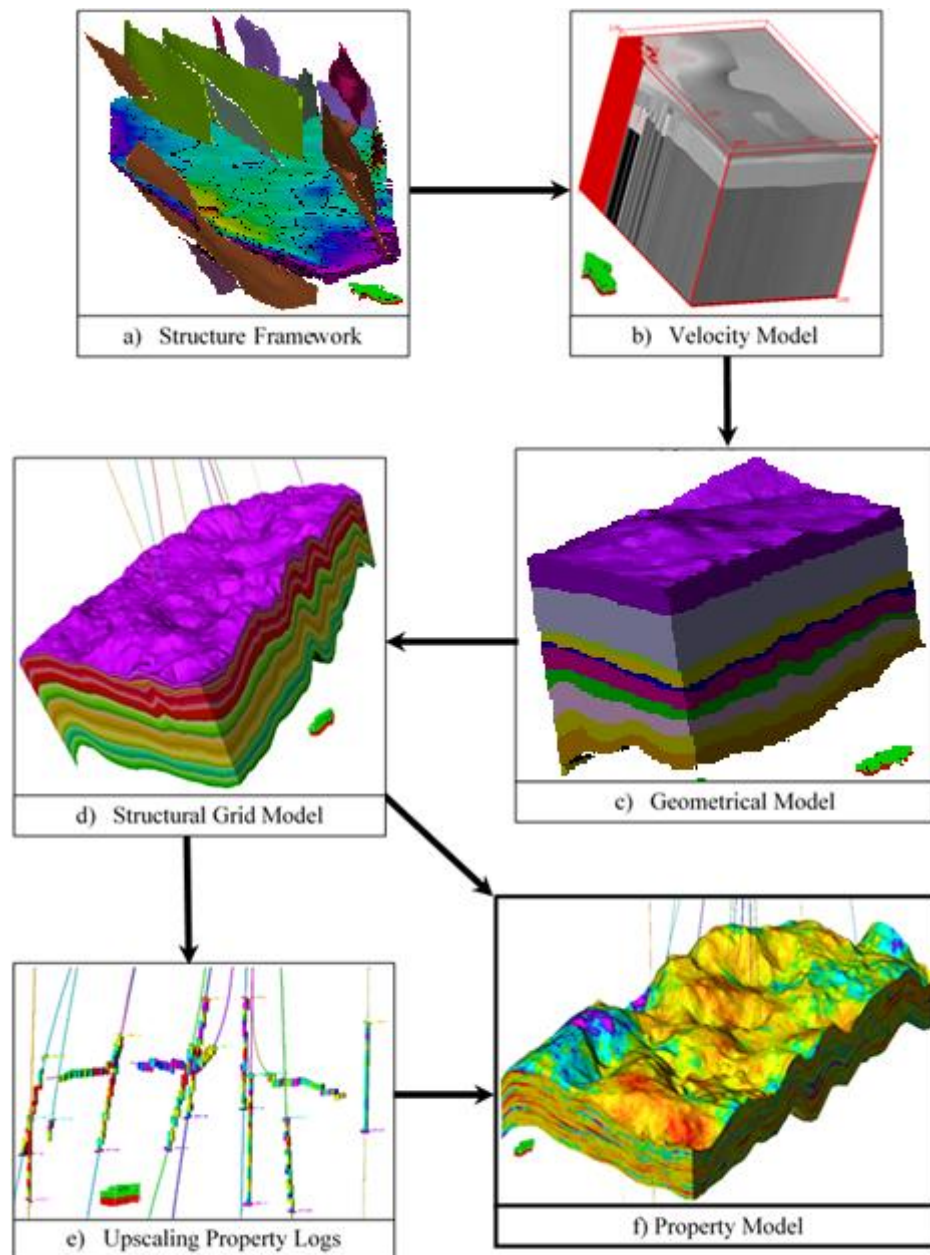


Figure 17. Sequence diagram flow of the petrophysical modeling. (a) Structural framework. (b) Velocity model. (c) Geometrical model. (d) Structural grid model. (e) Upscaling property logs. (f) Property model.

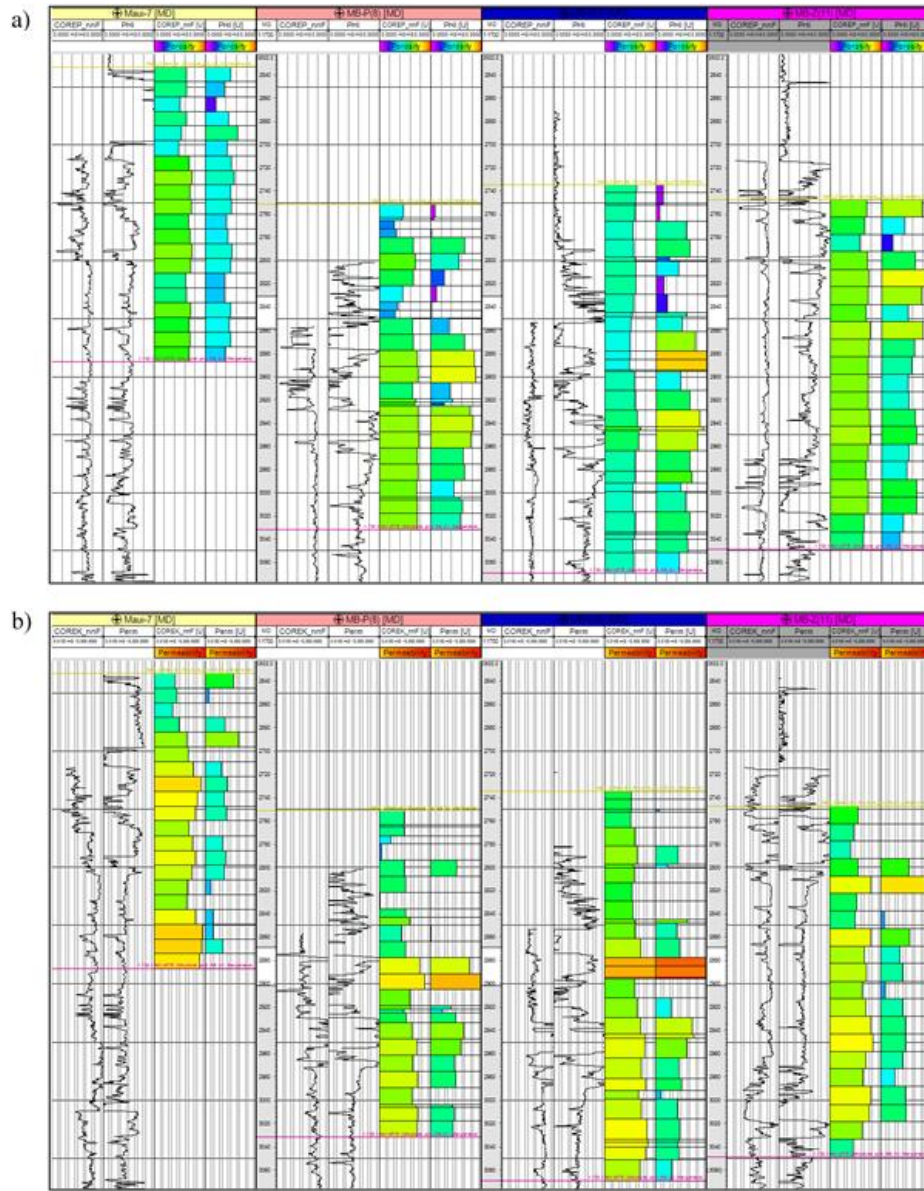


Figure 18. Petrophysical logs resulted from the NNM compared with the calculated logs and compared to the upscaled logs for both the predicted and the calculated logs. The Mangahewa C-sand Formation is bounded by yellow line (top) and pink line (bottom). Logs from the left are Maui-7, MB-P(8), MB-R(1), and MB-Z(11). Each log track illustrates consequently predicted log, calculated log, upscaled predicted log, and upscaled calculated log. a) Porosity logs. b) Permeability logs.

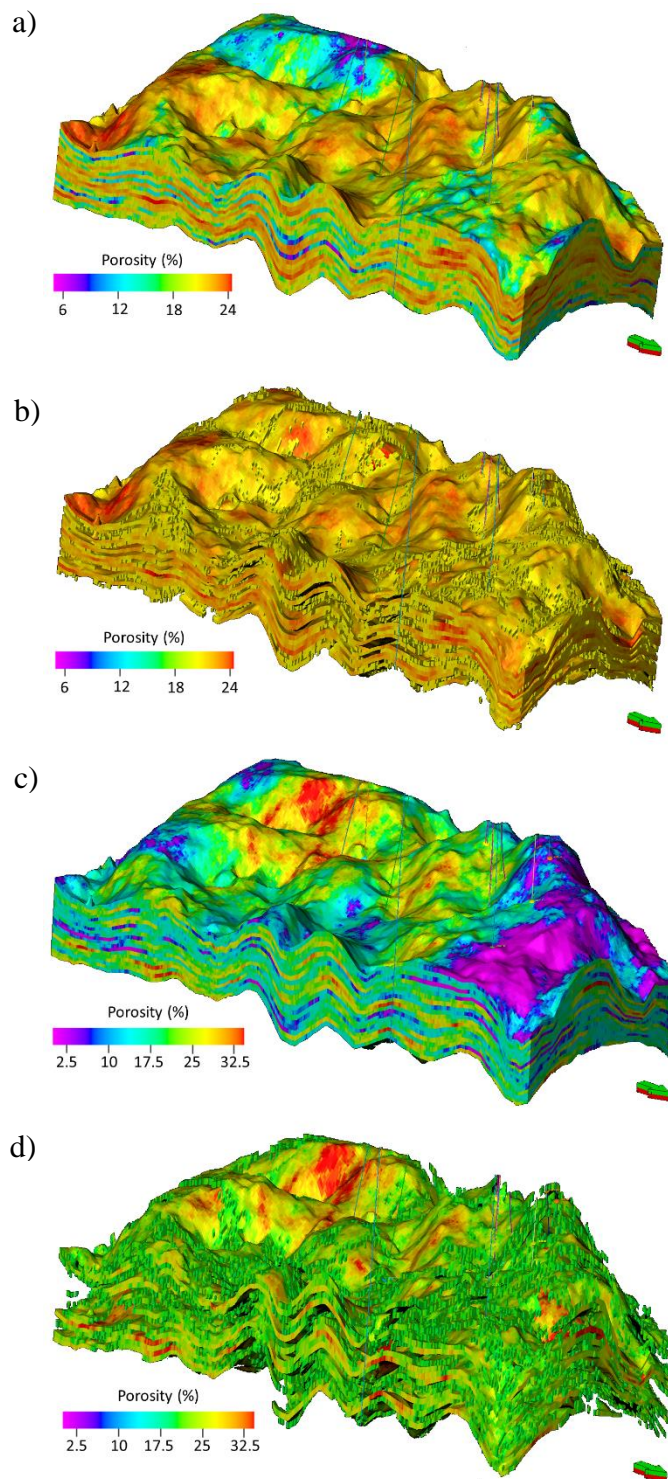


Figure 19. Porosity models of the Mangahewa C-sand reservoir within the Maui B-area.

a) Porosity model using PHInn logs. The porosity values range between 0% to about 25%. b) PHInn model with filtering values less than 20%. c) Porosity model using PHI logs. The porosity values range between 0% to about 35%. d) PHI model with filtering values less than 20%.

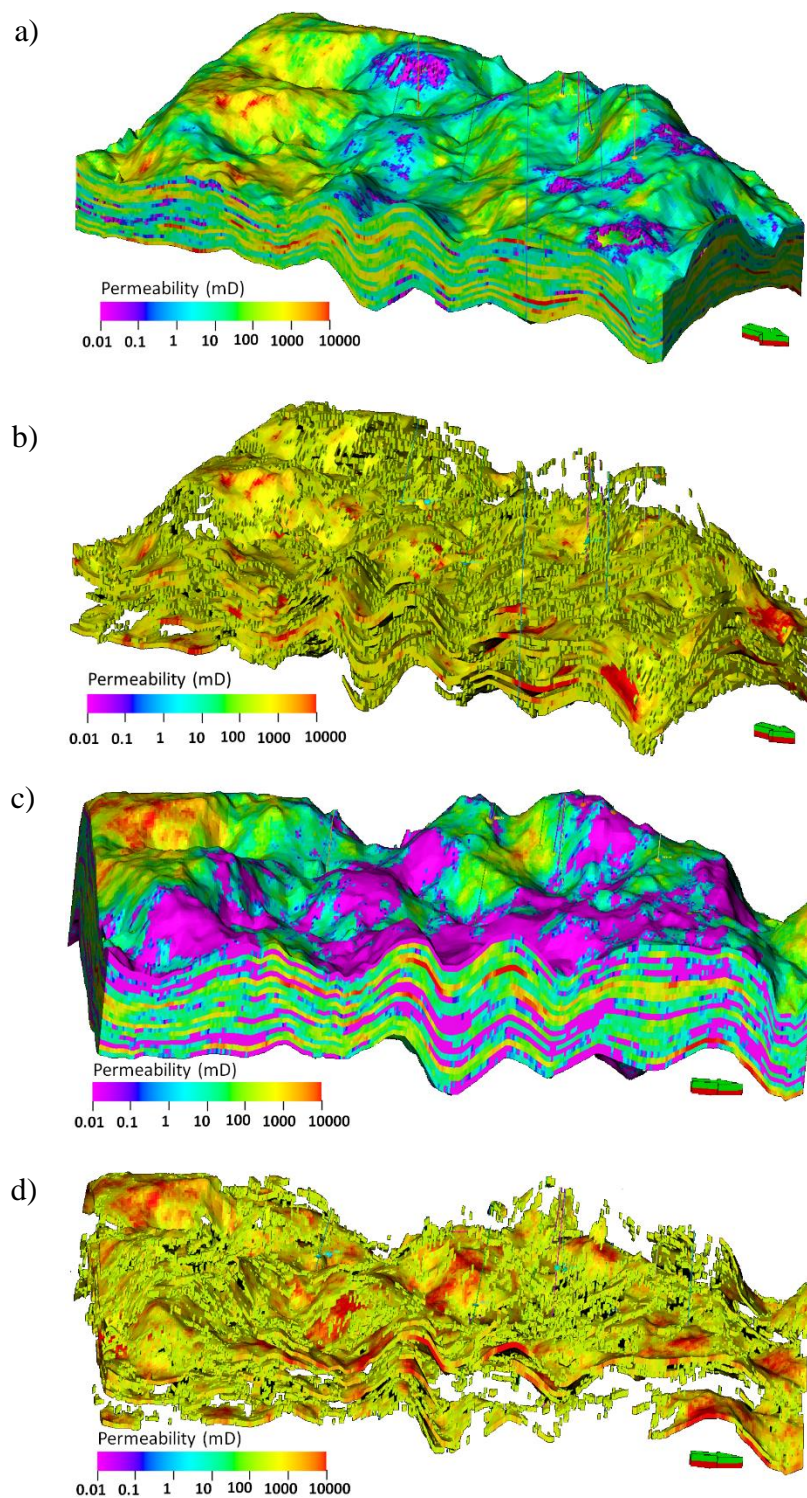


Figure 20. Permeability models of the Mangahewa C-sand reservoir within the Maui B-area. a) Permeability model using Knn logs. b) Knn model with filtering values less than 200 mD. c) Permeability model using PERM logs. b) PERM model with filtering values less than 200 mD.

Table 1. Well data used in this study and formation tops of the Mangahewa C-shale and C-sand. The availability of core data and ANN model (Table. 5) used for petrophysical log prediction are indicated.

#	Well Name	KB (m)	TD (m)	C-Shale FT (m)	C-Sand FT (m)	Formation at TD	Phi ANN	K ANN	Core Data
1	MA-02A	45.13	5603	5115	5146	Kapuni Group	1	2	
2	MA-05A	53.3	3640	2931.3	2982	Kapuni Group	4	2	
3	MA-10A	45.13	4114	3634.5	3657.2	Kapuni Group	4	2	
4	MA-14A	53.3	3636	2985.1	3121.8	Kapuni Group	1	1	
5	Maui-1	9.45	3510	2678.58	2691	Pakawau Group	4	1	
6	Maui-2	34	3567	2709.7	2786	Basement	1	1	
7	Maui-3	34	3401	2713.5	2734.1	Pakawau Group	1	2	
8	Maui-5	26.8	3227	2740	2804	Kapuni Group	2	1	Yes
9	Maui-6	27	3228	2780	2785	Kapuni Group	1	1	Yes
10	Maui-7	27	3139	2694.9	2713.93	Kapuni Group	2	1	Yes
11	MB-03A	48.6	3656	3004	3032.7	Kapuni Group	1	2	
12	MB-05B	48.6	3431	2773.1	2807.6	Kapuni Group	1	1	
13	MB-11B	48.6	3450	2724.1	2753.6	Kapuni Group	1	1	
14	MB-N(5)	39.42	3729	2662	2718.5	Kapuni Group	1	1	
15	MB-P(8)	39.42	3709	2838.79	2857	Kapuni Group	1	1	Yes
16	MB-Q(10)	39.42	3802	3620	3673.5	Kapuni Group	4	1	
17	MB-R(1)	39.42	3620	2791	2853	Kapuni Group	3	1	Yes
18	MB-S(12)	39.42	4402	4116.5	4185.5	Kapuni Group	1	1	
19	MB-T(9)	39.42	3639	3091	3155	Kapuni Group	1	1	
20	MB-V(3)	39.42	3781	2933	2991.5	Kapuni Group	1	1	
21	MB-W(2)	39.42	4186	3330.5	3400.5	Kapuni Group	1	1	
22	MB-X(4)	39.42	4150			Kapuni Group	1	1	
23	MB-Z(11)	39.42	3100	2699	2714	Kapuni Group	1	1	
24	Rahi-1	29	3501	2874	2889	Basement	1	1	
25	Tieke-1	23.58	3579	3026.6	3026.6	Basement	1	1	

Table 2. Logs utilized in this study.

Name	Description	Unite	Min	Max	Delta	Total#
BS	Bite Size Log	in.	6.67	36	29.33	25
CALI	Caliper Log	in.	6.92	25.59	18.67	15
DENS	Compensated Formation Density Log	g/cc	0.8219	3.1236	2.3017	23
DRHO	Density Log Correction	g/cc	-0.9597	1.1005	2.0602	20
DTC	P-wave Sonic Log	us/ft	30.36	434.31	403.94	11
GR	Gamma Ray Log	GAPI	-4	353.42	357.42	25
NEUT	Thermal Neutron Porosity Log	V/V	-0.0149	18.0541	18.069	19
PEF	Photoelectric Factor	B/E	0.58	47.28	46.7	21
RESD	Deep Resistivity Log	ohmm	0.5057	31096.6	31096.09	16
SP	Spontaneous Potential Log	MV	-188.79	299.76	488.56	20
TEMP	Temperature	degC	303.78	380.82	77.04	24
RESS	Shallow Resistivity	ohmm	0.3899	1632.736	1632.346	20
TENS	Cable tension at surface Log	KGF	126.01	3795.64	3669.63	7
RESM	Medium Resistivity	ohmm	0.2308	2000	1999.769	20
DTS	S-wave Sonic Log	US/F	108.22	324.09	215.87	4
COREGD	Grain Density Core Data Measured	g/cc	2.47	3.25	0.78	5
COREK	Permeability Core Data Measured	mD	0	10000	10000	5
COREP	Porosity Core Data Measured	V/V	0.01	0.26	0.26	5

Table 3. Part of the post-logic morphological pore mean value calculations of the porosity (Phi), permeability (K) for the thin-section.

Post-Logic		
Class	Phi [%]	K [mD]
1	6.05	54.91
2	24.14	166.14
3	34.68	232.51
4	42.97	284.84
5	48.95	322.58
6	53.67	352.38
7	57.33	375.55
8	62.63	409.01
9	64.43	420.37
10	67.12	437.36
Total	21.60	47.53

Table 4. Parameters used for petrophysical log analysis for the Mangahewa C-Sand Formation. R_w is the formation water resistivity. a is the Archie's factor. n is the saturation exponent. M is the cementation factor.

Parameter	Matrix Density gm/cc	Fluid Density gm/cc	DT Matrix uSec/ft	DT Fluid uSec/ft	R_w	a	m	n
Value	2.65	1	55.5	189	0.1	1	2	2

Table 5. The ANN models and logs and wells used to predict the petrophysical logs (PHInn and Knn).

ANN Model		Logs used for NNM	Wells with same model
Type	Number		
Phi	1	GR, DENS, NEUT, PHI	Maui-7, Maui-5
	2	GR, DENS, NEUT, PHI, DTC, RESD	MB-P(8), MB-05B, MB-11B, MB-N(5), MB-X(4), MB-Z(11), MA-02A, Maui-2, Maui-3
	3	GR, RHOM, NEUT, PHI, DTC, PHIE	MB-R(1)
	4	GR, RHOM, PHI, VCL, PHIE	Maui-1, MA-05A, MA-10A
K	1	GR, VCL, SW, PHI, Perm, DTC	Maui-7, Maui-6, Maui-5, Maui-2, Maui-1, MB-Z(11) MB-P(8), MB-05B, MB-11B, MB-N(5), MB-X(4), Rahi-1
	2	GR, VCL, SW, PHI, Perm	MB-03A, MA-02A Maui-3

Table 6. QC crossplots generated for both PHI and Perm. QA crossplots for PHInn and Knn are listed.

Well	PHI QC Crossplots	Perm QC Crossplots	PHInn QA Crossplots	Knn QA Crossplots
Maui-7	GR, DENS, NEUT, DTC, PHIE, VCL, RESD, RHOMA	GR, Cali, DTC, VCL, Sw, PHI, PHIE	GR, PHI, PHIE, DENS, NUET, VCL, RESD, RHOMA	GR, DENS, Sw, PHI, PHIE
MB-P(8)	GR, DENS, NEUT, DTC, Core, PHIE, VCL, RESD, RHOMA	GR, Cali, DTC, VCL, DENS	GR, DENS, DTC, PHIE, VCL, RESD, RHOMA	GR, DENS, CAL, VCL, Sw, PHI, PHIE
Maui-1	GR, DENS, DTC, PHIE, VCL, RESD	GR, DENS, DTC, VCL, Sw, PHI, PHIE	GR, DTC, PHIE, VCL, RESD	GR, DENS, VCL, Sw, PHI, PHIE

Table 7. Statistics structural framework of the Maui Field.

Axis	Min	Max	Delta
X	1622254	1644505	22250.31
Y	5600003	5631495	31492.64
Elevation time [ms]	-4654.97	-35.75	4619.22
Lat	44°17'25.8215"S	43°58'57.2644"S	0°18'28.5570"
Long	161°50'57.7389"E	162°10'41.0423"E	0°19'43.3034"
Number of iconized horizons	16		
Number of faults	22		
Grid cells (nI x nJ x nGridLayers)	178 x 252 x 173		
Total number of grid cells	7760088		
Number of geological horizons	141		
Total number of 2D cells	44856		
Average Xinc	124.94		
Average Yinc	124.94		
Average Zinc (along pillar)	19.79466		
Rotation angle	0.02		

Table 8. Statistics for the velocity model in the Maui Field. A total of 16 horizons are interpreted.

Axis	Min	Max	Delta
X	1533000	1724000	191000
Y	5443000	5660000	217000
TWT [ms]	-5773.66	0	5773.66
Z [m]	-20178.4	0	20178.35

Table 9. Statistics for the structural grid model of the Kapuni group in the Maui B-area.

Axis	Min	Max	Delta
X	1624984	1629387	4402.61
Y	5606109	5614458	8348.96
Elevation depth [m]	-4596.31	167.83	4764.14
Lat	44°13'3.8232"S	44°08'16.3526"S	0°04'47.4706"
Long	161°53'37.2414"E	161°57'44.7793"E	0°04'7.5379"
Number of iconized horizons	16		
Number of faults	3		
Grid cells (nI x nJ x nGridLayers)	176 x 334 x 160		
Total number of grid cells	9405440		
Number of geological layers	150		
Total number of 2D cells	58784		
Average Xinc	24.99		
Average Yinc	24.99		
Average Zinc (along pillar)	26.08488		
Rotation angle	0.03		

Table 10. Statistics for a structural grid of the Mangahewa reservoir in the Maui B-area.

Axis	Min	Max	Delta
X	1624986	1629365	4379.36
Y	5606127	5614454	8327.29
Elevation depth [m]	-3152.27	-2528.68	623.59
Lat	44°13'3.1493"S	44°08'16.4768"S	0°04'46.6724"
Long	161°53'37.4159"E	161°57'43.7839"E	0°04'6.3680"
Number of iconized horizons	2		
Number of faults	3		
Grid cells (nI x nJ x nGridLayers)	175 x 333 x 31		
Total number of grid cells	1806525		
Number of geological horizons	21		
Total number of 2D cells	58275		
Average Xinc	25		
Average Yinc	25		
Average Zinc (along pillar)	11.72267		
Rotation angle	0.03		

Table 11. Statistics for all obtained petrophysical logs and models. N is the number of defined values.

Name	Type	Min	Max	Delta	N	Mean	Std	Var	Sum
PhiM	Model	0.0001	0.342	0.342	1167578	0.1757	0.07	0.005	205181.12
PhiU	Upscaled	0.0001	0.342	0.342	356	0.1625	0.07	0.0049	57.86
PHI	Calculated	0.0001	0.6	0.599	28985	0.1625	0.083	0.0069	4711.45
PHInnM	Model	0.0495	0.244	0.194	1167578	0.1973	0.034	0.0012	230379.51
PHInnU	Upscaled	0.0495	0.244	0.194	356	0.1951	0.036	0.0013	69.46
PermM	Model	0	69218.64	69218.64	1167578	788.88	5271.48	27788529.08	921087428.9
PermU	Upscaled	0	69218.64	69218.64	365	804.58	5383.99	28987406.61	293673.16
Perm	Calculated	0	96353016	96353016	29816	8083.18	575110.02	3307515E05	241008157
KnnM	Model	0.0017	10000	9999.99	1167578	386.63	1250.22	1563059.52	451426060.7
KnnU	Upscaled	0.0017	10000	9999.99	356	358.92	1257.48	1581277.76	127778.54
Knn	Predicted	0.001	10000	9999.99	28681	836.52	2288.87	5238945.62	23992391

REFERENCES

- Al-Bazzaz, W. H., and Y. W. Al-Mehanna (2007), Porosity, Permeability, and MHR calculations using SEM and thin-section images for complex Mauddud-Burgan carbonate reservoir characterization, *Society of Petroleum Engineers*, SPE 110730.
- Asquith, G., and D. Krygowski (2004), Basic well log analysis, second edition, *American Association of Petroleum Geologist and Society of Exploration Geophysics*, Methods in Exploration.
- Bahorich, M., and S. Farmer (1995), The coherence cube, *The Leading Edge*, 14(10), 1053-1058.
- Banchs, R., and R. Michelena (2002), From 3d seismic attributes to Pseudo-well-log volumes using neural networks: Practical considerations, *The Leading Edge*, 996-1001.
- Brown, A. R. (2011), Interpretation of three-dimensional seismic data, seventh edition, *AAPG Memoir 42 and SEG Investigations in Geophysics*, 9.
- Chopra, S., and K. J. Marfurt (2007), Seismic attributes for prospect identification and reservoir characterization, *SEG geophysical developments series*, 11.
- Djebbar, T., and D. Erle (2004), Petrophysics, second edition, *Elsevier Inc.*, 880.
- Dorrington, K. P., and C. A. Link (2004), Genetic-algorithm/neural-network approach to seismic attribute selection for well-log prediction, *Geophysics*, 69(1), 212–221, doi:10.1190/1.1649389.
- Gersztenkorn, A., and K. J. Marfurt (1999), Eigenstructure based coherence computations as an aid to 3-D structural and stratigraphic mapping, *Geophysics*, 64, 1468–1479.
- Hampson, D., J. Schuelke, and J. Quirein (2001), Use of multiattribute transforms to predict log properties from seismic data, *Geophysics*, 66(1), 220-236.
- Herrera, V. M., B. Russell, and A. Flores (2006), Neural networks in reservoir characterization, *The Leading Edge*, 25(4), 402–411, doi:10.1190/1.2193208.
- Higgs, K. E., M. J. Arnot, G. H. Browne, and E. M. Kennedy (2010), Reservoir potential of Late Cretaceous terrestrial to shallow marine sandstones, Taranaki Basin, New Zealand, *Marine and petroleum geology*, 27(9), 1849-1871, doi:10.1016/j.marpetgeo.2010.08.002.

- King, P. R., G. P. Thrasher, K. J. Bland, P. Carthew, D. D'Cruz, A. G. Griffin, C. M. Jones, and D. P. Strogen (2010), Cretaceous-Cenozoic geology and petroleum systems of the Taranaki Basin, New Zealand. Digitally remastered version. GNS Science, Lower Hutt, *Institute of Geological & Nuclear Sciences monograph*, 13.
- Marfurt, K., R. Kirlin, S. Farmer, and M. Bahorich (1998), 3-D seismic attributes using a semblance-based coherency algorithm, *Geophysics*, 63, 1150-1165.
- Marfurt, K. J., V. Sudhaker, A. Gersztenkorn, K. D. Crawford, and S. E. Nissen (1999), Coherency calculations in the presence of structural dip, *Geophysics*, 64(1), 104–111, doi:10.1190/1.1444508.
- New Zealand Petroleum and Minerals (NZPAM) (2014), New Zealand Petroleum Basins, *Ministry of Business, Innovation and Employment, Wellington, New Zealand*, ISSN 2324-3988.
- New Zealand Petroleum and Minerals (2015), 2015 Petroleum Exploration Data Pack, External HDD, *Ministry of Business, Innovation & Employment, Wellington, New Zealand*.
- Stern, T. A., and F. J. Davey (1990), Deep seismic expression of a foreland basin: Taranaki basin, New Zealand, *Geology*, 18, 979-982.

PAPER

III. VALIDATION OF POSTSTACK SEISMIC INVERSION USING ROCK PHYSICS ANALYSIS AND 3D SEISMIC AND WELL CORRELATION

Aamer Alhakeem*, Kelly Liu, Tianze Zhang, and Stephen Gao

Missouri University of Science and Technology

ABSTRACT

Inversion of poststack seismic data is validated with rock physics analysis from the well data. The acoustic impedance is computed throughout the well-seismic-tie and synthetic seismogram generation. Seismic attributes, including velocities and results of inversion, are generated to study the potential prospect in the Maui Field, Taranaki Basin, New Zealand. Seismic interpretation generated structure and amplitude horizon slices as well as the recursive algorithmic attribute are applied to invert the seismic traces to provide quantitative predictions on the reservoir properties. Stratigraphic evaluation is obtained from the interpretation. After evaluating the petrophysical parameters from well logs, the poststack inversion of the seismic data is validated. The results are reliable for future use in an artificial neural network.

1. INTRODUCTION

Inversion is an essential process for seismic exploration to convert the seismic contrast model into a layer cake model. Nowadays, there is a growth in attribute analysis being applied to seismic volume for generating different properties. Poststack seismic inversion can be obtained, not only from deterministic physical calculations such as

recursive inversion (Yilmaz, 2001; Russell and Hampson, 2006), but also from probabilistic artificial intelligence, with reliable results. Therefore, quality control and validation of the input parameters should be implemented for a specific dataset.

Seismic exploration is a tool that physically describes the property of the Earth's subsurface, and rock physics analysis can validate the quality of the seismic attributes. Rock physics templates (RPT) are developed to investigate the correlations between the petrophysical parameters of rock and its physical properties (Ødegaard and Avseth, 2003; Avseth et al., 2005; Bachrach and Avseth, 2008; Chi and Han, 2009; Russell, 2013), among which the porosity and fluid saturation are related to the acoustic impedance and V_p/V_s of the P- and S-wave velocities (Figure 1).

This study targets a high potential prospective sand reservoir in the coastal marine environment. The main objective of this study is to examine the relationship between rock physics and petrophysics properties from different perspectives, including seismic and well logs, to evaluate the integrated results of acoustic impedance and porosity. In addition, it can assess neural network inversion modeling by providing a quality management for the input parameters to the model

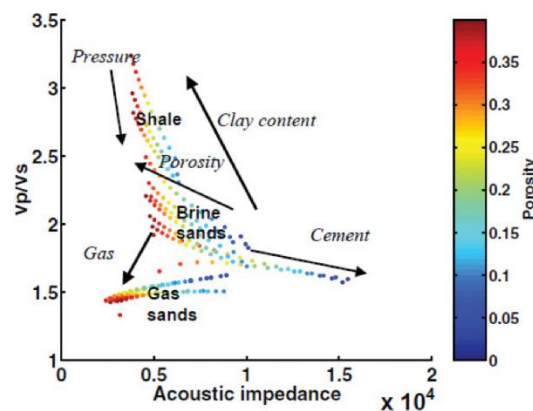


Figure 1. Rock physics template (RPT) developed by Ødegaard and Avseth (2003).

2. RECURSIVE INVERSION

Seismic poststack inversion of the amplitude seismic traces can be conducted in different ways to determine the acoustic impedance values (Z). The recursive inversion is considered to be a reliable inversion method (Russell and Hampson, 2006). The recursive equation applied to each trace of effects of the wavelet within the seismic bandwidth is described as

$$Z_{P_{i+1}} = Z_{P_i} \left[\frac{1 + r_{P_i}}{1 - r_{P_i}} \right], \quad (1)$$

where r_{P_i} is the zero-offset P-wave reflection coefficient at the i th interface of a stack of N layers, and $Z_{P_i} = \rho_i V_{P_i}$ is the i th P-impedance of the i th layer, where ρ is the density, V_p is the P-wave velocity (Russell and Hampson, 2006).

The inversion method is applied to the seismic data to generate the inversion volume in the time domain. Attributes such as velocity, amplitude, structure, and results from the inversion are used for seismic interpretation.

3. SEISMIC INTERPRETATION

3D seismic interpretation is correlated with the geological background to target the C-sand Formation of Kapuni group in the Maui Field, Taranaki Basin, New Zealand (Higgs et al., 2009; Alhakeem, 2017). A synthetic seismogram is computed from the well data. This process inverts the elastic property logs to the seismic trace by calculating the r_{P_i} . A time to depth chart (T-D) is applied to match the well-logs with the seismic data. The wavelet is extracted from the seismic data in the area near the well. Logs used from the Maui well include sonic logs, density logs, and gamma ray, which are used to

determine the acoustic impedance and reflection coefficient (Figure 2). AI is extracted along the borehole by a process that is performed by interpolating the seismic trace around the deviated borehole by fixed sample interval. Similarly, velocity trace and seismic trace are obtained.

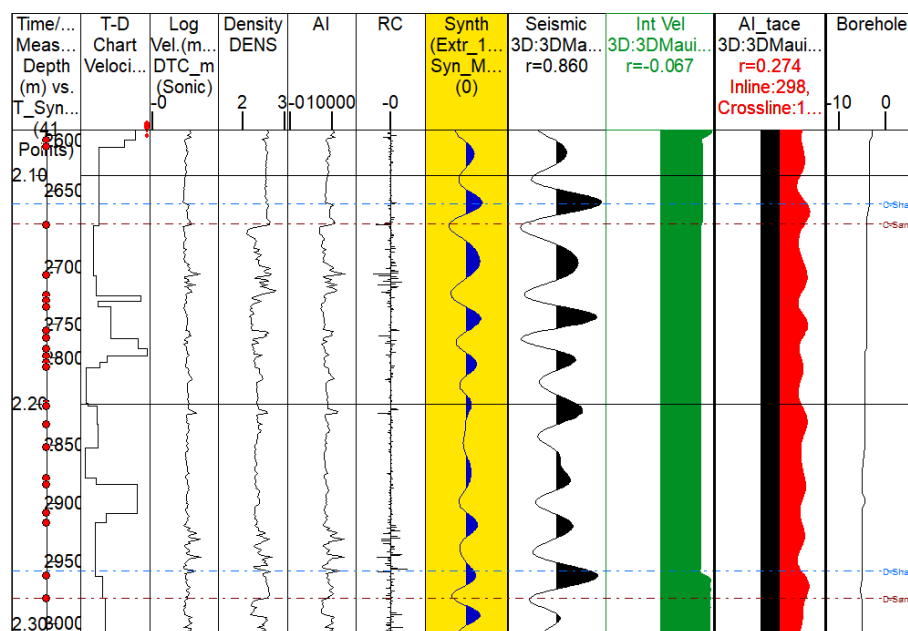


Figure 2. Synthetic seismogram generation for Well MB-Z(11). The cross-correlation coefficient between the seismic trace and the synthetic seismogram (r) value is 0.86 indicating a good match. The acoustic impedance log (AI) is generated from density logs (DENS) and sonic logs (DT). The synthetic seismogram is generated from the reflection coefficient (RC) and the computed zero phase wavelet. Gamma ray (GR) is used as the reference log. The right three traces are extracted along the borehole from amplitude, velocity, and inversion.

After matching the synthetic seismogram with the seismic data for about ten wells in the field, the inversion attribute volume is utilized in the horizon tracking to generate a C-sand structure map (Figure 3). More horizons are interpreted and utilized for updating the T-D chart for volume time to depth conversion. The inversion attribute is generated and presented with amplitude horizon slices (Figure 4). The two maps are cross plotted

(Figure 5). The calculated AI is overlaid within a vertical section that crosses the wells (Figure 6).

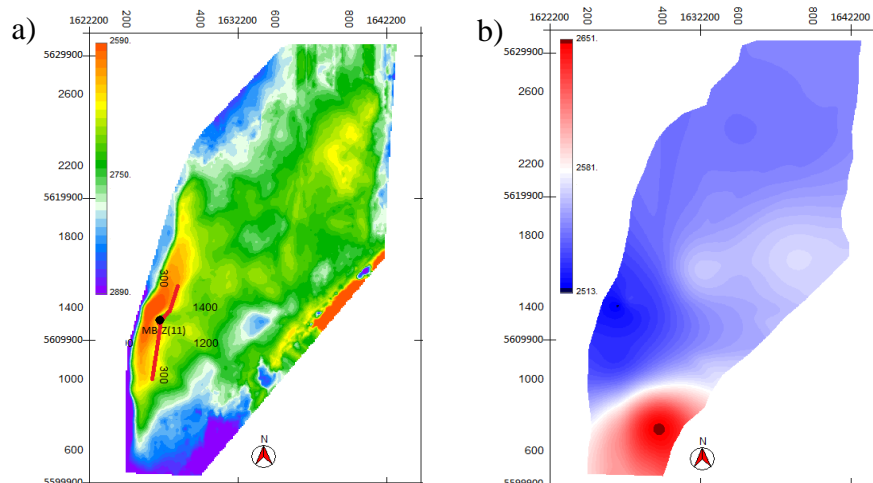


Figure 3. C-sand horizon interpretation. (a) Depth structure map shows an anticline to the southwest. The red arbitrary line crosses Well MB-Z(11). (b) Average velocity map shows lower values to the south. Velocity attributes are used to generate interval velocity volume for time to depth conversion.

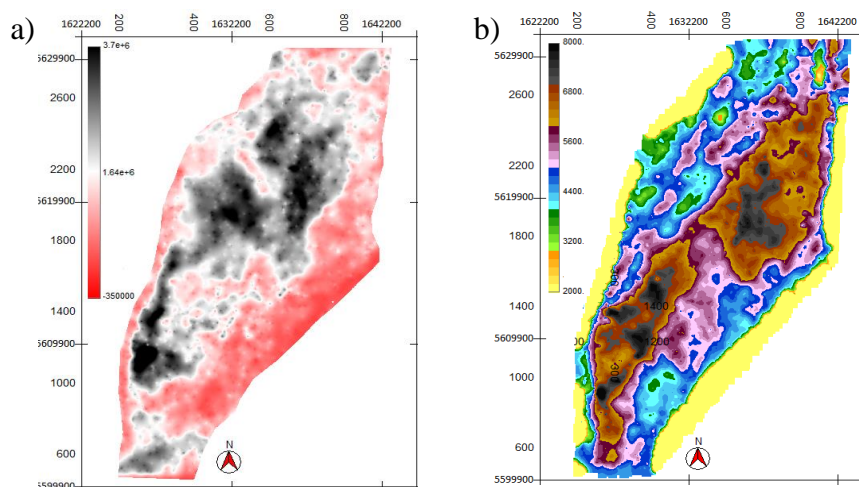


Figure 4. Seismic attributes of C-sand. (a) Amplitude horizon slice shows potential sand prospects deposited in the coastal plain environment. (b) Recursive inversion horizon slice map reveals two prospective areas within the Maui Field.

4. ROCK PHYSICS ANALYSIS

V_p/V_s and Poisson's ratio (ν) are used to validate the quality of the seismic inversion output for both the elastic logs and the elastic seismic attributes because of the relationship that relates these parameters with the porosity and fluid saturation (Figure 7). AI relations with both P-wave sonic (DTC) and the S-wave sonic (DTS) are plotted for contrast and evaluation (Figure 8). Rock property templates are developed for such quality control process. Rock physics template in Figure 1 is implemented for rock physical property analysis. The results show an excellent match for porosity estimation and the type and quantity of fluid saturation (Figure 9).

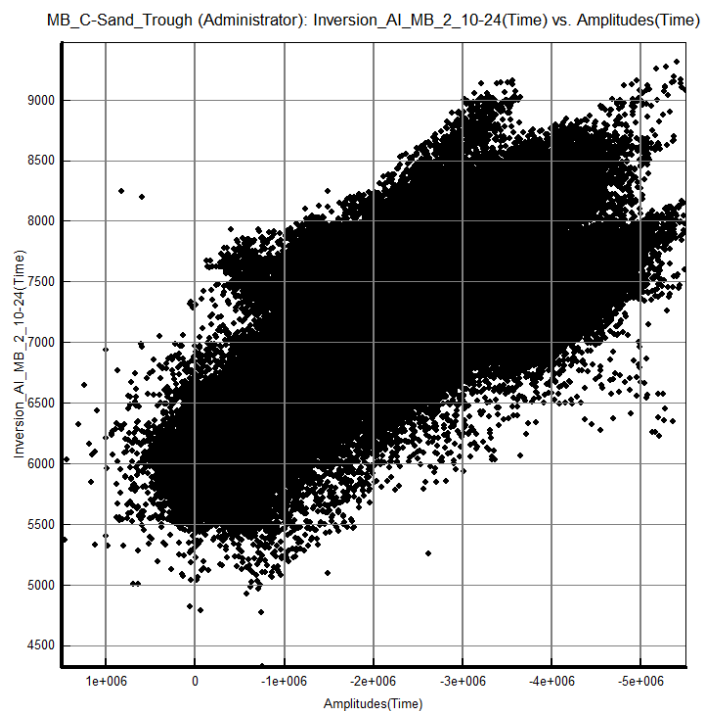


Figure 5. Crossplot between the C-sand amplitude horizon slice in Figure 4a and the C-sand AI slice in Figure 4b.

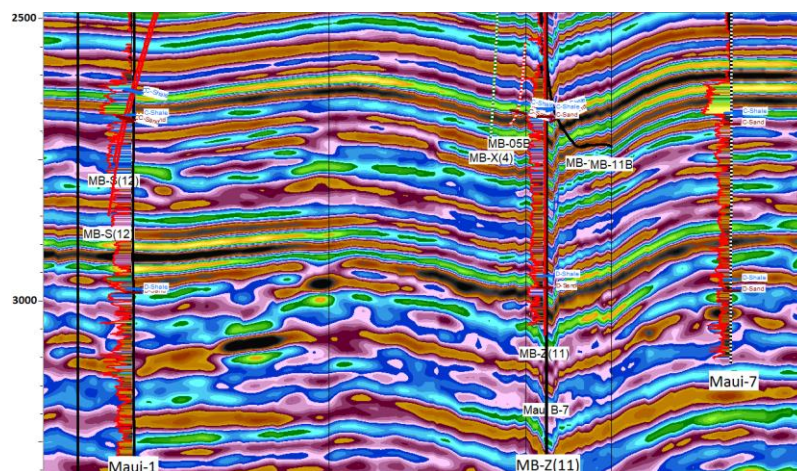


Figure 6. Inversion attribute cross-section along the arbitrary line shown in Figure 3a. The computed AI logs are overlaid with the vertical section across MB-Z(11), Maui-1, and Maui-7 wells.

5. DISCUSSION

The rock physics analysis (Figure 10) shows a good indication of gas saturated in a high porous sand reservoir. The AI, V_p/V_s , and DENS also show a proper match to the parameters obtained from the well logs and the seismic attributes.

In addition, the AI extracted from the seismic inversion is cross plotted with the V_p/V_s color-coded with both PHI and ν . As indicated in Figure 11, the Poisson's ratio is distributed perfectly indicating higher values for the shale identified successfully by the rock physics analysis. As a result, the generated seismic inversion volume is validated by applying the rock physics analysis to both logs and traces.

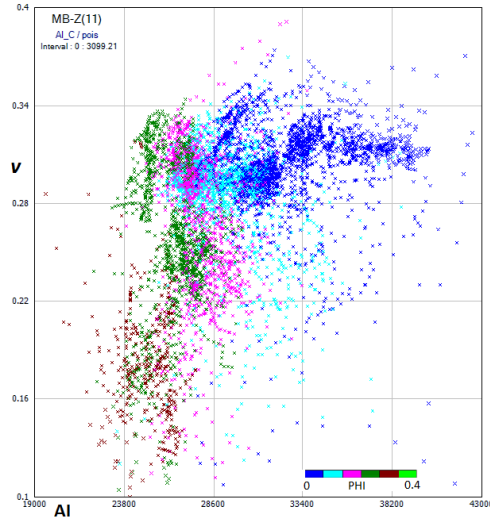


Figure 7. AI results from rock physics analysis vs. Poisson's ratio (ν) color-coded with PHI. Higher AI and ν values corresponds with lower porosity.

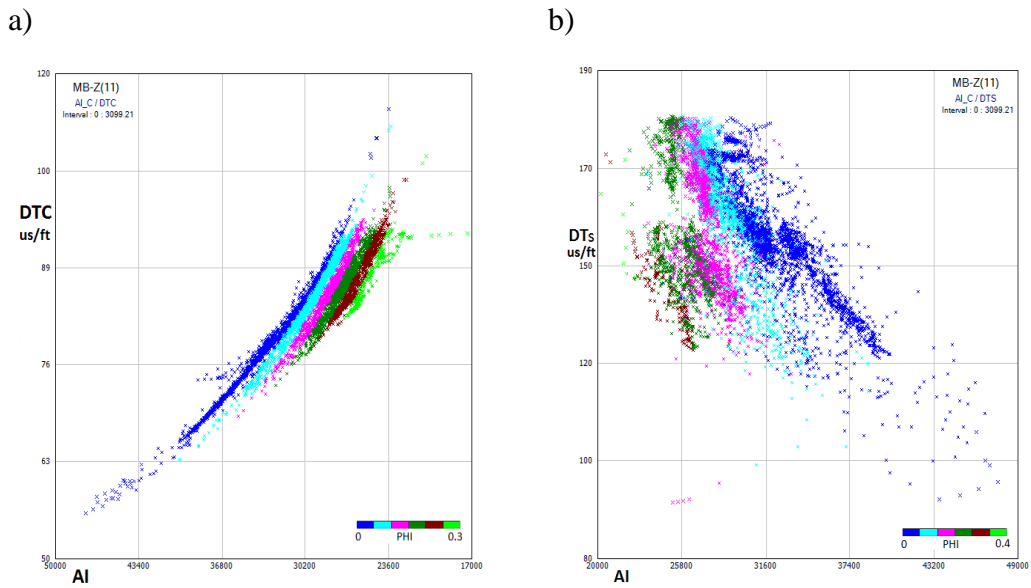


Figure 8. AI computed vs. sonic logs color-coded with PHI showing a good regression relation for Well MB-Z(11). (a) AI vs. DTC. (b) AI vs. DTS.

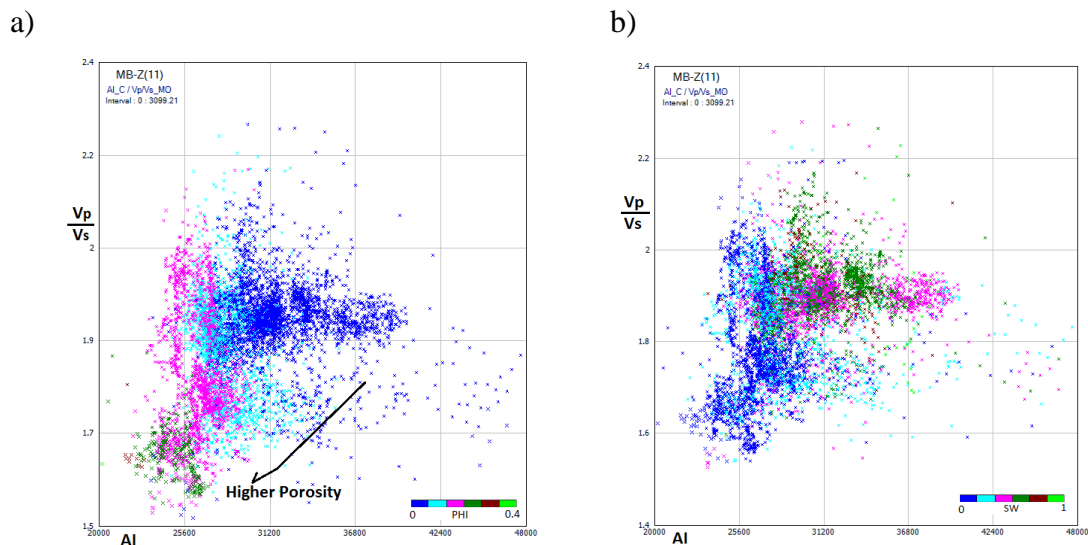


Figure 9. Rock physics template showing AI vs. V_p/V_s . (a) PHI color-coded crossplot shows a proper match to the RPT. (b) Water saturation log (SW) color-coded crossplot shows the effect of fluid saturation to the distribution of the porosity around the crossplots by comparison with (a).

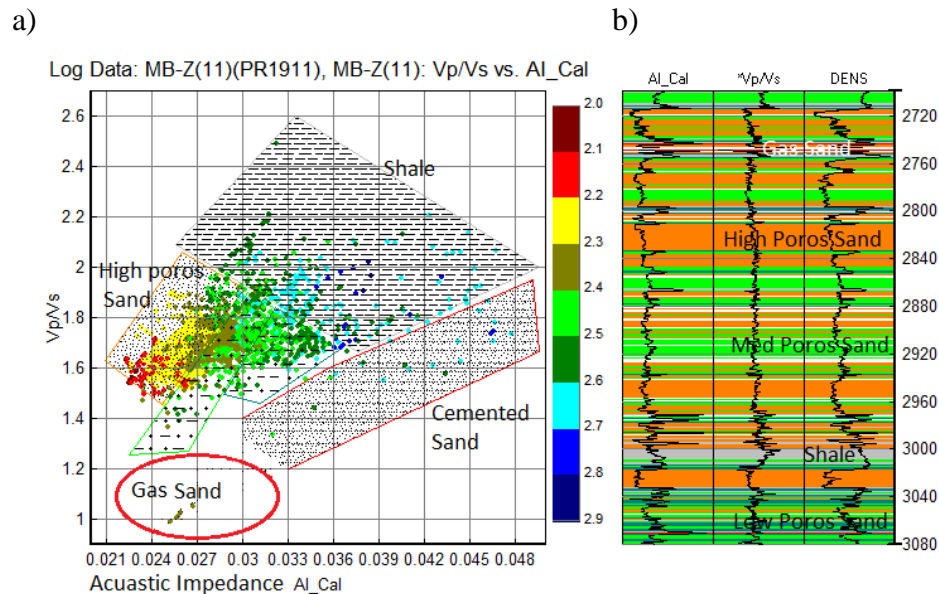


Figure 10. Rock physics template for facies analysis. (a) AI vs. V_p/V_s crossplot color-coded with DENS showing the analysis of facies identification from the RPT to evaluate the computed AI logs. (b) Logs facies and porosity indication using RPT.

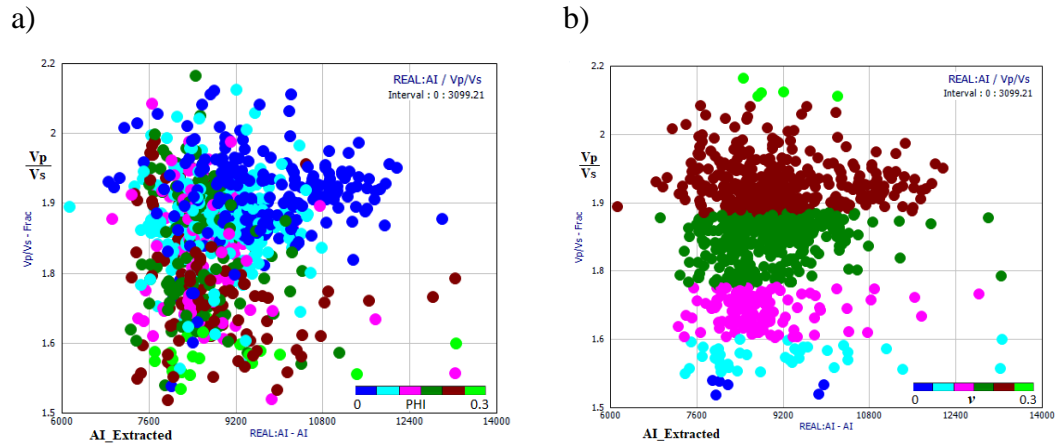


Figure 11. AI extracted vs. V_p/V_s crossplot for Well MB-Z(11). (a) Color-coded with PHI. (b) Color-coded with v .

6. CONCLUSIONS

Sonic log, density log, and interpreted seismic horizons are utilized for the poststack inversion. The resulting amplitude and inversion horizon slice maps are cross plotted showing a good relation.

The results of rock property analysis of crossplot of AI vs. V_p/V_s match well with the PHI values. Finally, the AI extracted from the seismic inversion around the well borehole was cross plotted with the V_p/V_s and color-coded with PHI and v , both showing a proper fit to the rock physics template. These processes are applied to a high potential prospective sand reservoir in the coastal marine environment. Along with the inversion attributes, this work improves matching between well log observations and rock-physics models.

For future research, other attributes such as reflectivity and density could be generated and validated to be integrated for an artificial neural network inversion.

REFERENCES

- Alhakeem, A., H. Almubarak, K. Liu, and W. Al-Bazzaz (2017), 3D seismic attribute analysis for structure and stratigraphy identification in Maui field, Taranaki Basin, New Zealand, Poster presentation, *2017 New Zealand Petroleum Conference*.
- Avseth, P., T. Mukerji, and G. Mavko (2005), Quantitative seismic interpretation, *Cambridge University Press*.
- Bachrach, R., and P. Avseth (2008), Rock physics modeling of unconsolidated sands: Accounting for nonuniform contacts and heterogeneous stress fields in the effective media approximation with applications to hydrocarbon exploration, *Geophysics*, 73, no. 6, E197–E209, doi: 10.1190/1.2985821.
- Chi, X., and D. Han (2009), Lithology and fluid differentiation using a rock physics template, *The Leading Edge*, 28(1), 60–65.
- Higgs, K. (2009). Opportunities for underground geological storage of CO₂ in New Zealand - Report CCS-08/6 - Onshore Taranaki Paleogene reservoirs, *GNS Science Report 2009/59*. 108 p.
- Russell, B., and D. Hampson (2006), The old and the new in seismic inversion: *Recorder*, 31(10).
- Russell, B. (2013), A Gassmann-consistent rock physics template, *Recorder*, 38(6), 22–30.
- Yilmaz, O. (2001), Seismic Data Analysis, *Soc. of Explor. Geophys., Tulsa, Okla*, 2027 p.
- Ødegaard, E., and P. Avseth (2003), Interpretation of elastic inversion results using rock physics templates, *EAGE, Expanded Abstracts*.
- Ødegaard, E., and P. Avseth (2004), Well log and seismic data analysis using rock physics templates, *First Break*, 23, 37–43.

SECTION

2. CONCLUSIONS

This study provides a geological visualization of the subsurface in the Taranaki Basin by integrating the regional geological, 3D seismic, well logs, core, well test, and well production history data. Time structure, horizon slice, velocity, depth structure, and isopach are constructed. The seismic volume are converted from time to depth domain for better correlation with well logs.

Stratigraphy from the 3-D seismic data are conducted to identify different geological features. The seismic data are interpreted and compared to well logs to identify facies sequences within the stratigraphy. Also, the study built a methodology to recognize reservoirs such as fluvial dominated channels, point bars, terrestrial, paralic and nearshore sandstone, turbidites, and fractured limestone, volcanoclastics, and shelf sands reservoirs.

Petrophysical analysis is implemented using geological data in the form of the thin sections of well cores to conduct the reservoir properties and to calculate petrophysical parameters including the water saturation, shale volume, and porosity. The thin sections are scanned and analyzed using the visual analysis software tool that counts different pores and grains beside measuring their shapes and sizes which are crucial for porosity and permeability. These values are compared with the seismic attribute results in porosity generated by Pseudo attributes. This process leads to optimal methodology of reservoir characterization. Analyzing of prospect and reservoir characterization of the Maui B-area results petrophysical measurements of different parameters. The porosity is estimated for the Mangahewa and Kaimiro formations.

Attribute analyses are the main goal achieved in this study. Geometric attributes such as volumetric dip and azimuth, coherence and curvature are cross plotted to strengthen the summation of their outputs supporting the seismic interpretation. Attribute measurements are utilized to characterize the subsurface structure and depositional system. Finally, multi-attribute analyses assist clustering the attributes as a useful tool that optimized the results predicted from attributes. The neural network modeling based on the consistent area identified to generated pseudo porosity logs used to build a property volume model by distributing the predicted logs along a structure grid model providing optimal reservoir characterization

This integrated study supports the petroleum exploration with the low cost by using the capabilities of the geophysical processing and interpretation of the seismic data. The seismic attribute and reservoir models that identify the potential prospects and characterize the targeted formation provide constraints for future exploration and drilling.

APPENDIX

QC and QA Crossplots Generated

	Regression	R	Fig	Well	Relation
QC PHI					
DENS	Linear	0.96	a	MB-P(8)	PHI=1.52 - 0.59 DENS
NEUT	Linear	0.75	b	Maui-7	PHI = -0.097007327 + 0.760534697 * NEUT
VCL	Linear	0.82	c	Maui-1	PHI=0.463874-0.83556*VCL
VCL	Linear	0.02		MB-P(8)	PHI = 0.1226948 - 0.011323448 * VCLN
PHIE	Linear	0.96	d	Maui-1	PHI=-0.0564448 + 1.08727*PHIE
PHIE	Linear	0.86		MB-P(8)	PHI = -0.065619819 + 1.212188852 * PHIE
PHIE	Linear	0.84		Maui-7	PHIE = 0.006200226 + 1.235314732 * PHI
RHOM	Linear	0.88	e	Maui-7	RhoMatApp = 3.005656459 - 2.321141689 * PHI
RESD	Polynomial	0.80	f	Maui-7	PHI = 0.16 + 0.033 * Log(RESD) - 0.67 * Log(RESD)^2 + 0.897 * Log(RESD)^3 - 0.4 * Log(RESD)^4 + 0.059 * Log(RESD)^5
DTC	Linear	0.56	g	Maui-1	DTC = 69.245296802 + 40.943344844 * PHI
QC Perm					
PHI	Exponential	0.99	h	MB-P(8)	PHI = 0.0862843569 * e ^ (0.497815174 * Log(Perm))
PHI	Exponential	0.97		Maui-7	PHI = 0.107283096 * e ^ (0.456437341 * Log(Perm))
DENS	Linear	0.81	i	Maui-7	Log(Perm) = 27.081730608 - 11.487154591 * DENS
DENS	Polynomial	0.87		MB-P(8)	Log(Perm) = 87.892 - 63.048 * DENS - 45.697 * DENS^2 + 49.447 * DENS^3 - 10.757 * DENS^4
DENS	Linear	0.85		Maui-1	Log(Perm) = 22.863182746 - 9.72322262 * DENS
SW	Exponential	0.50	j	Maui-1	SW = 0.294170795 * e ^ (-0.351590163 * Log(Perm))
PHIE	Linear	0.92	k	Maui-1	PHIE = 0.118669989 + 0.065767256 * Log(Perm)
PHIE	Linear	0.87		Maui-7	PHIE = 0.170359212 + 0.054482857 * Log(Perm)
PHIE	Exponential	0.93		Maui-1	PHIE = 0.144880261 * e ^ (0.246471722 * Log(Perm))
VCL	Linear	0.70	l	Maui-1	VCLAV = 0.374292765 - 0.039608106 * Log(Perm)
RHOMA	Polynomial	0.88		Maui-7	RhoMatApp = 2.7277 - 0.096082 * Log(Perm) - 0.0025579 * Log(Perm)^2 + 0.001454 * Log(Perm)^3 + 9.1067e-05 * Log(Perm)^4
QA PHInn					
DENS	Linear		a	Maui-7	
DTC	Linear		b	Maui-1	
GR	Linear	0.96	c	Maui-1	COREP_nn_3 = 0.30697 - 0.0013 * GR
Perm	Linear	0.89	d	MB-P(8)	Log(Perm) = -16.85918 + 84.79684 * COREP_nn
NEUT	Linear		e	Maui-7	
PHI	Linear	0.64	f	Maui-7	CorePhi_nn = 0.127646 + 0.51203 * PHI
RHOM	Linear	0.57	g	MB-P(8)	RhoMatApp = 3.74327 - 5.33973 * COREP_nn
PHIE	Linear	0.88	h	Maui-7	PHIE = -0.24731 + 2.05419 * CorePhi_nn
RESD	Polynomial	0.73	i	Maui-1	COREP_nn_3 = 0.30877 - 0.228650417 * Log(RESD) + 0.082031 * Log(RESD)^2 + 0.038428 * Log(RESD)^3 - 0.015708 * Log(RESD)^4
VCL	Linear		j	MB-P(8)	
QA Knn					
GR	Exponential	0.83	k	Maui-1	Log(COREK_nn2) = 7.175 * e ^ (-0.0182817747 * GR)
DENS	Exponential	0.89	l	Maui-1	Log(COREK_nn2) = 1443.55674 * e ^ (-3.07427643 * DENS)
DENS	Exponential	0.79		Maui-7	Log(CORE_nn_9_10_2) = 541.50694 * e ^ (-2.28526075 * DENS)
PHI	Exponential	0.94	m	Maui-1	Log(COREK_nn2) = 0.715289923 * e ^ (4.57402308 * PHI)
PHIE	Exponential	0.96	n	Maui-1	Log(COREK_nn2) = 0.533069267 * e ^ (5.27400412 * PHIE)
VCL	Exponential	0.85	o	Maui-1	Log(COREK_nn2) = 7.20215548 * e ^ (-4.39344641 * VCLAV)
VCL	Linear	0.82		MB-P(8)	Log(COREK_nn) = 3.381239086 - 10.027658574 * VCLGR
SW	Polynomial	0.94	p	Maui-1	SW = 0.43276 - 0.066725 * Log(Knn) - 0.41020 * Log(Knn)^2 + 0.27257 * Log(Knn)^3 - 0.042982 * Log(Knn)^4
PHInn	Exponential	0.85	Fig.1b	Maui-1	Log(COREK_nn2) = 0.128460536 * e ^ (13.1671771 * COREP_nn_3)

BIBLIOGRAPHY

- Al-Bazzaz, W. H., and Y. W. Al-Mehanna (2007), Porosity, Permeability, and MHR calculations using SEM and thin-section images for complex Mauddud-Burgan carbonate reservoir characterization, *Society of Petroleum Engineers*, SPE 110730.
- Al-Bazzaz, W. H. (2017), Classification of pore wettability, Email.
- Alhakeem, A. A., H. Almubarak, K. Liu, and W. H. Al-Bazzaz (2017), 3D seismic attribute analysis for structure and stratigraphy identification in Maui field, Taranaki Basin, New Zealand, Poster presentation, *2017 New Zealand Petroleum Conference*.
- Asquith, G., and D. Krygowski (2004), Basic well log analysis, second edition, *American Association of Petroleum Geologist and Society of Exploration Geophysics*, Methods in Exploration.
- Avseth, P., T. Mukerji, and G. Mavko (2005), Quantitative seismic interpretation, *Cambridge University Press*.
- Bachrach, R., and P. Avseth (2008), Rock physics modeling of unconsolidated sands: Accounting for nonuniform contacts and heterogeneous stress fields in the effective media approximation with applications to hydrocarbon exploration, *Geophysics*, 73, no. 6, E197–E209, doi: 10.1190/1.2985821.
- Bahorich, M., and S. Farmer (1995), The coherence cube, *The Leading Edge*, 14(10), 1053-1058.
- Banchs, R. E., and R. J. Michelena (2002), From 3d seismic attributes to Pseudo-well-log volumes using neural networks: Practical considerations, *The Leading Edge*, 996-1001.
- Brown, A. R. (2011), Interpretation of three-dimensional seismic data, seventh edition, *AAPG Memoir 42 and SEG Investigations in Geophysics*, 9.
- Chi, X., and D. Han (2009), Lithology and fluid differentiation using a rock physics template, *The Leading Edge*, 28(1), 60-65.
- Chopra, S., and K. J. Marfurt (2007), Seismic attributes for prospect identification and reservoir characterization, *SEG geophysical developments series*, 11.

- Djebbar, T., and D. Erle (2004), *Petrophysics*, second edition, *Elsevier Inc.*, 880.
- Dorrington, K. P., and C. A. Link (2004), Genetic-algorithm/neural-network approach to seismic attribute selection for well-log prediction, *Geophysics*, 69(1), 212–221, doi:10.1190/1.1649389.
- Gersztenkorn, A., and K. J. Marfurt (1999), Eigenstructure based coherence computations as an aid to 3-D structural and stratigraphic mapping, *Geophysics*, 64, 1468–1479.
- Hampson, D., J. Schuelke, and J. Quirein (2001), Use of multiattribute transforms to predict log properties from seismic data, *Geophysics*, 66(1), 220-236.
- Herrera, V. M., B. Russell, and A. Flores (2006), Neural networks in reservoir characterization, *The Leading Edge*, 25(4), 402–411, doi:10.1190/1.2193208.
- Higgs, K. (2009), Opportunities for underground geological storage of CO₂ in New Zealand - Report CCS-08/6 - Onshore Taranaki Paleogene reservoirs, *GNS Science Report 2009/59*. 108 p. doi:10.1016/j.marpetgeo.2010.08.002.
- Higgs, K. E., M. J. Arnot, G. H. Browne, and E. M. Kennedy (2010), Reservoir potential of Late Cretaceous terrestrial to shallow marine sandstones, Taranaki Basin, New Zealand, *Marine and petroleum geology*, 27(9), 1849-1871.
- King, P. R., G. P. Thrasher, K. J. Bland, P. Carthew, D. D’Cruz, A. G. Griffin, C. M. Jones, and D. P. Strogen (2010), Cretaceous-Cenozoic geology and petroleum systems of the Taranaki Basin, New Zealand. Digitally remastered version. GNS Science, Lower Hutt, *Institute of Geological & Nuclear Sciences monograph*, 13.
- Marfurt, K. J., R. L. Kirlin, S. L. Farmer, and M. S. Bahorich (1998), 3-D seismic attributes using a semblance-based coherency algorithm, *Geophysics*, 63, 1150-1165.
- Marfurt, K. J., V. Sudhaker, A. Gersztenkorn, K. D. Crawford, and S. E. Nissen (1999), Coherency calculations in the presence of structural dip, *Geophysics*, 64(1), 104–111, doi:10.1190/1.1444508.
- New Zealand Petroleum and Minerals (NZPAM) (2014), *New Zealand Petroleum Basins, Ministry of Business, Innovation and Employment, Wellington, New Zealand*, ISSN 2324-3988.
- New Zealand Petroleum and Minerals (2015), *2015 Petroleum Exploration Data Pack, External HDD, Ministry of Business, Innovation & Employment, Wellington, New Zealand*.

- Russell, B., and D. Hampson (2006), The old and the new in seismic inversion, *Recorder*, 31(10).
- Russell, B. (2013), A Gassmann-consistent rock physics template, *Recorder*, 38(6), 22–30.
- Stern, T. A., and F. J. Davey (1990), Deep seismic expression of a foreland basin: Taranaki basin, New Zealand, *Geology*, 18, 979-982.
- Yilmaz, O. (2001), *Seismic Data Analysis*, Soc. of Explor. Geophys., Tulsa, Okla, 2027 p.
- Ødegaard, E., and Avseth, P. (2003), Interpretation of elastic inversion results using rock physics templates, *EAGE, Expanded Abstracts*.
- Ødegaard, E., and P. Avseth (2004), Well log and seismic data analysis using rock physics templates, *First Break*, 23, 37–43.

VITA

Aamer AlHakeem was born in Dhahran, Saudi Arabia. In 2007, he received his B.S. in Geophysics from King Fahd University of Petroleum and Minerals, Dhahran, Saudi Arabia. He did his summer training at Saudi ARAMCO during the summer of 2006. After working for two years in EniRepSa Gas Ltd., Khobar, Saudi Arabia, he joined Missouri University of Science and Technology to continue his academic career. In 2013, he received his Master degree in Geology and Geophysics. And in 2018, he received his PhD in Geology and Geophysics.

He has published conference and journal papers, some of which are listed with the references of this research. Aamer AlHakeem has been a member of Society of Exploration Geophysicist since 2004. He has been a member of the American Association of Petroleum Geologists (AAPG) since 2006. He was praised by his colleagues at Missouri S&T and elected president of the SEG student chapter. In 2017 he gave the rise to the 2017 SEG Excellence Student Chapter Ridge Award for Missouri S&T. He has been awarded by the geology and geophysics department with the 2017 Outstanding Service Award. Moreover, Aamer received the 2017 SEG/ Chevron Student Leadership Award.